Numerical Modelling for Elastic Waves in Laminated Composite Plates

by

Jiujing Zhu

A thesis
presented to the University of Manitoba
in fulfilment of the
thesis requirement for the degree of
Doctor of Philosophy
in
Civil Engineering

Winnipeg, Manitoba, Canada 1996

©Jiujing Zhu 1996

National Library of Canada
Acquisitions and Bibliographic Services Branch
395 Wellington Street
Ottawa, Ontario
K1A 0N4

Bibliothèque nationale du Canada
Direction des acquisitions et des services bibliographiques
395, rue Wellington
Ottawa (Ontario)
K1A 0N4

Your file *Votre référence*

Our file *Notre référence*

The author has granted an irrevocable non-exclusive licence allowing the National Library of Canada to reproduce, loan, distribute or sell copies of his/her thesis by any means and in any form or format, making this thesis available to interested persons.

L'auteur a accordé une licence irrévocable et non exclusive permettant à la Bibliothèque nationale du Canada de reproduire, prêter, distribuer ou vendre des copies de sa thèse de quelque manière et sous quelque forme que ce soit pour mettre des exemplaires de cette thèse à la disposition des personnes intéressées.

The author retains ownership of the copyright in his/her thesis. Neither the thesis nor substantial extracts from it may be printed or otherwise reproduced without his/her permission.

L'auteur conserve la propriété du droit d'auteur qui protège sa thèse. Ni la thèse ni des extraits substantiels de celle-ci ne doivent être imprimés ou autrement reproduits sans son autorisation.

ISBN 0-612-16395-4

Canada

Name _____

Dissertation Abstracts International and *Masters Abstracts International* are arranged by broad, general subject categories. Please select the one subject which most nearly describes the content of your dissertation or thesis. Enter the corresponding four-digit code in the spaces provided.

Engineering, Civil

SUBJECT TERM

0543 UMI

SUBJECT CODE

Subject Categories

THE HUMANITIES AND SOCIAL SCIENCES

COMMUNICATIONS AND THE ARTS

Architecture 0729
Art History 0377
Cinema 0900
Dance 0378
Fine Arts 0357
Information Science 0723
Journalism 0391
Library Science 0399
Mass Communications 0708
Music 0413
Speech Communication 0459
Theater 0465

EDUCATION

General 0515
Administration 0514
Adult and Continuing 0516
Agricultural 0517
Art 0273
Bilingual and Multicultural 0282
Business 0688
Community College 0275
Curriculum and Instruction 0727
Early Childhood 0518
Elementary 0524
Finance 0277
Guidance and Counseling 0519
Health 0680
Higher 0745
History of 0520
Home Economics 0278
Industrial 0521
Language and Literature 0279
Mathematics 0280
Music 0522
Philosophy of 0998
Physical 0523
Psychology 0525
Reading 0535
Religious 0527
Sciences 0714
Secondary 0533
Social Sciences 0534
Sociology of 0340
Special 0529
Teacher Training 0530
Technology 0710
Tests and Measurements 0288
Vocational 0747

LANGUAGE, LITERATURE AND LINGUISTICS

Language
- General 0679
- Ancient 0289
- Linguistics 0290
- Modern 0291

Literature
- General 0401
- Classical 0294
- Comparative 0295
- Medieval 0297
- Modern 0298
- African 0316
- American 0591
- Asian 0305
- Canadian (English) 0352
- Canadian (French) 0355
- English 0593
- Germanic 0311
- Latin American 0312
- Middle Eastern 0315
- Romance 0313
- Slavic and East European 0314

PHILOSOPHY, RELIGION AND THEOLOGY

Philosophy 0422
Religion
- General 0318
- Biblical Studies 0321
- Clergy 0319
- History of 0320
- Philosophy of 0322

Theology 0469

SOCIAL SCIENCES

American Studies 0323
Anthropology
- Archaeology 0324
- Cultural 0326
- Physical 0327

Business Administration
- General 0310
- Accounting 0272
- Banking 0770
- Management 0454
- Marketing 0338

Canadian Studies 0385
Economics
- General 0501
- Agricultural 0503
- Commerce-Business 0505
- Finance 0508
- History 0509
- Labor 0510
- Theory 0511

Folklore 0358
Geography 0366
Gerontology 0351
History
- General 0578
- Ancient 0579
- Medieval 0581
- Modern 0582
- Black 0328
- African 0331
- Asia, Australia and Oceania 0332
- Canadian 0334
- European 0335
- Latin American 0336
- Middle Eastern 0333
- United States 0337

History of Science 0585
Law 0398
Political Science
- General 0615
- International Law and Relations 0616
- Public Administration 0617

Recreation 0814
Social Work 0452
Sociology
- General 0626
- Criminology and Penology ... 0627
- Demography 0938
- Ethnic and Racial Studies 0631
- Individual and Family Studies 0628
- Industrial and Labor Relations 0629
- Public and Social Welfare 0630
- Social Structure and Development 0700
- Theory and Methods 0344

Transportation 0709
Urban and Regional Planning 0999
Women's Studies 0453

THE SCIENCES AND ENGINEERING

BIOLOGICAL SCIENCES

Agriculture
- General 0473
- Agronomy 0285
- Animal Culture and Nutrition 0475
- Animal Pathology 0476
- Food Science and Technology 0359
- Forestry and Wildlife 0478
- Plant Culture 0479
- Plant Pathology 0480
- Plant Physiology 0817
- Range Management 0777
- Wood Technology 0746

Biology
- General 0306
- Anatomy 0287
- Biostatistics 0308
- Botany 0309
- Cell 0379
- Ecology 0329
- Entomology 0353
- Genetics 0369
- Limnology 0793
- Microbiology 0410
- Molecular 0307
- Neuroscience 0317
- Oceanography 0416
- Physiology 0433
- Radiation 0821
- Veterinary Science 0778
- Zoology 0472

Biophysics
- General 0786
- Medical 0760

EARTH SCIENCES

Biogeochemistry 0425
Geochemistry 0996
Geodesy 0370
Geology 0372
Geophysics 0373
Hydrology 0388
Mineralogy 0411
Paleobotany 0345
Paleoecology 0426
Paleontology 0418
Paleozoology 0985
Palynology 0427
Physical Geography 0368
Physical Oceanography 0415

HEALTH AND ENVIRONMENTAL SCIENCES

Environmental Sciences 0768
Health Sciences
- General 0566
- Audiology 0300
- Chemotherapy 0992
- Dentistry 0567
- Education 0350
- Hospital Management 0769
- Human Development 0758
- Immunology 0982
- Medicine and Surgery 0564
- Mental Health 0347
- Nursing 0569
- Nutrition 0570
- Obstetrics and Gynecology .. 0380
- Occupational Health and Therapy 0354
- Ophthalmology 0381
- Pathology 0571
- Pharmacology 0419
- Pharmacy 0572
- Physical Therapy 0382
- Public Health 0573
- Radiology 0574
- Recreation 0575
- Speech Pathology 0460
- Toxicology 0383

Home Economics 0386

PHYSICAL SCIENCES

Pure Sciences

Chemistry
- General 0485
- Agricultural 0749
- Analytical 0486
- Biochemistry 0487
- Inorganic 0488
- Nuclear 0738
- Organic 0490
- Pharmaceutical 0491
- Physical 0494
- Polymer 0495
- Radiation 0754

Mathematics 0405
Physics
- General 0605
- Acoustics 0986
- Astronomy and Astrophysics 0606
- Atmospheric Science 0608
- Atomic 0748
- Electronics and Electricity 0607
- Elementary Particles and High Energy 0798
- Fluid and Plasma 0759
- Molecular 0609
- Nuclear 0610
- Optics 0752
- Radiation 0756
- Solid State 0611

Statistics 0463

Applied Sciences

Applied Mechanics 0346
Computer Science 0984
Engineering
- General 0537
- Aerospace 0538
- Agricultural 0539
- Automotive 0540
- Biomedical 0541
- Chemical 0542
- Civil 0543
- Electronics and Electrical 0544
- Heat and Thermodynamics ... 0348
- Hydraulic 0545
- Industrial 0546
- Marine 0547
- Materials Science 0794
- Mechanical 0548
- Metallurgy 0743
- Mining 0551
- Nuclear 0552
- Packaging 0549
- Petroleum 0765
- Sanitary and Municipal 0554
- System Science 0790

Geotechnology 0428
Operations Research 0796
Plastics Technology 0795
Textile Technology 0994

PSYCHOLOGY

General 0621
Behavioral 0384
Clinical 0622
Developmental 0620
Experimental 0623
Industrial 0624
Personality 0625
Physiological 0989
Psychobiology 0349
Psychometrics 0632
Social 0451

THE UNIVERSITY OF MANITOBA

FACULTY OF GRADUATE STUDIES

COPYRIGHT PERMISSION

NUMERICAL MODELLING FOR ELASTIC WAVES IN LAMINATED COMPOSITE PLATES

BY

JIUJING ZHU

A Thesis/Practicum submitted to the Faculty of Graduate Studies of the University of Manitoba in partial fulfillment of the requirements for the degree of

DOCTOR OF PHILOSOPHY

Jiujing Zhu © 1996

Permission has been granted to the LIBRARY OF THE UNIVERSITY OF MANITOBA to lend or sell copies of this thesis/practicum, to the NATIONAL LIBRARY OF CANADA to microfilm this thesis/practicum and to lend or sell copies of the film, and to UNIVERSITY MICROFILMS INC. to publish an abstract of this thesis/practicum..

This reproduction or copy of this thesis has been made available by authority of the copyright owner solely for the purpose of private study and research, and may only be reproduced and copied as permitted by copyright laws or with express written authorization from the copyright owner.

Abstract

Propagation and scattering of elastic waves in laminated composite plates are investigated with particular reference to ultrasonic nondestructive detection of flaws.

An analytical method and a stiffness method are formulated to study the two-dimensional wave propagation in laminated composite plates. Based on these methods, plane-strain elastodynamic Green's functions are obtained. Boundary element method is adopted to analyze scattering of waves by flaws in laminated composite plates. A new technique is established to evaluate the Cauchy Principal Value integrals and weakly singular integrals involved in the boundary integral equations. Also, a hybrid method, which combines the finite element formulation in a finite region and a wave modal representation outside, is presented with special attention to the analysis of inclusion or joint problems. The methods are illustrated through solving the problems of guided wave scattering by surface-breaking cracks, horizontal cracks (due to delamination), cracks on the interphase of joints. The frequency domain results and transient responses show that application of these methods in nondestructive evaluation technique is very promising.

Three-dimensional wave propagation and scattering phenomena are also studied. It is shown that three-dimensional wave propagation problems can be decomposed into a sequence of two-dimensional wave problems. Based on the decomposition technique, three-dimensional Green's functions are derived in a double summation form. The boundary element method is exploited in the analysis of three-dimensional wave scattering in isotropic plates.

Acknowledgements

I am deeply grateful to my advisor, Professor A.H. Shah, for suggesting the research topic and providing continued expert guidance up to completion of this study.

I would also like to express my grateful thanks to Professor E. Wilms and Professor D. W. Trim for providing helpful comments and serving the advisory committee. I convey my thanks to Professor S.B. Dong for devoting his time to serve as the external examiner. Sincere thanks are extended to Professor S.K. Datta for his fruitful suggestion and guidance.

My appreciation goes to my colleagues and friends, Dr. W.M. Karunasena, Dr. Y.M. Desai, Dr. Y. Wang, Dr. N. Rattanawangcharoen, and Ms. W. Zhuang for their help and encouragement.

Financial support received in the form of research assistantship from the NSERC and Ontario Hydro research grant of Professor Shah, a graduate fellowship from The University of Manitoba, and a teaching assistantship from the Department of Civil and Geological Engineering, are greatly appreciated.

Finally, I wish to express my gratitude to my wife, my son and my parents for their understanding, encouragement and support during the course of my Ph.D program.

Contents

Abstract i

Acknowledgements ii

List of Tables viii

List of Figures ix

1 Introduction 1

1.1 Composite materials 1

1.2 Nondestructive evaluation 3

1.3 Literature review 4

1.3.1 Dispersion relation 5

1.3.2 Numerical modelling 6

1.3.2.1 Hybrid method 6

1.3.2.2 Boundary element method 7

1.4 An overview of the present study 11

1.4.1 Wave propagation and Green's functions 11

1.4.2 Wave scattering 12

1.5 Organization of the thesis 13

2 Plane-strain Green's Functions **15**

2.1 General 15

2.2 Description of the problem 16

2.3 Governing equations 17

2.4 Wave function expansion method 18

2.4.1 Wave functions 18

2.4.2 Numerical difficulties at high frequencies 21

2.4.3 Amplitude coefficients of Green's functions 22

2.4.4 Numerical aspect 25

2.5 Rayleigh-Ritz type approximation approach 27

2.5.1 Approximate governing equations 27

2.5.2 Eigenvalue Problem 30

2.5.3 Modal summation technique 30

2.5.4 Green's functions 31

2.6 Numerical implementation 32

2.7 Concluding remarks 37

3 Plane-strain Wave Scattering **46**

3.1 General 46

3.2 Description of the problem 47

3.3 Hybrid method 48
3.3.1 Wave function expansion for exterior regions 48
3.3.2 Finite element model of interior region 50
3.3.3 Global solution 51
3.4 Boundary element method 53
3.4.1 Formulation 53
3.4.2 Evaluation of CPV and weakly singular integrals 56
3.4.3 Numerical aspect 58
3.4.4 Treatment of corner points 61
3.5 Application of BEM in crack problems 62
3.5.1 Difficulties in crack modelling 63
3.5.2 Multidomain technique 64
3.5.3 Crack-tip elements 66
3.6 Numerical applications 67
3.7 Concluding remarks 74

4 3-D Waves in Isotropic Plates **87**

4.1 General 87
4.2 Description of the problem 88
4.3 3-D wave propagation and Green's functions 89
4.3.1 Axisymmetric case 89
4.3.1.1 Governing equations 89

4.3.1.2 Wave functions 90
4.3.1.3 Hybrid method to compute Green's functions 92
4.3.2 General formulation 95
4.3.2.1 Decomposition of the problem 96
4.3.2.2 Green's functions 99
4.3.2.3 Solutions in (x, y, z) coordinate system 104
4.3.3 Numerical results for Green's functions 105
4.4 BEM for 3-D wave scattering 107
4.4.1 Formulation 107
4.4.2 Numerical results 108
4.5 Concluding remarks 110

5 3-D Green's Functions for Composite Plates **118**
5.1 General 118
5.2 Description of the problem 119
5.3 Governing Equations 120
5.4 Decomposition of the equations 123
5.5 Green's function 126
5.6 Numerical implementation 131
5.7 Concluding remarks 133

6 Concluding Remarks **140**
6.1 Conclusions 140
6.2 Recommendation for Future Work 141

References 143

A Coefficients of matrix $[P^{\Delta}]$ 151

List of Tables

2.1 Elastic properties of 0° and 90° Graphite/Epoxy fibers (GPa) 33

3.1 The diagonal block elements of **G** and **H**. 60

3.2 Cut–off frequencies in a 8-layered cross-ply composite plate. 73

5.1 Elastic properties of single layer Graphite/Epoxy fibers (GPa) 131

List of Figures

1.1 Schematic diagram of ultrasonic flaw detector. 14

2.1 Configuration of a laminated composite plate 16

2.2 Symmetric condition about loaded section 24

2.3 Vertical displacements along top surface, $\Omega = 1$ 35

2.4 Vertical displacements along top surface, $\Omega = 20$. (a) $Q_{\mathrm{L}} = 200$, $Q_{\mathrm{T}} = 100$; (b) $Q_{\mathrm{L}} = 2000$, $Q_{\mathrm{T}} = 1000$. 38

2.5 Vertical displacements along sections, $\Omega = 1$. (a) $x = 0.3H$; (b) $x = 10H$. 39

2.6 Vertical displacements along sections, $\Omega = 20$. (a) $x = 0.3H$; (b) $x = 10H$. 40

2.7 The dispersion relation of the single layered plate 41

2.8 Vertical displacements along sections in the single layered plate. (a) $\Omega = 1$, (b) $\Omega = 10$. 42

2.9 The dispersion relation of the 35-layered plate 43

2.10 Displacements along sections for 35-layered plate, $\Omega = 1$. (a) $x = 0.3H$; (b) $x = 10H$. 44

2.11 Displacements along sections for 35-layered plate, $\Omega = 10$. (a) $x = 0.3H$; (b) $x = 10H$. 45

3.1 Region division of a plate 48

3.2 Discretization of boundary into elements 55

3.3 Artificial source 56

3.4 Configuration of a semi-infinite plate 59

3.5 Configuration of corner points 61

3.6 Crack surface geometry 63

3.7 partitioning of a cracked body 65

3.8 Quarter-point crack-tip elements 67

3.9 Configuration of a surface-breaking crack 68

3.10 Configuration of a surface-breaking crack 69

3.11 Configuration of jointed composite plate 70

3.12 The configuration of load. (a) time–dependence, (b) frequency–dependence 75

3.13 Surface response spectra of points $(-0.25H, H)$ and $(5H, 0)$. 76

3.14 Vertical displacement at two sections for $\Omega = 1$, (a) $x = -1.4H$, (b) $x = 5H$. 77

3.15 Response spectra at top surface, (a) without crack, (b) with crack. 78

3.16 Top surface response at $\Omega = 1.57$. 79

3.17 Displacement spectrum at the origin. 80

3.18 Transient response of top surface, (a) without crack, (b) with crack. 81

3.19 Transient response of point (1.26H,0). 82

3.20 Frequency spectrum for 8-layer plate. 83

3.21 Dispersion curves for 8-layer composite plate. Solid lines: symmetric mode; dashed lines: antisymmetric mode. 84

3.22 Vertical displacement spectra of surface points. (a) point (-0.2H,0), (b) point (0.15H,0). 85

3.23 Transient response spectra of surface points. (a) point (-0.2H,0), (b) point (0.15H,0). 86

4.1 Configuration of an isotropic plate 88

4.2 Divided regions of an isotropic plate 94

4.3 Coordinate systems and wave traveling direction 97

4.4 Vertical displacements through thickness, $\Omega = 1$, (a) $x = 0.3H$, (b) $x = 10H$. 111

4.5 Vertical displacements through thickness, $\Omega = 10$, (a) $x = 0.3H$, (b) $x = 10H$. 112

4.6 Displacements through thickness, $\Omega = 1$, (a) $x = 0.3H$, (b) $x = 10H$. 113

4.7 Displacements through thickness, $\Omega = 10$, (a) $x = 0.3H$, (b) $x = 10H$. 114

4.8 Configuration of a rectangular crack 115

4.9 Crack-tip elements in 3-D analysis 115

4.10 Vertical displacement on the top surface at $\Omega = 1$. (a) without crack, (b) with crack. 116

4.11 Vertical displacement on the top surface at $\Omega = 1$. Plane-strain modelling. 117

5.1 Configuration of a 3-D laminated composite plate 119

5.2 Variation of wave numbers versus propagation direction in the single layered plate 134

5.3 Variation of top surface displacement in the single layer plate at 0° . 135

5.4 Variation of top surface displacement in the single layer plate at 45° 136

5.5 Variation of top surface displacement in the single layer plate at 90° 137

5.6 Variation of wave numbers versus propagation direction in the 8-layer plate 138

5.7 Variation of top surface displacement in the 8-layer plate 139

Chapter 1

Introduction

1.1 Composite materials

The word 'composite' in composite material signifies that two or more materials are combined on a macroscopic scale to form a useful material. The key is the macroscopic examination of a material. Different materials can be combined on a microscopic scale, such as in alloying, but the resulting material is macroscopically homogeneous. The advantage of composites is that they usually exhibit the best qualities of their constituents and often some qualities that neither constituent possesses.

Composite materials are often used in situations involving the sudden application of loads. The dynamic response of the structure ensues after load application, and a state of stress may be generated that leads to failure. It is necessary to understand the response characteristic of the material body to account properly for all important effects.

There are three commonly used types of composite materials [1], namely, *Fibrous composites*, *Particulate composites*, and *Laminated composites*.

Fibrous composites consist of fibers in a matrix. The fibers are characterized geometrically by their near crystal-sized diameters. Naturally, fibers are of little use unless they are bound together to take the form of a structural element which can take loads. The fibers may be organic or metallic. Examples of commonly used fibers are glass, graphite, boron, and aramid. The binder material is usually called a matrix. The purpose of the matrix is manifold: support, protect, transfer stress, etc. The matrix may be organic or metallic. Some examples of matrices are epoxy, polyester, and silicon. Typically, the matrix is of considerably lower density, stiffness, and strength than the fibers. However, the combination of fibers and a matrix can have very high strength and stiffness, yet still have low density.

Particulate composites are elemental or alloy matrices within which fine particles of one or more materials are dispersed. The particles can be either metallic or non-metallic as can the matrix. Commonly used particles are Al_2O_3, TnO_2, Cr_2O_3, SiO_2 and SIC.

Laminated composites are composed of layers or laminae of two or more materials bonded together. Lamination is used to combine the best aspects of the constituent layers in order to achieve a more useful material. The properties that can be emphasized by lamination are strength, stiffness, low weight, corrosion resistance, thermal insulation, acoustical insulation, etc. Examples of laminated composites are bimetals, clad metals, laminated glass, plastic based laminates and laminated fibrous-reinforced composites.

Laminated fibrous-reinforced composites are a hybrid class of composites involving both fibrous composites and lamination technique. Here, layers of fiber-reinforced material are built up with the fiber directions of each layer typically oriented in different directions to give different strengths and stiffnesses in the various directions. Thus, the strengths and stiffnesses of the laminated fiber-reinforced composite can be

tailored to the specific design requirements of the structural element being built.

The contents of this thesis will be mainly directed towards laminated and fibrous composites, although some of the principles to be discussed will have general applicability. A *laminated composite plate* is a plate which is constructed from laminae with various orientations of principal material axes in the laminae perfectly bonded together.

1.2 Nondestructive evaluation

Composite materials are ushering in a new era for material science and engineering due to their low density, increased service life, and high performance not obtainable with conventional engineering materials. The strength of composite structures is dependent on the elastic properties of the composite materials. However the presence of flaws or defects in the composite materials has a great influence on the strength. The growth of flaws in composite materials can have serious consequences during operation. In order to detect these flaws without impairing the usefulness of the composite structures, which are often in the form of plates, nondestructive evaluation (NDE) technique has been exploited. The testing technique may involve visual inspection, dye penetrant, magnetic particle, radiography, eddy current or ultrasonic.

The main idea of using ultrasonic waves in flaw detection is the scattering of waves by a flaw or other abrupt change in the elastic properties of the material in which the waves are travelling. A schematic diagram of a typical ultrasonic flaw detector is shown in Figure 1.1 (Page 14). Ultrasonic waves generated by the transducer travel through the specimen and are scattered when a flaw is encountered. Of particular interest are the scattered signals, which reach the surface of the specimen and are measured by receivers located on the surface. These signals carry a substantial amount

of information about the characteristic of the flaw, such as the size, shape, and location. Ultrasonic flaw detection techniques rely on the theoretical predictions of the signature of the scattered signals. Therefore, it is crucial to establish an appropriate theoretical model which can accurately predict the scattering by flaws.

Several ultrasonic techniques, such as pulse echo, transmission, resonance, frequency modulation, and acoustic image are available for nondestructive evaluation of plate-like specimens. Early techniques used body waves. Newer techniques employing guided waves are constantly under development. The important advantages of using guided waves in NDE are:

1. The dispersive and multimodal nature of the guided waves can be used to generate a large number of data points in a given frequency range.

2. The velocity of guided waves is very sensitive to the material properties of the plate.

3. The velocity of guided waves can be measured accurately as a function of frequency.

This thesis is concerned with the study of guided waves in laminated composite plates. In the ensuing section, a concise review of literature related to theoretical analysis and numerical modelling of these waves pertaining to the thesis topic is presented.

1.3 Literature review

The study of wave phenomena in laminated composite plates can be categorized as analysis of wave propagation in the plates and investigation of wave scattering by

inhomogenities. Dispersion characteristics of guided waves are important to understand wave propagation properties. Numerical algorithms are required to study the wave scattering phenomena. In this section, the literature survey is focussed on the study of dispersion relations and numerical modelling.

1.3.1 Dispersion relation

In order to exploit guided waves in ultrasonic testing for laminated plates, dispersion characteristics of these waves need to be understood. Dispersion characteristics of guided waves in an undamaged laminated composite plate are affected by many factors, the most important of which are: interfaces, fiber orientation in each lamina, number of layers, and effective material properties of each lamina.

The dispersion equation for a homogeneous isotropic plate was studied extensively by Mindlin [2] . Nayfeh and Chimenti [3] reviewed the literature and presented results for the dispersion of Lamb waves in a homogeneous anisotropic plate. Baylis and Green [4, 5] and Baylis [6] investigated analytical dispersion equations for two- or three-layer transversely isotropic plates.

Several approximate theories have been proposed to derive the dispersion relations in the form of generalized eigenvalue problems. The common ones are plate theories. A list of references on various refined plate theories can be found in [7, 8]. However, plate theories do not provide very accurate eigenvalues for wave velocities.

Dong and his co-workers [9, 10, 11] presented a Rayleigh-Ritz type approximation based stiffness method to analyze the wave propagation in laminated composite plates. In this method, the plate is discretized in the thickness direction with subdivision into mathematical sublayers. Quadratic interpolation polynomials are used to approximate the displacement variation in the thickness direction. Datta et al. [12] presented an approximate stiffness method applicable to a layered anisotropic plate

with an arbitrary number of layers. In their analysis, the continuity of both displacements and tractions are maintained. Karunasena et al. [13] made a systematic investigation of the effect of increasing the number of laminae on the dispersion of waves in a multilayered plate. For further references on previous studies of guided wave dispersion, the reader is referred to [14].

1.3.2 Numerical modelling

Ultrasonic testing technique relies on the information carried by the scattering waves. Many references on earlier work on problems of wave scattering by flaws are included in [15]. The edited volume of Datta et al. [14] is a good source of reference on recent works on this subject. Rokhlin [16, 17] analyzed the scattering of Lamb waves by a crack parallel to the surface of an isotropic plate using the modified Wiener-Hopf technique and the method of multiple diffractions. Tan and Auld [18] investigated the scattering of Lamb waves by a crack normal to the surface of an isotropic plate using the normal mode variation method. The application of these methods is extremely difficult, if not impossible, for flaws of arbitrary shape.

1.3.2.1 Hybrid method

Shah et al. [19] and Wong [20] presented a hybrid method combining an analytical procedure with a finite element modelling to study the scattering of horizontally polarized shear waves (SH waves) by arbitrarily shaped cracks and cavities in an isotropic half-space. Abduljabbar et al. [21] extended this hybrid method to analyze the scattering of SH waves in isotropic plates. Koshiba et al. [22] applied this technique to scattering of Lamb waves in isotropic plates. Paskaramoorthy et al. [23] employed the hybrid method to investigate scattering of slow flexural waves by cracks in isotropic plates. The hybrid method was also used by Bratton et al. [24] to study

the plane-strain wave scattering by a normal surface-breaking crack in a homogeneous (uniaxial) fiber-reinforced composite plate. In all these studies, the incident wave is assumed as a single wave emanating from infinity.

Ju and Datta [25] and Datta et al. [26] investigated scattering of Lamb waves, by using a hybrid method combining the finite element discretization of the near-field with boundary integral representation of the field outside a contour completely enclosing the crack. Bond [27] reviewed various applicable numerical techniques for a wave scattering problem, and recommended that the family of boundary methods are well suited for scattering by various defects.

1.3.2.2 Boundary element method

Two of the popular numerical methods which are used to perform the elastic stress analysis are the finite element method (FEM) and the boundary element method (BEM). The main disadvantage of the FEM is that a domain discretization is required to perform the analysis. The boundary element method involves discretization only of the boundary of the structure and the governing differential equation is solved analytically in the interior, leading to greater accuracy. However, the BEM generally leads to a nonsymmetric, fully populated system of equations, unlike the FEM which yields a symmetric, banded system of equations.

In the analysis of problems with cracks, the boundary element method is particularly attractive. The difficulties in FEM primarily stem from the stress field singularity ahead of the crack. Accurate approximation of the singular behavior demands highly refined discretization and specialized crack treatment, leading to a costly calculation. Moreover, a changing crack profile, as any problem which involves changing boundaries, requires that the discretization be redone at each step. Working solely with function values on the domain boundary, BEM should be able to

avoid the interior singularity and, therefore, circumvent these difficulties. However, since the boundary integrals involve singular kernels, the integrations have to be performed very carefully and the overall accuracy of the BEM is largely dependent on the precision with which the various integrals are evaluated.

Much research has been done and several techniques have been suggested to handle the singular integrals. A set of weighted Gaussian formulae [28] has been established to calculate the singular integrals. Degenerated co-ordinate transformation technique was applied by Lachat and Watson [29] to compute the weakly singular integrals and also the rigid body movement technique suggested by Cruse [30] was used to evaluate the Cauchy Principal Value (CPV) singular integrals indirectly. Semi-analytical method, wherein using asymptotic expansion of the kernel function with respect to the local co-ordinates such that the singular part can be subtracted out and integrated analytically, was suggested by Guiggiani [31]. A review of these techniques can be found in [32].

As is known, the direct boundary element method for a crack geometry fails: the discretization of the whole domain boundary, including both crack surfaces, yields a singular system of equations [33]. This follows from the observation that the integral equations generated by a pair of corresponding nodes on either side of the crack (i.e. occupying the same position in the space) are identical. Several strategies have been proposed for the boundary element analysis of crack problems. These methods include representing the crack as a notch, symmetric crack modelling, use of special Green's functions, and flat crack modelling. Representing the crack as a notch or replacing the crack plane with symmetry boundary conditions, i.e. symmetric crack modelling, removes the singularity in the algebraic system of equations [34]. It is, however, limited to symmetric crack problems. Representing the crack as a notch increases the modelling error due to the notch opening. The special Green's function approach [35] possesses the advantages that crack geometry and crack tip singularities are fully

embedded; no modelling of the crack surface is required. The disadvantage is that this approach works only for special cases since it requires quite a lot of preliminary analytic work to find the necessary Green's functions. Flat crack modelling [36] represents the displacements along the crack surface as the relative displacement between the two crack surfaces. This scheme has two critical deficiencies as a mathematical model for crack geometries, i.e. non-uniqueness of the boundary integral equation resulting from crack surface loading and the problem of two displacement variables along the crack. An extensive discussion of these modelling techniques is given by Cruse[33].

The most common general purpose, direct boundary element technique for treating cracks has been the multidomain approach [37]. This method decomposes the domain into subregions without cracks; the boundary element equations for each subregion, together with the conditions of compatibility of displacements and equilibrium of tractions across the fictitious boundaries, yield sufficient number of equations to solve the problem.

Many efforts have been devoted to evaluate the hypersingular integrals [38, 39] arising from the additional integral equation which expresses the boundary condition on the crack surface. Recently, a number of papers have viewed these integrals in a different manner, utilizing what is basically a regularization procedure to subtract out the most singular terms [40]. A brief review of the techniques to evaluate the hypersingular integrals was given by Huang and Cruse [32].

In the conventional application of the BEM, the Green's functions are full space fundamental solutions. Most of the techniques to evaluate the singular integrals are based on the explicit, analytical expressions of the displacements and stresses as $\sim lnr$ and $\sim r^{-1}$ in two dimensions, and as $\sim r^{-1}$ and $\sim r^{-2}$ in three dimensions, respectively, with r being the distance between the source and field points.

When the BEM is applied to analyze the wave scattering problem in laminated composites, the application of the full space Green's function is, if not impossible, extremely difficult [41]. It is not only because of the complexity in discretizing the interfaces between the different layers, but also because of the difficulties in deriving the explicit expression for the fundamental solution for infinite anisotropic media. It is crucial to derive Green's functions for laminated composite plates in the boundary element analysis of wave scattering.

Green's functions for isotropic plates have been extensively studied in the past. References to early literature can be found in [42].

A wavenumber integral technique using a quadrature scheme was developed by Xu and Mal [43, 44]. Recently Mal and Lih [45] have presented a wavenumber integral technique to study the waves in a composite plate due to a concentrated load. As discussed by them, this is a fairly time consuming process, even for a single lamina.

Most of the studies dealt with two dimensional problems (plane strain or plane stress). Ceranoglu and Pao [46], Weaver and Pao [47] studied the dynamic responses of isotropic plates to a vertical load where the axisymmetric condition holds. Three dimensional transient solution has been discussed by Vasudevan and Mal [48] , Liu et al. [49].

However, to the best of the author's knowledge, no efficient method to compute the three-dimensional Green's function has been yet published.

When the Green's functions for laminated composites are used in BEM, all the established techniques based on the analytical expressions of displacements and stresses to evaluate the singular integrals fail. The rigid body movement technique which was developed for static problem to evaluate the CPV integrals also fails since the displacement Green's functions for the laminated plates are singular at zero frequency [50]. No method has been reported to evaluate both the weakly and CPV singular integrals

when the Green's functions cannot be expressed in analytical, closed form.

1.4 An overview of the present study

The objective of the present study is to investigate propagation and scattering of guided waves in laminated composite plates with particular reference to developing algorithm for direct problem (not inverse) of flaw detection. The analysis is based on the assumption that the lateral dimensions of the plate are very large in comparison to the thickness of the plate. Of interest are the theoretical analysis and numerical studies of the plane-strain elastodynamic Green's functions of, and wave scattering by cracks or inhomogeneities in, laminated composite plates; three-dimensional wave propagation in laminated composite plates; and three-dimensional wave scattering in isotropic plates.

1.4.1 Wave propagation and Green's functions

Two models of wave propagation in laminated composite plates are presented in this study. The analytical formulation is employed for plane-strain analysis of laminated composite plates and axisymmetric analysis of isotropic plates. A Rayleigh-Ritz type approximation based stiffness method is used for both two- and three-dimensional analyses.

Based on the analytical formulation, a method is developed to compute the plane-strain elastodynamic Green's functions due to line loads in laminated composite plates by expressing them in terms of the guided wave modes. As is known, the numerical methods based on the direct implementation of the matrix method become unstable at high frequencies. To circumvent this difficulty, a modification of the matrix formulation as discussed by Dunkin [51] for isotropic material is employed and extended for

anisotropic material. It is shown that accurate computation of the Green's functions can be made both in the near and far fields by keeping not only the propagating modes, but also the non-propagating and evanescent modes, in the wave function expansion. Accuracy of the solution is assured by satisfaction of the energy conservation. In the stiffness method, the dispersion relation is obtained as a standard eigenvalue problem. The orthogonality relations of the left and right eigenvectors are used together with the modal summation technique to construct the plane-strain Green's functions.

The circular-crested wave propagation in an isotropic plate is studied by the analytical formulation. The dynamic response of the plate to a vertical point load is obtained by a hybrid method which combines the finite element representation and wave function expansion. Also, it is shown that the three-dimensional wave propagation problem in the isotropic plate can be decomposed into a series of plane-strain and antiplane wave problems. The three-dimensional elastodynamic Green's function is obtained in a modal summation form.

With the confidence from the analysis of three-dimensional wave propagation in isotropic plates, we investigate the three-dimensional wave phenomena in laminated composite plates. It is illustrated that the three-dimensional wave propagation problem in a laminated composite plate is composed of a series of two-dimensional wave problems. Based on the stiffness method and modal summation technique, Green's functions are obtained in a double summation form with respect to wave travelling directions and wavenumbers.

1.4.2 Wave scattering

A hybrid method is employed to investigate the time-harmonic plane-strain wave scattering problem in laminated composite plates. The method incorporates finite

element formulation in a bounded interior region which contains all the flaws with a modal representation in the exterior region. Continuity conditions for the displacements and forces are imposed at the nodes lying along the boundaries between the two regions. This results in a system of linear algebraic equations which is solved for the unknown modal amplitudes.

The boundary element method is applied to investigate the plane-strain wave scattering by cracks in laminated composite plates. A new technique is developed to evaluate the Cauchy Principal Value integrals and weakly singular integrals involved in the boundary integral equations. Numerical computations have shown the accuracy and reliability of the proposed technique. This technique, illustrated through two-dimensional examples, is extended to three-dimesional analysis. To circumvent the difficulties associated with the evaluation of hypersingular integrals due to the presence of cracks, the multidomain technique is adopted.

1.5 Organization of the thesis

This thesis is mainly concerned with the investigation of propagation and scattering of guided waves in laminated composite plates. An analytical formulation and an approximate model are presented in Chapter 2 to derive the dispersion relations and to construct the plane-strain elastodynamic Green's functions. The hybrid method and boundary element method to analyze the plane-strain wave scattering problem are presented in Chapter 3. The study of three-dimensional wave propagation and scattering by flaws in isotropic plates is presented in Chapter 4. The concepts and procedures described in Chapter 4 are extended in Chapter 5 to construct the three-dimensional Green's functions for laminated composite plates. Finally, conclusions and some recommendations for further study are outlined in Chapter 6.

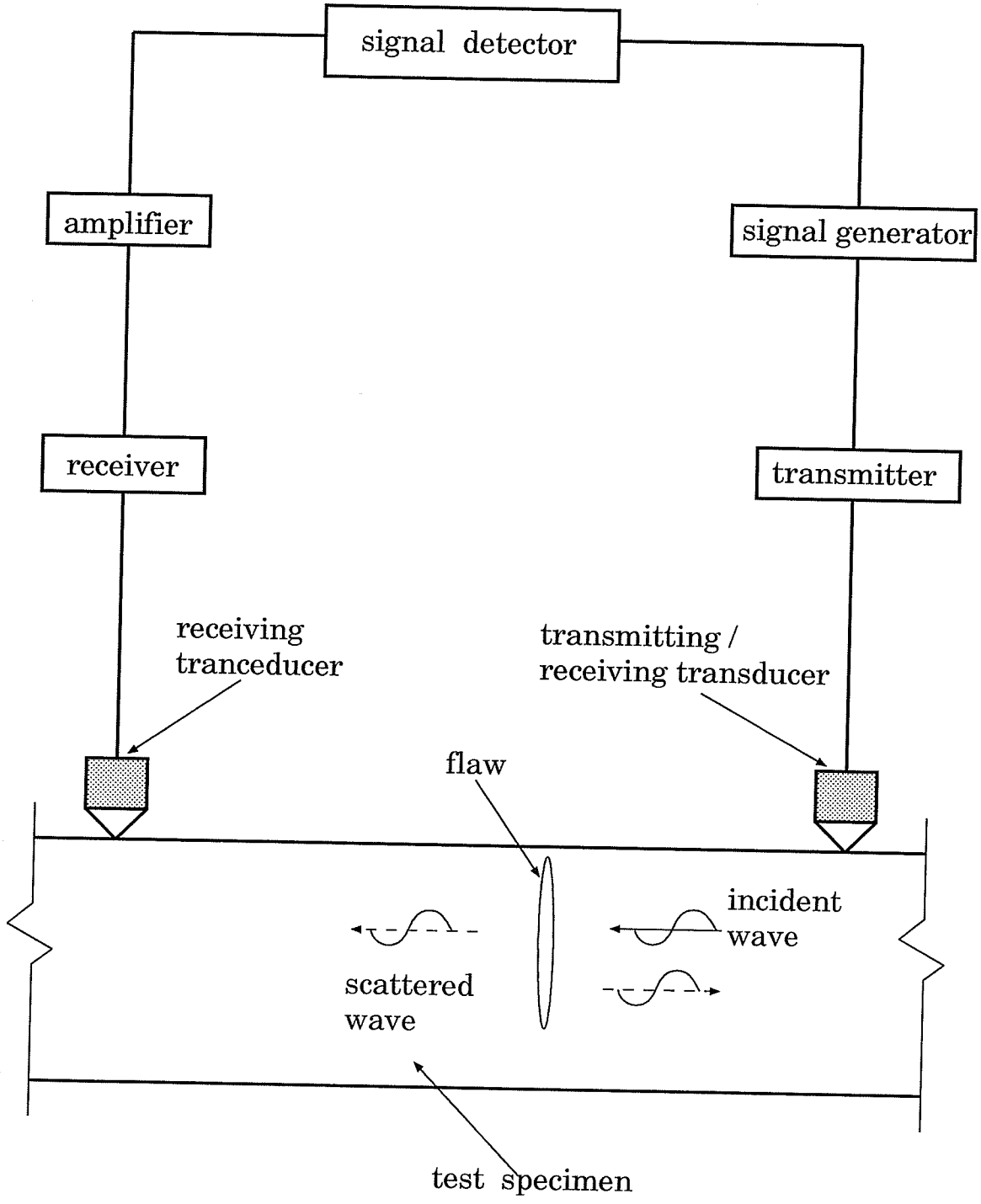

Figure 1.1: Schematic diagram of ultrasonic flaw detector.

Chapter 2

Plane-strain Green's Functions

2.1 General

The derivation of time-harmonic plane-strain Green's functions of laminated composite plates is considered in this chapter. As mentioned in Chapter 1, two models are developed: analytical formulation and Rayleigh–Ritz type approximation based stiffness method. In the analytical formulation, a modified propagator matrix approach is exploited to establish the frequency equation of the plate. Analytical wave functions are employed together with the symmetric/antisymmetric conditions along the loaded section of the plate to construct the Green's functions. In the stiffness method, the displacements are approximated by the interpolation of discrete nodal (interface) values. Fourier integral transforms are employed to obtain governing equations in wavenumber domain. The frequency equation of the plate is formulated in the form of a standard algebraic eigenvalue problem. The orthogonality properties of the right and left eigenvectors are employed to construct the Green's functions through a modal summation technique.

The accuracy of the methods is demonstrated by comparing the results with those

from wavenumber integral method for an isotropic plate. Numerical results for multilayed composite plates are also presented.

2.2 Description of the problem

Consider a laminated composite plate as shown in Figure 2.1. It is assumed to be composed of perfectly bonded laminae (layers) with possibly distinct mechanical properties and thicknesses. For simplicity, it will be assumed that each layer is orthotropic with symmetry axes parallel to the global coordinate axes (see Figure 2.1) x, y (not shown) and z. Plane strain deformation in the plane of xz will be considered here. To obtain the displacements at any point due to a unit load acting at a point in either the x or z direction each layer will be divided into several sub-layers so that the total number of sub-layers through the thickness $2H$ is N.

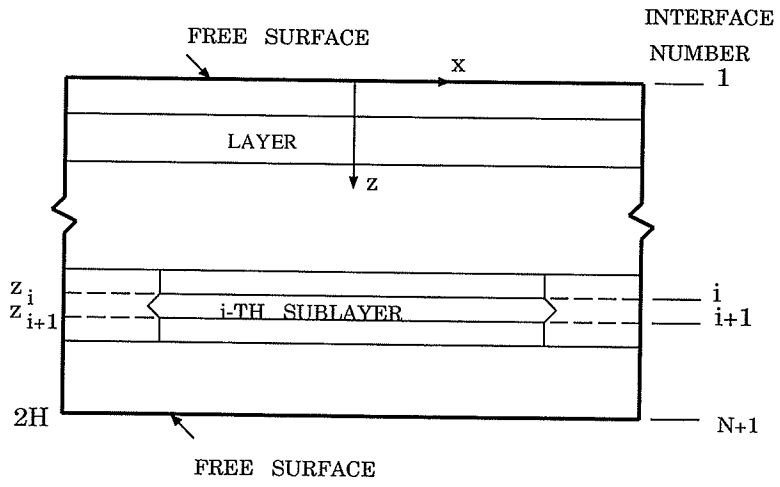

Figure 2.1: Configuration of a laminated composite plate

2.3 Governing equations

Consider the ith sub-layer bounded by $z = z_i$ and $z = z_{i+1}$. The strain-displacement relation is given by

$$\{\epsilon\} = \mathbf{L}\mathbf{u} \tag{2.1}$$

where

$$\mathbf{u}^T = \{\, u \quad w \,\} \tag{2.2}$$

u and w are displacements in x and z directions, respectively,

$$\mathbf{L}^T = \begin{bmatrix} \frac{\partial}{\partial x} & 0 & \frac{\partial}{\partial z} \\ 0 & \frac{\partial}{\partial z} & \frac{\partial}{\partial x} \end{bmatrix} \tag{2.3}$$

and

$$\{\epsilon\}^T = \{\, \epsilon_{xx} \quad \epsilon_{zz} \quad \epsilon_{zx} \,\} \tag{2.4}$$

where ϵ_{ij} is the strain component. The stress-strain relation in this sub-layer is given by

$$\{\sigma\} = \mathbf{D}\{\epsilon\} \tag{2.5}$$

where

$$\mathbf{D} = \begin{bmatrix} D_{11} & D_{13} & 0 \\ D_{13} & D_{33} & 0 \\ 0 & 0 & D_{55} \end{bmatrix} \tag{2.6}$$

and

$$\{\sigma\}^{\mathrm{T}} = \{\, \sigma_{xx} \quad \sigma_{zz} \quad \sigma_{zx} \,\} \tag{2.7}$$

where σ_{ij} is the stress component; D_{ij} is an element of the constitutive matrix $\mathbf{D}$ for the sub-layer.

The equations of harmonic motion in frequency domain can be expressed in terms of displacements $u(x, z)$ and $w(x, z)$ as

$$D_{11}\frac{\partial^2 u}{\partial x^2} + D_{55}\frac{\partial^2 u}{\partial z^2} + (D_{13} + D_{55})\frac{\partial^2 w}{\partial x \partial z} + b_x \;=\; -\rho\omega^2 u$$

$$D_{33}\frac{\partial^2 w}{\partial x^2} + D_{55}\frac{\partial^2 w}{\partial z^2} + (D_{13} + D_{55})\frac{\partial^2 u}{\partial x \partial z} + b_z = -\rho\omega^2 w \tag{2.8}$$

where b_x and b_z are body forces in x and z directions, respectively, ρ the mass density, and ω the circular frequency.

2.4 Wave function expansion method

In this section, the analytical frequency equation is derived based on a modified propagator matrix approach, and Green's functions are obtained by applying the symmetric/antisymmetric conditions along the loaded section of the plate.

2.4.1 Wave functions

The appropriate solution to the homogeneous equation from (2.8) are:

$$\begin{aligned} u &= jk(\Omega_1^+ + b\Omega_2^+)e^{jkx}, \\ w &= (ar_1\Omega_1^- + r_2\Omega_2^-)e^{jkx} \end{aligned} \tag{2.9}$$

where $j = \sqrt{-1}$, and

$$\begin{aligned} \Omega_1^+ &= A_{11}cosr_1z + A_{12}sinr_1z, \\ \Omega_1^- &= A_{12}cosr_1z - A_{11}sinr_1z, \\ \Omega_2^+ &= A_{21}cosr_2z + A_{22}sinr_2z, \\ \Omega_2^- &= A_{22}cosr_2z - A_{21}sinr_2z \end{aligned} \tag{2.10}$$

$$\begin{aligned} a &= (k_2^2 - \bar{\alpha}k^2 - r_1^2)/\bar{\delta}r_1^2, \\ b &= (k_2^2 - k^2 - \bar{\beta}r_2^2)/\bar{\delta}k^2 \end{aligned} \tag{2.11}$$

$$\bar{\alpha} = \frac{D_{11}}{D_{55}};\ \bar{\beta} = \frac{D_{33}}{D_{55}};\ k_2 = \sqrt{\frac{\rho\omega^2}{D_{55}}};\ \bar{\delta} = 1 + \frac{D_{13}}{D_{55}} \tag{2.12}$$

r_1 and r_2 are the roots of the equation

$$\begin{vmatrix} r^2 + \bar{\alpha}k^2 - k_2^2 & \bar{\delta}r^2 \\ \bar{\delta}k^2 & k^2 - k_2^2 + \bar{\beta}r^2 \end{vmatrix} = 0 \tag{2.13}$$

A_{11}, A_{12}, A_{21} and A_{22} are the arbitrary constants for the sub-layer. Stress and displacement components of the sub-layer can be expressed in terms of these four unknown constants. Evaluating the stresses and displacements at $z = z_i$ and $z = z_{i+1}$, after some manipulations, the following relation can be obtained:

$$\mathbf{Q}_{i+1} = [P_i]\mathbf{Q}_i \tag{2.14}$$

where

$$\mathbf{Q}_i^{\mathrm{T}} = \langle\, u_i \quad w_i \quad \sigma_{zzi} \quad \sigma_{zxi} \,\rangle\,. \tag{2.15}$$

The vector $\mathbf{Q}_i$, which is unknown yet, represents the displacement and stress components at $z = z_i$; and $[P_i]$ is the propagator matrix for the ith sub-layer. The elements of $[P_i]$ are given in [52].

The global propagator matrix $[P]$ for the entire plate is obtained by the repeated application of equation (2.14) as

$$\mathbf{Q}_{N+1} = [P]\mathbf{Q}_1 \tag{2.16}$$

where

$$[P] = [P_N][P_{N-1}]\cdots[P_i]\cdots[P_2][P_1]. \tag{2.17}$$

The repeated application of equation (2.14) ensures continuity of the displacement components u and w, and stress components σ_{zz} and σ_{zx}, at the faces between sublayers. Denoting the elements of the 4 by 4 matrix $[P]$ by P_{mn} $(m, n = 1, 2, 3, 4)$

and invoking the zero traction conditions at faces 1 and $(N+1)$, the following can be obtained from equation (2.16):

$$\begin{bmatrix} P_{31} & P_{32} \\ P_{41} & P_{42} \end{bmatrix} \begin{Bmatrix} u_1 \\ w_1 \end{Bmatrix} = \begin{Bmatrix} 0 \\ 0 \end{Bmatrix} \tag{2.18}$$

Note that there is as yet no external load acting on the plate. The dispersion equation (frequency equation) for the plate is obtained by setting the determinant of the coefficient matrix to zero as

$$f(\omega, k) = \begin{vmatrix} P_{31} & P_{32} \\ P_{41} & P_{42} \end{vmatrix} = 0. \tag{2.19}$$

Let M be the total number of modes to be used in the modal expansion of $\mathbf{Q}_i$ and k_m be the mth root of equation (2.19). Traction free conditions at face 1 and equation (2.18) give the components of the mth eigenvector at face 1, as

$$\mathbf{Q}_{1m}^{\mathrm{T}} = \langle\, 1, \quad -P_{31}/P_{32}, \quad 0, \quad 0 \,\rangle \tag{2.20}$$

Then, applying equation (2.14) at successive interfaces, the mth mode eigenvector can be obtained as

$$\mathbf{Q}_m^{\mathrm{T}} = \langle\, \mathbf{Q}_{1m}^{\mathrm{T}}, \quad \mathbf{Q}_{2m}^{\mathrm{T}}, \quad \ldots, \quad \mathbf{Q}_{im}^{\mathrm{T}}, \quad \ldots, \quad \mathbf{Q}_{(N+1)m}^{\mathrm{T}} \,\rangle \tag{2.21}$$

where

$$\mathbf{Q}_{im}^{\mathrm{T}} = \langle\, u_{im}, \quad w_{im}, \quad \sigma_{zzim}, \quad \sigma_{zxim} \,\rangle \tag{2.22}$$

$u_{im}, w_{im}, \sigma_{zzim}$ and σ_{zxim} are components of mth eigenvector at the ith interface. It may be noted that $\mathbf{Q}_{im}$ can be associated with propagating, non-propagating or evanescent modes corresponding to real, imaginary or complex k_m.

2.4.2 Numerical difficulties at high frequencies

Two numerical difficulties encountered by Dunkin [51] for isotropic material also arise here in the high frequency region. The first involves evaluation of the roots of equation (2.19), while the second is concerned with the computing of eigenvectors according to equation (2.14). It is known that the dispersion equation (2.19) can be manipulated in the form $(\bar{a} - \bar{b})f$, where f are products of like trigonometric functions (which are $sin^2 r_j h_i$, $sinr_j h_i cosr_j h_i$, $cos^2 r_j h_i$, $j = 1, 2$, h_i is the thickness of ith sub-layer) which may become very large at high frequencies. Analytically $\bar{a}$ and $\bar{b}$ are equal, but in numerical calculations small roundoff errors in $\bar{a}$, $\bar{b}$ may be sufficiently magnified by their large multiplier to dominate the results. In order to avoid the numerical difficulties, a modification of the matrix formulation which was first introduced by Dunkin [51] is adopted here. In this method, a 6×6 delta matrix $[A^{\Delta}]$ containing all 2×2 subdeterminants of the 4×4 matrix $[A]$ is constructed so that the elements of $[A^{\Delta}]$ are related to those of $[A]$ through

$$A^{\Delta}_{mn} = A^{pq}_{rs} = A_{pr}A_{qs} - A_{ps}A_{qr} \tag{2.23}$$

where the paired indices pq, rs take on the values 12,13,14,23,24,34 corresponding to the values of m or $n = 1, 2, 3, 4, 5, 6$. It can be easily verified that for matrix $[P]$ in equation (2.17):

$$[P^{\Delta}] = [P^{\Delta}_N][P^{\Delta}_{N-1}]...[P^{\Delta}_i]...[P^{\Delta}_1]. \tag{2.24}$$

Expressions for the elements of $[P^{\Delta}_i]$ (given in the Appendix A) show that the subdeterminants of the propagator matrix do not suffer from the difficulties associated with P_{ij}. Using equations (2.23) and (2.24), the dispersion relation (2.19) can be rewritten as:

$$P^{\Delta}_{61} = 0. \tag{2.25}$$

Therefore the numerical difficulties involved in satisfying the dispersion relation are avoided by making use of the algebraic expression for the subdeterminants of the $[P_i]$

as the basis of calculation.

The next task is the calculation of the mode vectors. First we define

$$P_{mn} = s_{mk} t_{kn} \tag{2.26}$$

where P_{mn} is the element of $[P]$ in equation (2.17), and

$$\begin{aligned} t_{mn} &= p^i_{ma} p^{i-1}_{ab} ... p^1_{rn}, \\ s_{mn} &= p^N_{ma} p^{N-1}_{ab} ... p^{i+1}_{rn} \end{aligned} \tag{2.27}$$

p^i_{mn} is element of $[P_i]$. Then equations (2.14) and (2.20) give:

$$\mathbf{Q}_{i+1} = \frac{1}{P_{32}} [P_i][P_{i-1}]...[P_1]\hat{\mathbf{Q}} \tag{2.28}$$

where

$$\hat{\mathbf{Q}}^{\mathrm{T}} = \langle\, P_{32}, \quad -P_{31}, \quad 0, \quad 0 \,\rangle\,. \tag{2.29}$$

Using equations (2.26) and (2.27) in (2.28), one finds:

$$Q_{i+1,a} = \frac{1}{P_{32}} (t_{a1} s_{3b} t_{b2} - t_{a2} s_{3b} t_{b1}) \tag{2.30}$$

that is:

$$Q_{i+1,a} = \frac{1}{P_{32}} s_{3b} t^{ab}_{12} \tag{2.31}$$

where $Q_{i+1,a}$ is the ath element of $\mathbf{Q}_{i+1}$. Then the mode vectors can be computed according to equation (2.31) without precision problems since they have nonzero coefficients.

2.4.3 Amplitude coefficients of Green's functions

The displacement vector $\mathbf{q}_x$, at arbitrary $x \geq 0$, can be approximated by the modal sum of a finite number of modes M in the form

$$\mathbf{q}_x = \sum_{m=1}^{M} A_m \mathbf{q}_m e^{j k_m x} \tag{2.32}$$

where A_m is the amplitude of mth mode,

$$\mathbf{q}_m^{\mathrm{T}} = \langle\, u_{1m}, \quad ..., \quad u_{im}, ..., \quad u_{(N+1)m}, \; w_{1m}, \quad ..., \quad w_{im}, ..., \quad w_{(N+1)m} \quad \rangle\,. \tag{2.33}$$

It may be noted that the displacement elements in (2.33) are arranged according to the order of degree of freedom, *i.e.*, the displacements in x-direction first, then the displacements in z-direction.

The force vector $\mathbf{f}_x$ at $x \geq 0$ can be expressed as

$$\mathbf{f}_x = \sum_{m=1}^{M} A_m \mathbf{f}_m e^{jk_m x} \tag{2.34}$$

where

$$\mathbf{f}_m^{\mathrm{T}} = \langle\, f_{x1m}, \quad ..., \quad f_{xim}, ..., \quad f_{x(N+1)m}, f_{z1m}, \quad ..., \quad f_{zim}, ..., \quad f_{z(N+1)m} \quad \rangle\,, \tag{2.35}$$

f_{xim} and f_{zim} are the force shape modes representing x and z direction forces at ith interface formed using the constitutive equation and the consistent load vector formulation [53]. The explicit form of f_{xim} and f_{zim} can be found in [52].

The displacement field at $x = 0$ is obtained as

$$\mathbf{q}_0 = [E]\mathbf{A} \tag{2.36}$$

where

$$\begin{aligned} [E] &= [\,\mathbf{q}_1, \quad \mathbf{q}_2, \quad ..., \quad \mathbf{q}_M\,] \\ \mathbf{A}^{\mathrm{T}} &= \langle\, A_1, \quad A_2, \quad ..., \quad A_M \,\rangle \end{aligned} \tag{2.37}$$

[E] is a $2(N+1)$ by M matrix, $\mathbf{A}$ is a vector with dimension M.

The force vector at $x = 0$ can be formed as

$$\mathbf{f}_0 = [F]\mathbf{A} \tag{2.38}$$

where

$$[F] = [\,\mathbf{f}_1, \quad \mathbf{f}_2, \quad ..., \quad \mathbf{f}_M\,] \tag{2.39}$$

is a rectangular matrix of size $2(N+1)$ by M.

Suppose a concentrated load acts at point $(0, z_0)$, and let L denote the interface number at which the load acts. For a z direction unit load, we have symmetric conditions with respect to vertical plane $x = 0$ (Figure 2.2):

$$\begin{aligned} \mathbf{q}_0^{\mathrm{T}} &= \langle\, 0, \quad 0, \quad ..., \quad 0, \quad w_1, \quad w_2, \quad ..., w_i, \quad ..., \quad w_{N+1}\,\rangle\,, \\ \mathbf{f}_0^{\mathrm{T}} &= \langle\, f_{x1}, \quad ..., \quad f_{xi}, ..., \quad f_{x(N+1)}, 0, \quad ..., 0, \quad 1/2, \quad ..., \quad 0\,\rangle \end{aligned} \tag{2.40}$$

where f_{xi} is the force in the x direction at ith interface at $x = 0$, and $1/2$ is located at the $(N+1+L)th$ row of $\mathbf{f}_0$.

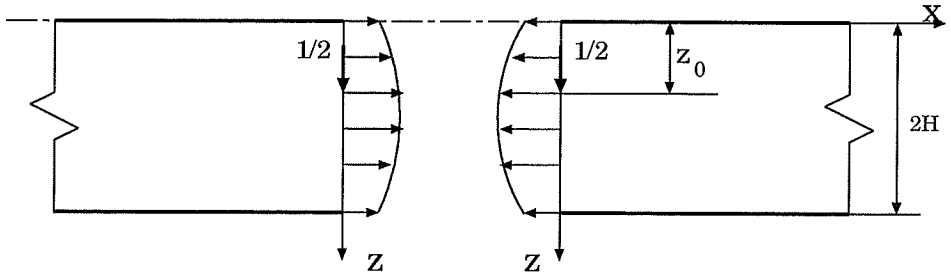

Figure 2.2: Symmetric condition about loaded section

Equations (2.36) and (2.38) can be written as follows according to equation (2.40),

$$\begin{bmatrix} E_{11} & E_{12} \\ E_{21} & E_{22} \end{bmatrix} \mathbf{A} = \begin{bmatrix} \mathbf{0} \\ \mathbf{q}_{02} \end{bmatrix} \tag{2.41}$$

$$\begin{bmatrix} F_{11} & F_{12} \\ F_{21} & F_{22} \end{bmatrix} \mathbf{A} = \begin{bmatrix} \mathbf{f}_{01} \\ \mathbf{f}_{02} \end{bmatrix} \tag{2.42}$$

where $[E_{ij}]$ and $[F_{ij}]$ $(i, j = 1, 2)$ are $(N+1)$ by M matrices, $\mathbf{0}$, $\mathbf{q}_{02}$ and $\mathbf{f}_{0i}$ $(i = 1, 2)$ are $(N+1)$ dimensional vectors.

By combining the first half of equation (2.41) and second half of equation (??), we obtain:

$$[H]\mathbf{A} = \mathbf{r} \tag{2.43}$$

where

$$[H] = \begin{bmatrix} E_{11} & E_{12} \\ F_{21} & F_{22} \end{bmatrix}; \quad \mathbf{r} = \begin{bmatrix} \mathbf{0} \\ \mathbf{f}_{02} \end{bmatrix}. \tag{2.44}$$

By applying the principle of virtual displacement, the amplitude coefficients can be obtained as:

$$\mathbf{A} = [[\bar{H}^-]^{\mathrm{T}}[H]]^{-1}[\bar{H}^-]^{\mathrm{T}}\mathbf{r} \tag{2.45}$$

where

$$[H^-] = \begin{bmatrix} F_{11} & F_{12} \\ E_{21} & E_{22} \end{bmatrix} \tag{2.46}$$

and overbar refers to the complex conjugate.

Applying similar procedure to x-direction unit load, we obtain vector $\mathbf{A}$ from equation (2.45) by replacing

$$\mathbf{r} = \begin{bmatrix} \mathbf{f}_{01} \\ \mathbf{0} \end{bmatrix}; [H] = \begin{bmatrix} F_{11} & F_{12} \\ E_{21} & E_{22} \end{bmatrix}; [H^-] = \begin{bmatrix} E_{11} & E_{12} \\ F_{21} & F_{22} \end{bmatrix}. \tag{2.47}$$

Once the amplitudes, A_m, are known, the displacement and stress field anywhere in the plate (Green's functions) can be computed using equation (2.32) and constitutive relations. Thus, for a fixed location of source point, evaluation of the Green's functions is a matter of summation of series, and the numerical difficulties associated with the infinite wavenumber integrals are avoided.

2.4.4 Numerical aspect

Wavenumber determination

For a fixed value of the frequency ω, $f(\omega, k)$ in equation (2.19) (or (2.25)) is a transcendental function of the wavenumber, k. There are three different kinds of roots: real, imaginary and complex. The real roots represent the propagating modes which dominate the dynamic response of the plate. The imaginary and complex roots represent nonpropagating and evanescent modes, respectively, and these modes decay with x. As reported by Gregory and Gladwell [54], the admissible k are those real roots with positive group velocity and those non-real roots with $\mathrm{Im}(k) > 0$. These conditions ensure that the waves produce bounded displacement and stress field throughout the plate for waves travelling in positive x direction. Muller's method [55] is employed here. At first, the plate is divided into a sufficiently large number of sub-layers and the approximate roots are obtained via Dong's method [11] as illustrated in the next section. Those approximate roots are used as initial guesses in Muller's method to accurately determine the exact roots.

Assessment of numerical accuracy

Energy is carried only by the propagating modes. The time-averaged value of the energy flux associated with the mth propagating mode through the plate cross section is given by

$$I_m = \omega |A_m|^2 Im[\mathbf{f}_m^{\mathrm{T}} \cdot \bar{\mathbf{q}}_m]. \tag{2.48}$$

where overbar represents complex conjugate.

The input energy due to the unit load is

$$I^{in} = \omega Im[\bar{q}] \tag{2.49}$$

where q is the displacement of the loading point in the direction of the unit load.

Let us define the percentage error in energy balance, ϵ, as

$$\epsilon = \frac{100}{I^{in}}[\frac{1}{2} I^{in} - \sum_{m=1}^{M_p} I_m] \tag{2.50}$$

where M_p is the total number of propagating modes. The principle of energy conservation requires that ϵ should be zero. This condition is used to assess the numerical accuracy of our analysis.

2.5 Rayleigh-Ritz type approximation approach

A Rayleigh-Ritz type approximation based stiffness method was presented by Dong and his co-workers [9, 10, 11] for wave propagation analysis in laminated anisotropic media. In this technique, variations of the displacements along thickness are approximated by quadratic functions of a thickness variable. The generalized coordinates in this representation are the displacements at the top, middle, and bottom of each mathematical layer (sub-layer). The frequency equation of the plate is formulated in the form of an eigenvalue problem. The orthogonality properties of the eigenvectors are applied to construct the Green's functions through a modal summation technique.

2.5.1 Approximate governing equations

The stiffness method starts with dividing each layer into several sublayers so that the total number of sublayers through the thickness of the plate is N. By using the interpolation polynomials in the z direction, the displacement components in a typical sub-layer with thickness h can be approximated as

$$\mathbf{u} = \mathbf{N}(\zeta)\mathbf{q}(x) \tag{2.51}$$

where $\mathbf{N}$ is the shape function matrix given by

$$\mathbf{N} = [\,(1 - 3\zeta + 2\zeta^2)\mathbf{I} \quad 4(\zeta - \zeta^2)\mathbf{I} \quad (2\zeta^2 - \zeta)\mathbf{I}\,] \tag{2.52}$$

and

$$\zeta = \frac{Z}{h}.$$

In the above, $\mathbf{I}$ is a 2 by 2 identity matrix, Z is a local coordinate originating at the top of the sub-layer, while $\mathbf{q}$ is the displacement vector at $Z = 0, h/2$ and h as follows:

$$\mathbf{q}^T = \langle\, \mathbf{q}_t^T \quad \mathbf{q}_m^T \quad \mathbf{q}_b^T \,\rangle \tag{2.53}$$

where

$$\mathbf{q}_i^T = \langle\, u \quad w \,\rangle_i \quad (i = t, m, b) \tag{2.54}$$

t, m and b represent top, middle and bottom surfaces of the sub-layer, respectively.

The approximate equation of motion for the sub-layer is obtained by following conventional finite element analysis procedure as:

$$\mathbf{f} = (-\omega^2 \mathbf{m} + \mathbf{k})\mathbf{q} \tag{2.55}$$

where

$$\mathbf{k} = -\mathbf{k}_1 \frac{\mathrm{d}^2}{\mathrm{d}x^2} + \mathbf{k}_2 \frac{\mathrm{d}}{\mathrm{d}x} + \mathbf{k}_3 \tag{2.56}$$

matrices $\mathbf{m}$ and $\mathbf{k}_i, (i = 1, 2, 3)$ are mass matrix and stiffness matrices [9]. The vector $\mathbf{f}$ is a force vector given by

$$\mathbf{f} = \mathbf{t} + \int_0^h \mathbf{N}^T \mathbf{b} dZ \tag{2.57}$$

$\mathbf{t}$ is the external traction vector; $\mathbf{b}$ is the body force vector.

The governing equation for the entire plate is obtained by summation over all the sublayers as:

$$\mathbf{F} = (\mathbf{K} - \omega^2 \mathbf{M})\mathbf{Q} \tag{2.58}$$

where

$$\mathbf{K} = -\mathbf{K}_1 \frac{\mathrm{d}^2}{\mathrm{d}x^2} + \mathbf{K}_2 \frac{\mathrm{d}}{\mathrm{d}x} + \mathbf{K}_3 \tag{2.59}$$

the matrices $\mathbf{M}$ and $\mathbf{K}_i (i = 1, 2, 3)$ are the results of overlapping the contributions of $\mathbf{m}$ and $\mathbf{k}_i (i = 1, 2, 3)$ for neighbouring sublayers, respectively. The vectors $\mathbf{Q}$ and $\mathbf{F}$ represent the nodal displacements and tractions, respectively. The dimensions of $\mathbf{Q}$ and $\mathbf{F}$ are M, and the sizes of matrices $\mathbf{M}$ and $\mathbf{K}$ are M by M, where $M = 2\times(2N+1)$. Note that the matrices $\mathbf{M}$, $\mathbf{K}_1$, and $\mathbf{K}_3$ are symmetric, whereas $\mathbf{K}_2$ is antisymmetric.

Introduce the Fourier integral transform with respect to x coordinate defined as [56]

$$\tilde{f}(k, z) = \int_{-\infty}^{\infty} f(x, z) e^{-jkx} dx \tag{2.60}$$

and the inverse formula defined by

$$f(x, z) = \frac{1}{2\pi} \int_{-\infty}^{\infty} \tilde{f}(k, z) e^{jkx} dk \tag{2.61}$$

where k is the transform parameter.

The application of Fourier transform to equation (2.58) results in the governing equation in transformed wavenumber domain as:

$$\tilde{\mathbf{F}} = (k^2\mathbf{K}_1 - jk\mathbf{K}_2 + \mathbf{K}_3 - \omega^2\mathbf{M})\tilde{\mathbf{Q}} \tag{2.62}$$

where $\tilde{\mathbf{F}}$ and $\tilde{\mathbf{Q}}$ are the Fourier transforms of $\mathbf{F}$ and $\mathbf{Q}$.

The above equation can be arranged in the form:

$$\mathbf{p} = [\mathbf{A} - k\mathbf{B}]\mathbf{d} \tag{2.63}$$

where

$$\mathbf{A} = \begin{bmatrix} \mathbf{0} & \mathbf{I} \\ \mathbf{K}_3^* & -j\mathbf{K}_2 \end{bmatrix} \qquad \mathbf{B} = \begin{bmatrix} \mathbf{I} & \mathbf{0} \\ \mathbf{0} & -\mathbf{K}_1 \end{bmatrix}, \tag{2.64}$$

$$\mathbf{p}^T = \begin{Bmatrix} \mathbf{0} & \tilde{\mathbf{F}} \end{Bmatrix}^T \qquad \mathbf{d}^T = \begin{Bmatrix} \tilde{\mathbf{Q}} & k\tilde{\mathbf{Q}} \end{Bmatrix}^T \tag{2.65}$$

and

$$\mathbf{K}_3^* = \mathbf{K}_3 - \omega^2\mathbf{M}$$

2.5.2 Eigenvalue Problem

When the external force is zero, *i.e.* $\tilde{\mathbf{F}} = \mathbf{0}$, equation (2.62) gives

$$(k^2\mathbf{K}_1 - jk\mathbf{K}_2 + \mathbf{K}_3^*)\tilde{\mathbf{Q}} = 0 \tag{2.66}$$

A nontrivial solution can be obtained by setting the determinant of the coefficient matrix to zero. This results in the dispersion relation to solve for the eigenvalues k. In other words, k for a given ω is found by treating equation (2.66) as a second order eigenvalue problem about k.

According to equation (2.63), both the right and left eigenvalue equations are obtained as:

$$[\mathbf{A} - k_m\mathbf{B}]\mathbf{\Phi}_m^R = 0; \quad 0 = \mathbf{\Phi}_m^L[\mathbf{A} - k_m\mathbf{B}] \tag{2.67}$$

where $\mathbf{\Phi}_m^R$ and $\mathbf{\Phi}_m^L$ are right and left eigenvectors, respectively.

It is noted that equation (2.67) yields 2M eigenvalues and eigenvectors. The two halfs decay in the $\pm x$-directions towards $\pm\infty$ [57].

The orthogonality condition of the right and left eigenvectors are:

$$\mathbf{\Phi}_n^L\mathbf{B}\mathbf{\Phi}_m^R = B_n\delta_{nm}; \quad \mathbf{\Phi}_n^L\mathbf{A}\mathbf{\Phi}_m^R = k_nB_n\delta_{nm} \tag{2.68}$$

where

$$B_n = \mathbf{\Phi}_n^L\mathbf{B}\mathbf{\Phi}_n^R; \quad n, m = 1, 2, ..., 2M$$
$$\delta_{nm} = \begin{cases} 1 & n = m \\ 0 & n \neq m \end{cases}$$

2.5.3 Modal summation technique

Modal summation technique [58] is employed here to obtain the solution to equation (2.63). Expressing $\mathbf{d}$ in terms of the right eigenvectors,

$$\mathbf{d} = \sum_{m=1}^{2M} \alpha_m\mathbf{\Phi}_m^R \tag{2.69}$$

substituting the above equation into (2.63) yields

$$\mathbf{p} = \sum_{m=1}^{2M} \alpha_m [\mathbf{A} - k\mathbf{B}] \mathbf{\Phi}_m^R. \tag{2.70}$$

Multiplying both sides with $\mathbf{\Phi}_n^L$ gives

$$\mathbf{\Phi}_n^L \mathbf{p} = \sum_{m=1}^{2M} \alpha_m [\mathbf{\Phi}_n^L \mathbf{A} - k\mathbf{\Phi}_n^L \mathbf{B}] \mathbf{\Phi}_m^R. \tag{2.71}$$

Applying orthogonality condition (2.68) to equation (2.71) results in:

$$\alpha_n = \frac{\mathbf{\Phi}_n^L \mathbf{p}}{(k_n - k)B_n} \tag{2.72}$$

The solution to (2.63) is obtained by substituting (2.72) into (2.69):

$$\mathbf{d} = \sum_{m=1}^{2M} \frac{\mathbf{\Phi}_m^L \mathbf{p} \mathbf{\Phi}_m^R}{(k_m - k)B_m}. \tag{2.73}$$

The displacement in transformed wavenumber domain can be expressed as:

$$\tilde{\mathbf{Q}} = \sum_{m=1}^{2M} \frac{\mathbf{\Phi}_{m2}^L \tilde{\mathbf{F}} \mathbf{\Phi}_{m1}^R}{(k_m - k)B_m} \tag{2.74}$$

where

$$\mathbf{\Phi}_m^L = \{ \mathbf{\Phi}_{m1}^L \quad \mathbf{\Phi}_{m2}^L \} \quad \mathbf{\Phi}_m^R = \begin{Bmatrix} \mathbf{\Phi}_{m1}^R \\ \mathbf{\Phi}_{m2}^R \end{Bmatrix} \tag{2.75}$$

$\mathbf{\Phi}_{m1}^L, \mathbf{\Phi}_{m2}^L, \mathbf{\Phi}_{m1}^R$ and $\mathbf{\Phi}_{m2}^R$ have the same dimension M.

2.5.4 Green's functions

Expressing $\mathbf{F}$ due to a concentrated unit load acting at point $(0, z_0)$ in the form:

$$\mathbf{F} = \mathbf{F}_0 \delta(x) \tag{2.76}$$

where δ is the Dirac delta function defined operationally by:

$$\int_{-\infty}^{\infty} f(x)\delta(x) = f(0) \tag{2.77}$$

and $\mathbf{F}_0$ is a constant vector representing the amplitude of the external force across the thickness of the plate given by

$$\mathbf{F}_0^{\mathrm{T}} = \langle 0 \quad \cdots, \quad 0, \quad 1, \quad 0 \quad \cdots \quad 0 \rangle \tag{2.78}$$

The Fourier transform of $\mathbf{F}$ is:

$$\tilde{\mathbf{F}} = \int_{-\infty}^{\infty} \mathbf{F}_0 \delta(x) e^{-jkx} dx = \mathbf{F}_0. \tag{2.79}$$

Substituting the above equation into (2.74) gives

$$\tilde{\mathbf{Q}} = \sum_{m=1}^{2M} \frac{\psi \mathbf{\Phi}_{m1}^R}{(k_m - k) B_m} \tag{2.80}$$

where $\psi = \mathbf{\Phi}_{m2}^L \mathbf{F}_0$.

Application of the inverse Fourier transform to equation (2.80) gives the displacement in frequency domain as

$$\mathbf{Q}(x) = \frac{1}{2\pi} \int_{-\infty}^{\infty} \sum_{m=1}^{2M} \frac{\psi \mathbf{\Phi}_{m1}^R}{(k_m - k) B_m} e^{jkx} dk \tag{2.81}$$

It is noted that in the above equation, ψ, $\mathbf{\Phi}_{m1}^R$ and B_m are independent of k. Applying Cauchy's residue theorem [59], choosing the M modes that propagate away from the source, we obtain the displacement Green's function due to the unit point load as:

$$\mathbf{Q}(x) = \sum_{m=1}^{M} A_m \mathbf{q}_m e^{jk_m x} \tag{2.82}$$

where

$$A_m = -\frac{j\psi}{B_m}; \quad \mathbf{q}_m = \mathbf{\Phi}_{m1}^R \tag{2.83}$$

2.6 Numerical implementation

Three numerical examples are considered for illustration purposes. For brevity, only results for a vertical load are presented in the following examples.

Table 2.1: Elastic properties of 0° and 90° Graphite/Epoxy fibers (GPa)

degrees	D_{11}	D_{33}	D_{13}	D_{55}
0°	160.73	13.92	6.44	7.07
90°	13.92	13.92	6.92	3.50

Example 1 . – a homogeneous isotropic plate with Poisson's ratio $\nu = 1/3$.

Example 2 . – a single layer graphite/epoxy cross-ply laminated plate with fibers being aligned with the x axis. The relevant elastic constants characterizing the plate material are: $D_{11} = 160.73\ GPa$, $D_{33} = 13.92\ GPa$, $D_{13} = 6.44\ GPa$, and $D_{55} = 7.07\ GPa$. The density is $1.8\ g/cm^3$. Thus, the longitudinal (c_p) and shear (c_s) wave speeds in the $x-$direction are 9.45 $mm/\mu s$ and 1.98 $mm/\mu s$, respectively.

Example 3 . – a 35-layer graphite/epoxy cross-ply laminated plate having 90°/0°/... /90°/ 0°/90°/... /0°/90° configuration. Material properties are given in Table 2.1. The 0° fibers are taken to be aligned with the x axis.

The frequency nondimensionlization $\Omega = \omega H/c_s$ is used for example 1, and $\Omega = \omega H/\sqrt{(D_{55}/\rho)_{0°}}$ is used for examples 2 and 3.

In the first two examples, the concentrated load is supposed to be acting at $(0, H/4)$, while in the third example, it is supposed to be at $(0, 16H/35)$.

Example 1

To illustrate the application of techniques presented above, we first consider the Green's functions for an isotropic plate. The solution is compared with the results obtained by wavenumber integral technique developed by Xu and Mal [44]. To apply

the wavenumber integral technique some material dissipation must be assumed. The elastic constants (λ and μ) and the longitudinal and shear wavenumbers k_p and k_s, respectively, were taken to be frequency-dependent and complex:

$$k_p = (1 + 0.5j/Q_{\rm L})\omega/c_p; \qquad k_{\rm s} = (1 + 0.5j/Q_{\rm T})\omega/c_s,$$

$$\mu = \rho c_s^2/(1 + 0.5j/Q_{\rm T})^2; \qquad \lambda + 2\mu = \rho c_p^2/(1 + 0.5j/Q_{\rm L})^2$$

Here $Q_{\rm L}$ and $Q_{\rm T}$ are the quality factors which account for dissipation. Numerical computations show that at low frequencies, by choosing the typical values of these quality factors as used by Xu and Mal in the wavenumber integrals, results are in very good agreement with those of our techniques in both near and far regions. For example, at $\Omega = 1$, choosing $Q_{\rm L} = 200$, and $Q_{\rm T} = 100$, good agreement is obtained. Figure 2.3 shows the vertical displacement along the top surface of the plate. In this figure, RRS represents the Rayleigh-Ritz approximation based stiffness method, and WNI represents wavenumber integral method.

As the frequency increases, however, their values must be adjusted in the wavenumber integrals in order to obtain good results.

Figure 2.4 shows the vertical displacements at the top surface obtained by the two methods when $\Omega = 20$. The dashed line in Figure 2.4(a) shows the results from the wavenumber integral method (WNI) with $Q_{\rm L} = 200$ and $Q_{\rm T} = 100$, while the solid line shows the results from the RRS. It is found that the two results agree only in the near field. Figure 2.4(b) shows the results when $Q_{\rm L} = 2000$ and $Q_{\rm T} = 1000$. Good agreement is found in both near and far regions only after adjusting the quality factors. It may be noted that the choice of appropriate quality factors for laminated plates can pose considerable problems.

Figures 2.5 and 2.6 show the displacement Green's function through the thickness of the plate near and far from the source obtained by RRS, WNI and WFE (representing wave function expansion technique) for $\Omega = 1$ and $\Omega = 20$, respectively. For

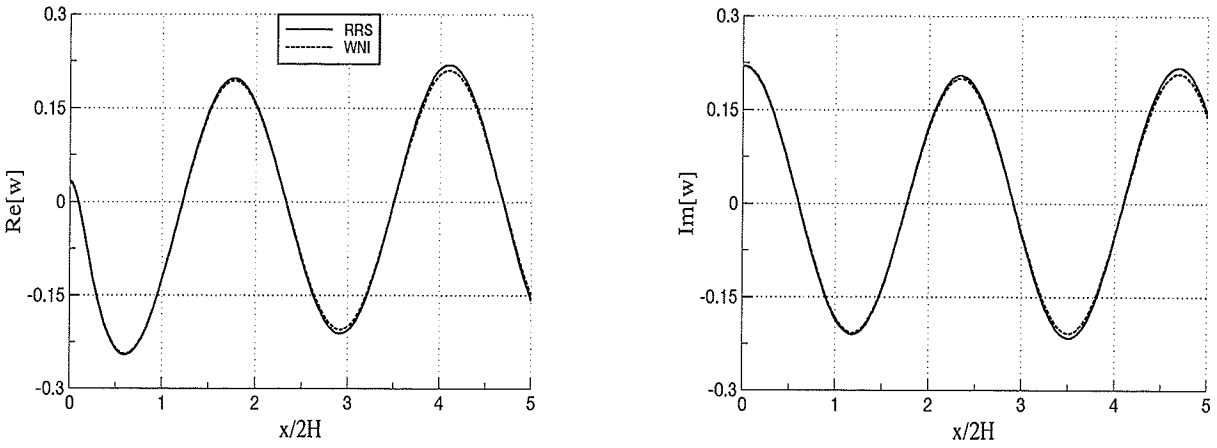

Figure 2.3: Vertical displacements along top surface, $\Omega = 1$

$\Omega = 1$, the plate is divided into ten sublayers in the RRS method. Thirty modes, which contain one symmetric and one antisymmetric propagating modes, are used in the wave function expansion method. For $\Omega = 20$, Q_{L} and Q_{T} were chosen to be 2000 and 1000, respectively. The plate is divided into twenty sublayers in the RRS method. Forty modes, which contain ten symmetric and ten antisymmetric propagating modes, are used in the wave function expansion. In this example $|\epsilon|$ was less than 0.5%.

Example 2

The dispersion relation of the single layered plate is shown in Figure 2.7. In this example we consider the Green's functions for two normalized frequencies, $\Omega = 1$ and 10. Both the wave function expansion technique and Rayleigh-Ritz approximation based stiffness method are employed. Figure 2.8 gives the displacements along the

sections $x = 0.3H$ and $x = 10H$ at $\Omega = 1$ and $\Omega = 10$. It is seen that the results from the two methods are in good agreements in both near and far fields, at low and high frequencies.

Example 3

Figure 2.9 shows the dispersion relation of the 35-layered cross-ply plate. Two normalized frequencies, $\Omega = 1$ and 10, are considered. There is one symmetric and one antisymmetric propagating mode at $\Omega = 1$ and six symmetric and seven antisymmetric propagating modes at $\Omega = 10$.

For each frequency total number of forty modes are used in the wave function expansion technique. Figures 2.10(a) and (b) show displacements at sections $x = 0.3H$ and $x = 10H$ when $\Omega = 1$, and Figures 2.11(a) and (b) show the corresponding results when $\Omega = 10$. The percentage error $|\epsilon|$ is less than 1% in the cases considered from wave function expansion technique. These figures show that at low frequencies the motion is primarily vertical except near the free surfaces of the plate. Figure 2.10 shows that $Im[w]$ is constant through the thickness at locations both near and far from the source. $Re[w]$ on the other hand varies through the thickness in the near field and is uniform in the far field. At high frequency, the dominant component is still vertical, but now there is also a measurable horizontal component. It is interesting to note the oscillations in the horizontal component in Figure 2.11 are caused by the lamination. They seem to be caused by the large differences in the shear modulus D_{55} of the adjacent layers (D_{55} of the 0° lamina is twice that of the 90° lamina).

2.7 Concluding remarks

An analytical formulation is employed to study the guided wave propagation in laminated composite plates. The delta matrix formulation is developed to refine the modes. A stiffness method based on the through-thickness interpolation functions for displacements has also been presented.

The Green's functions for laminated plates are constructed based on the two models of wave propagation analysis. It is shown that the solution for the isotropic plate agreed well with the wavenumber integral results. In the latter case it was necessary to choose frequency-dependent attenuation in order to get good results. Results are presented also for uniaxial and multilayered composite plates.

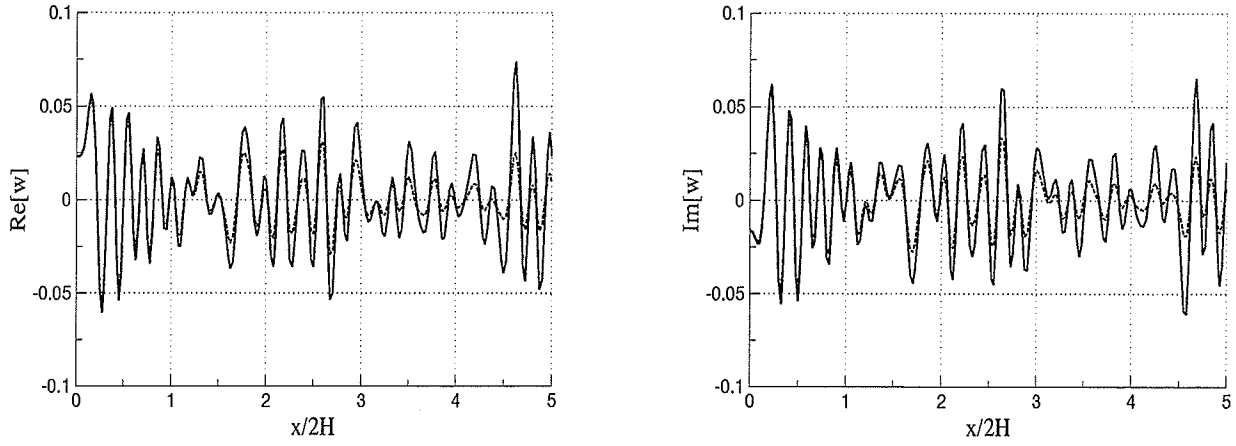

(a)

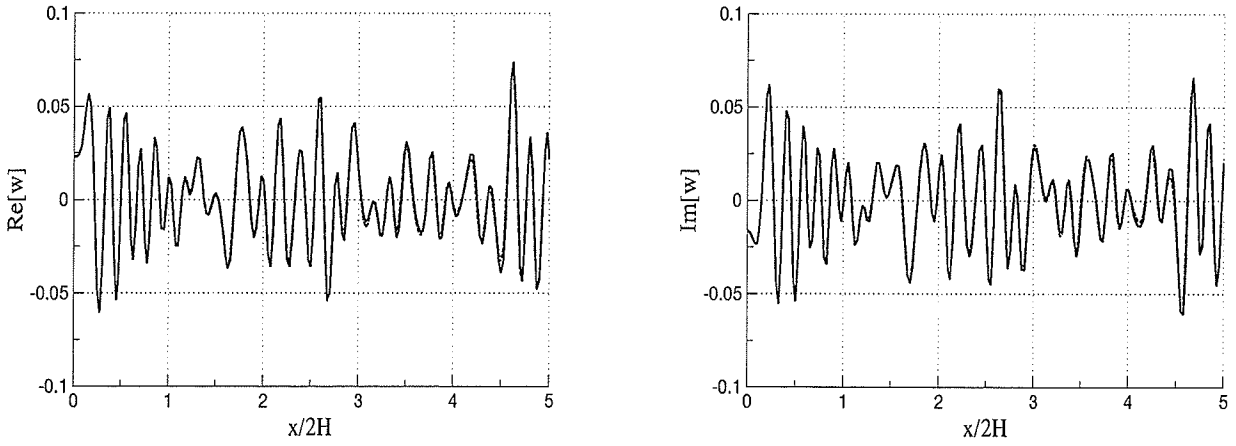

(b)

Figure 2.4: Vertical displacements along top surface, $\Omega = 20$. (a) $Q_{\mathrm{L}} = 200$, $Q_{\mathrm{T}} = 100$; (b) $Q_{\mathrm{L}} = 2000$, $Q_{\mathrm{T}} = 1000$.

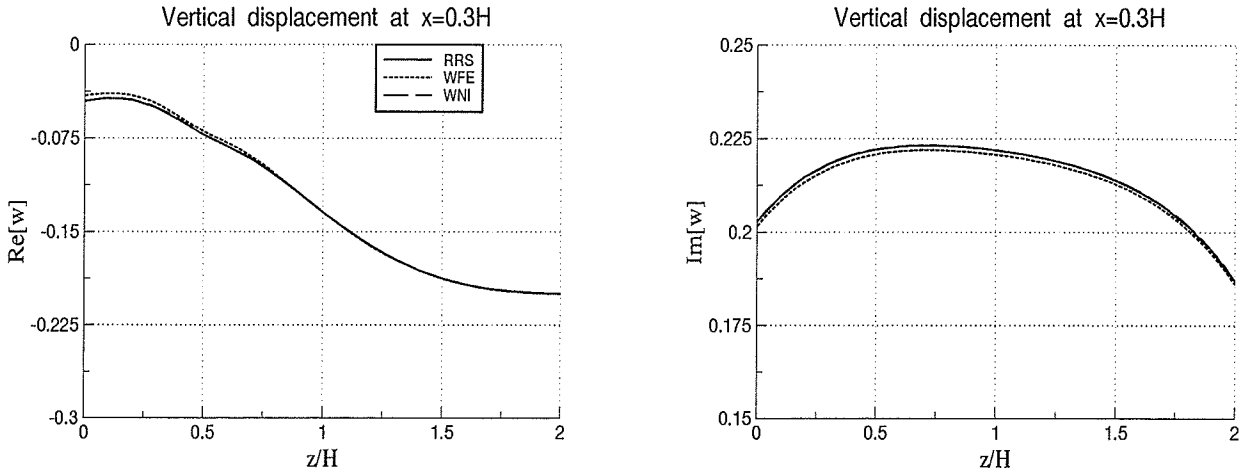

(a)

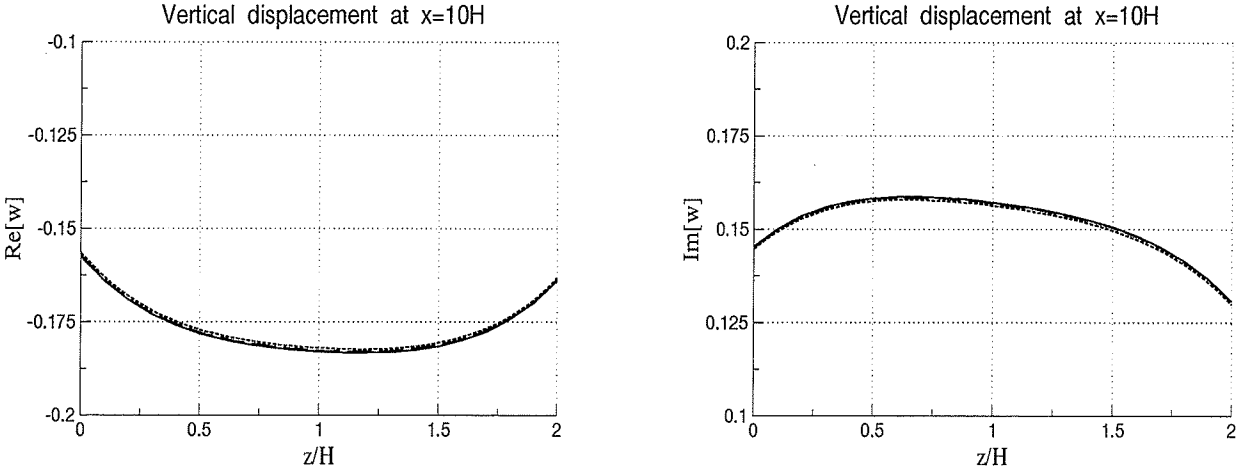

(b)

Figure 2.5: Vertical displacements along sections, $\Omega = 1$. (a) $x = 0.3H$; (b) $x = 10H$.

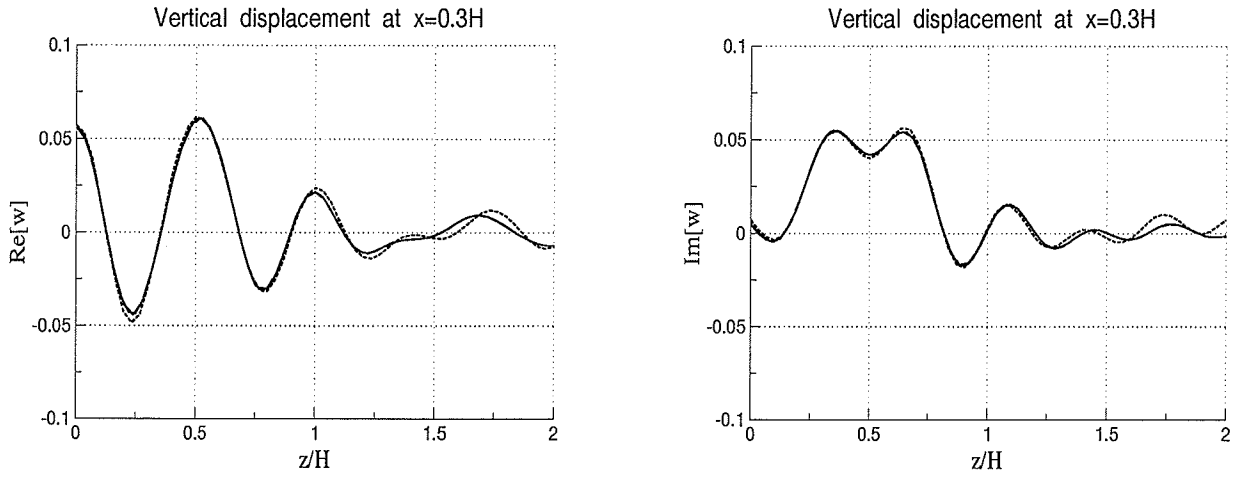

(a)

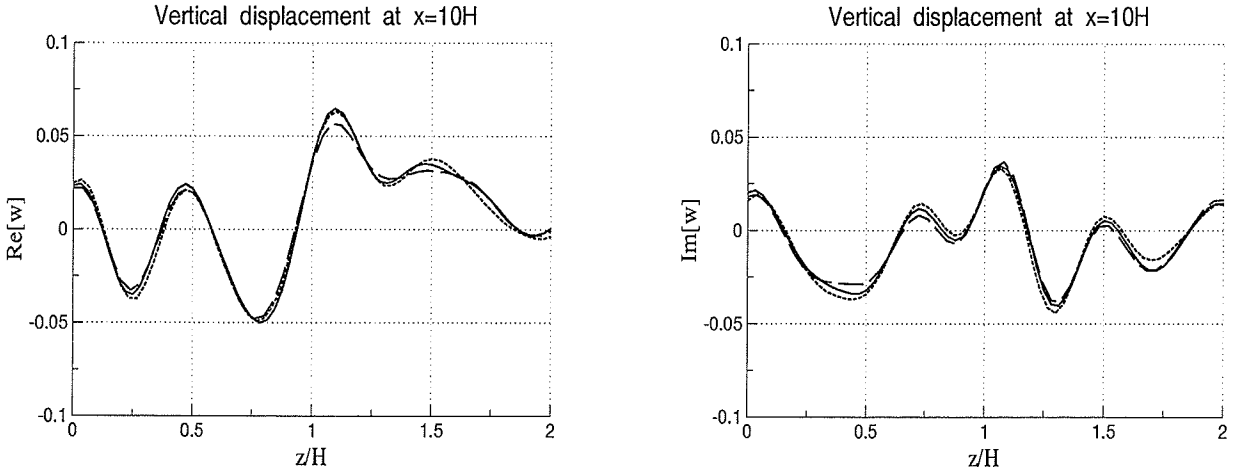

(b)

Figure 2.6: Vertical displacements along sections, $\Omega = 20$. (a) $x = 0.3H$; (b) $x = 10H$.

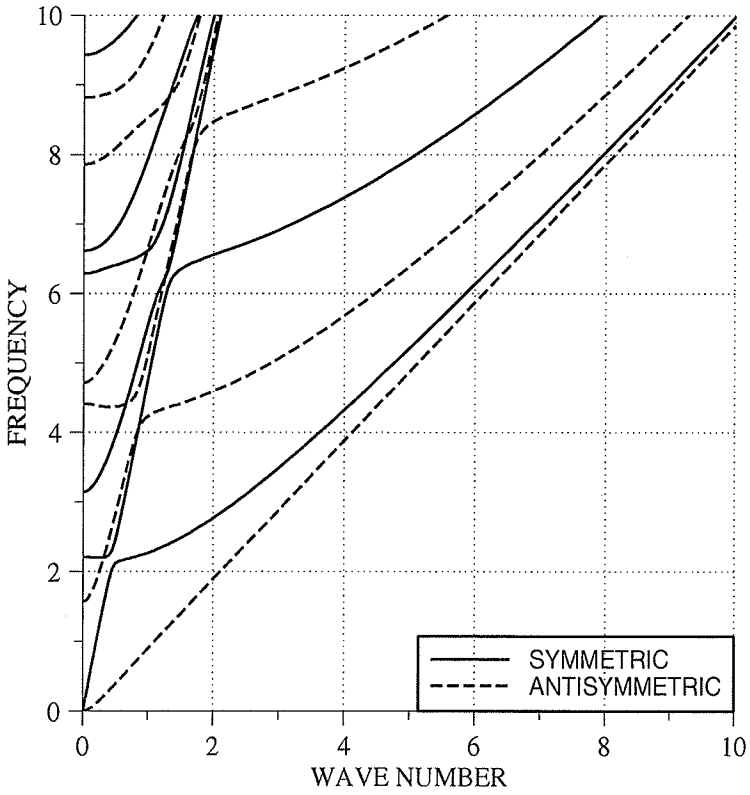

Figure 2.7: The dispersion relation of the single layered plate

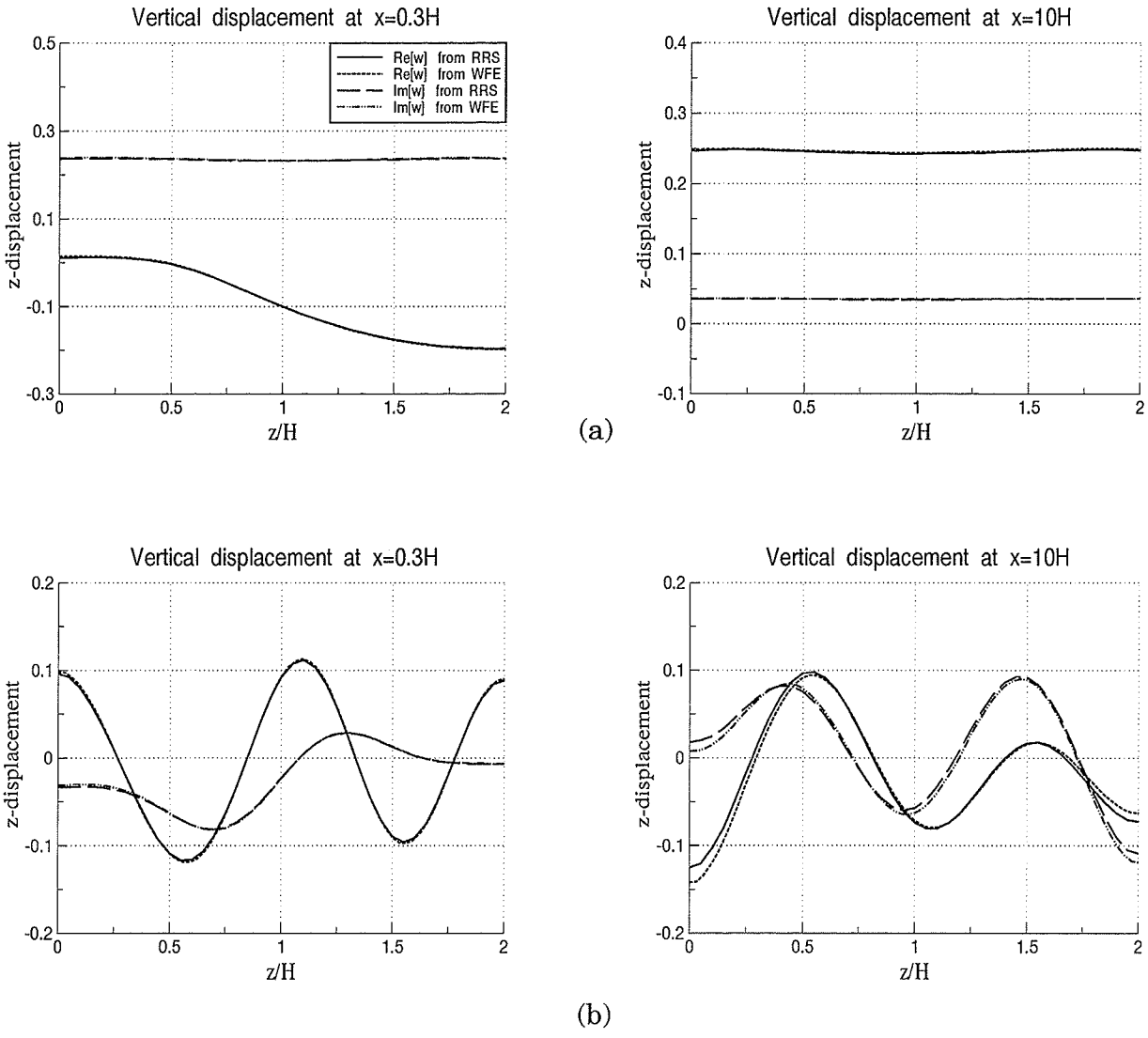

Figure 2.8: Vertical displacements along sections in the single layered plate. (a) $\Omega = 1$, (b) $\Omega = 10$.

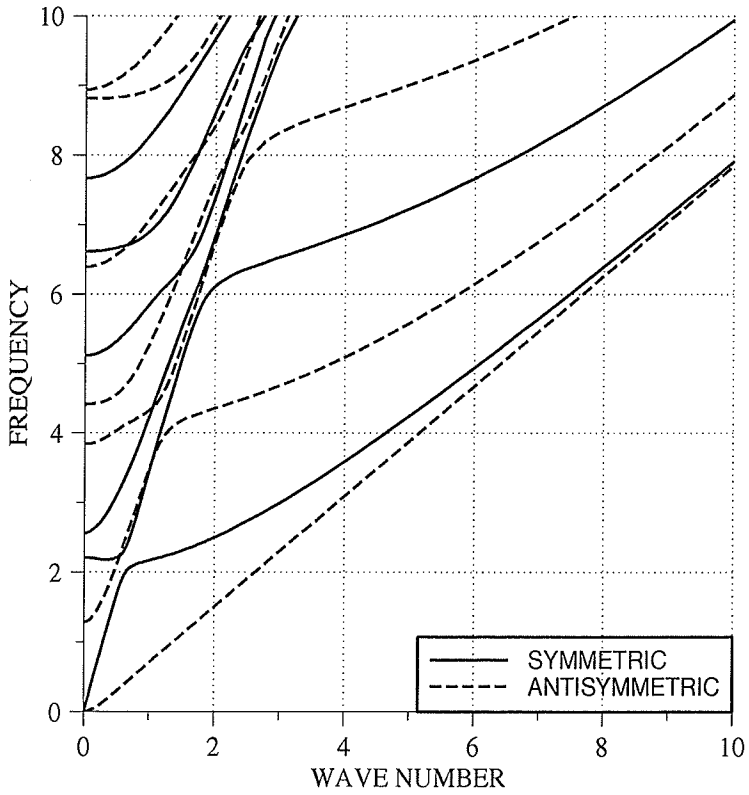

Figure 2.9: The dispersion relation of the 35-layered plate

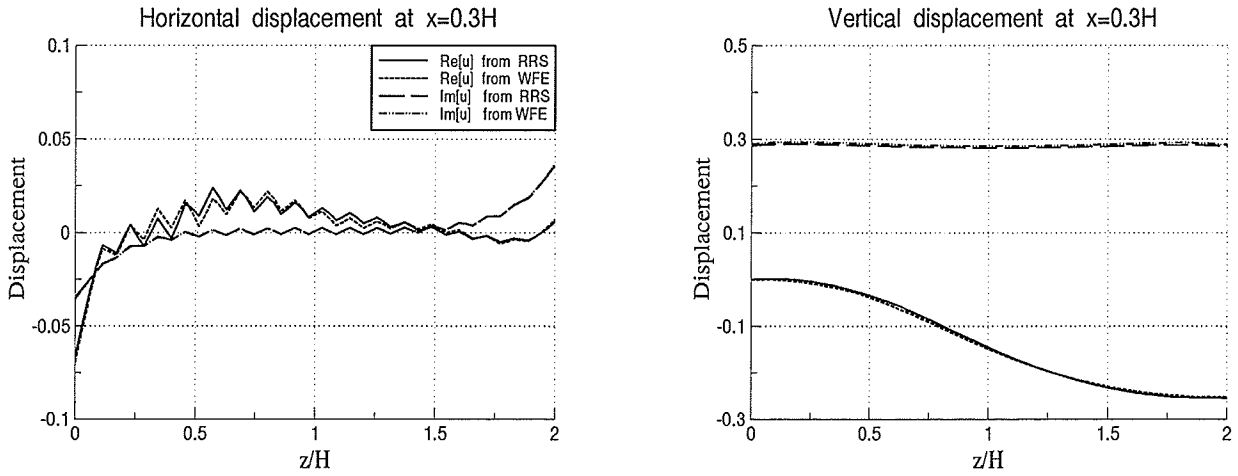

(a)

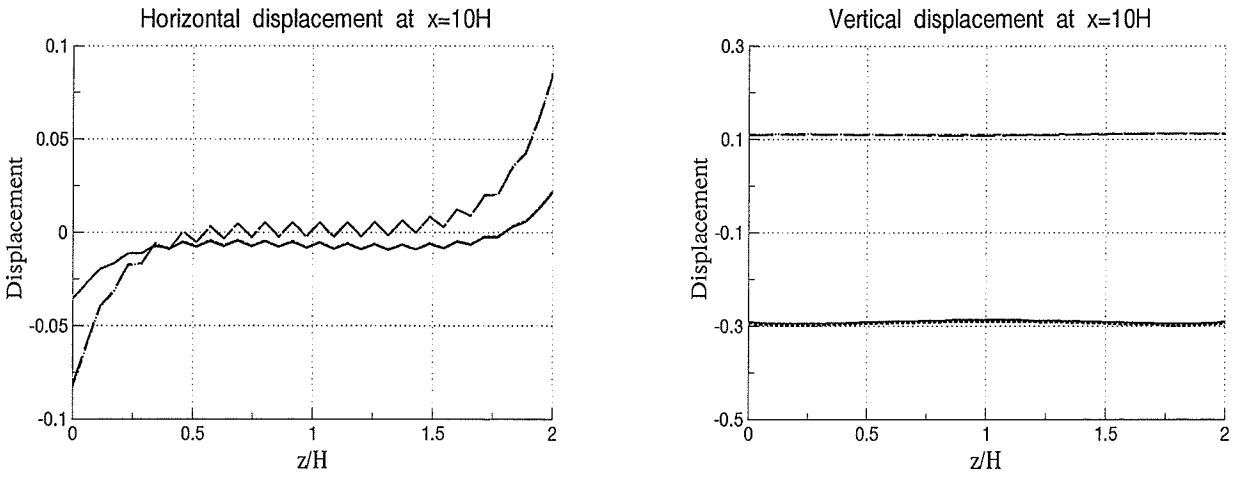

(b)

Figure 2.10: Displacements along sections for 35-layered plate, $\Omega = 1$. (a) $x = 0.3H$; (b) $x = 10H$.

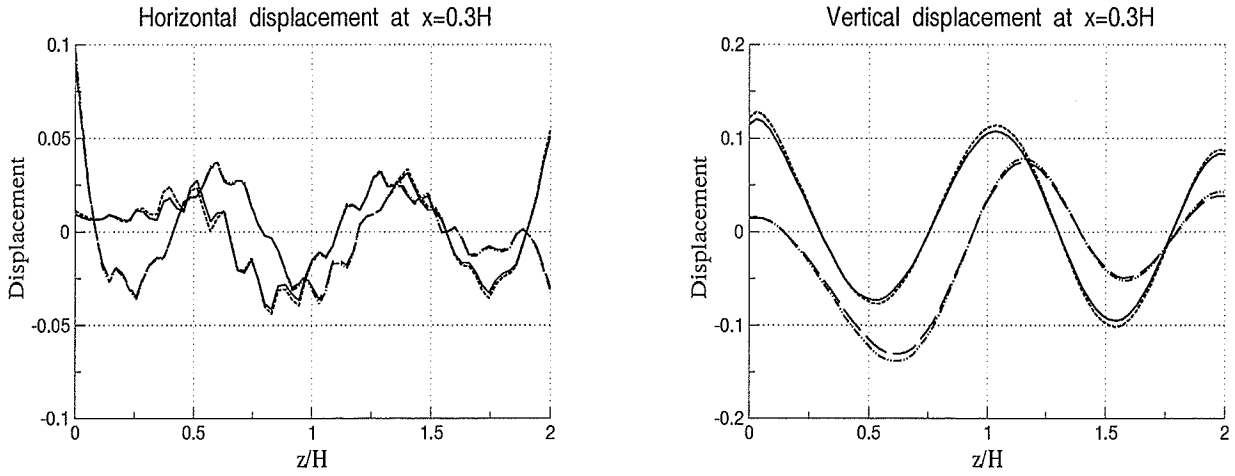

(a)

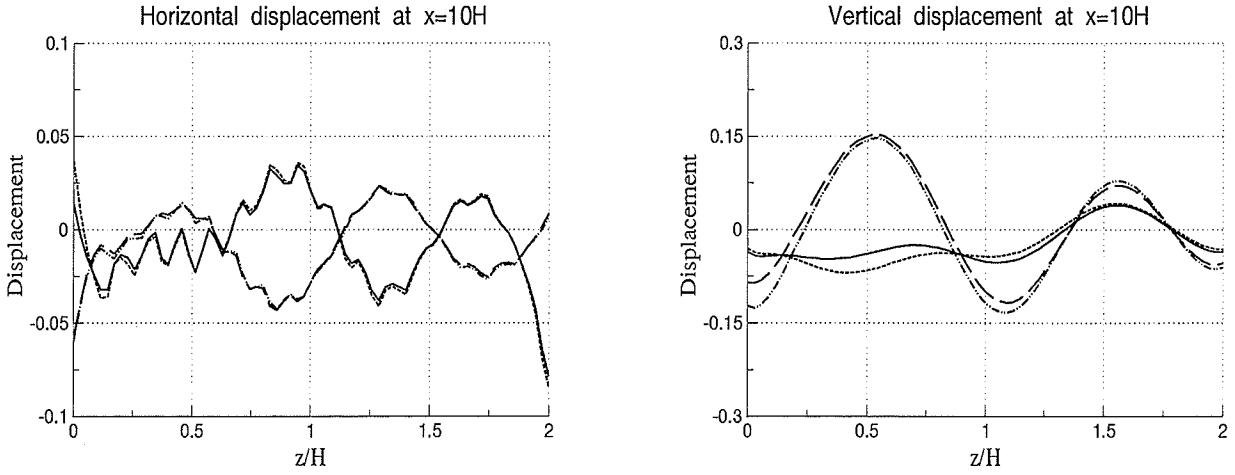

(b)

Figure 2.11: Displacements along sections for 35-layered plate, $\Omega = 10$. (a) $x = 0.3H$; (b) $x = 10H$.

Chapter 3

Plane-strain Wave Scattering

3.1 General

The need for ultrasonic nondestructive evaluation (NDE) techniques has motivated much progress in the understanding of elastic wave scattering by defects in composite structures, which are often in the form of plates. It is extremely difficult, if not impossible, to obtain a general analytical solution for the complex wave interaction phenomenon occurring in a plate-flaw system. Therefore, it is necessary to resort to numerical methods. The study of wave scattering problem can be categorized into:

1. the study of elastic wave propagation in undamaged media (incident field), which is typically represented by the study of elastodynamic Green's functions, as presented in Chapter 2;

2. the study of wave scattering due to flaws in the media, which is the subject of this Chapter.

Two models are developed in this Chapter to study the wave scattering problems: hybrid model and boundary element model. The hybrid method combines finite

element formulation in a bounded interior region of the plate with a wave function expansion representation in the exterior region. The flaw is assumed to be contained in the bounded interior region. The two regions are connected along vertical boundaries. Continuity conditions for the displacements and interaction forces are imposed at the finite element nodes lying on the boundaries.

A generalized boundary element method is established to analyze the wave scattering problem by cracks. The time-harmonic Green's functions for composite plates obtained in Chapter 2 are employed. A new technique is developed to evaluate the Cauchy Principal Value (CPV) and weakly singular integrals involved in the boundary integral equations. This technique is also extended to treat the singular integrals around corner points. To circumvent the difficulties arising from the presence of cracks, a multidomain technique is incorporated. Numerical investigation shows that the boundary element method is much more efficient than the hybrid method when large cracks are involved.

3.2 Description of the problem

Time harmonic wave scattering by flaws (crack, delamination or inclusion) in an infinite laminated composite plate is considered. It is assumed that the geometry of flaws and the incident load are independent of y coordinate. So, as shown in Figure 3.1, a plane-strain wave motion in xz plane is generated. The methodology and formula established in Chapter 2 to compute Green's functions will be employed here. The objective herein is to investigate the scattered field due to the existence of flaws.

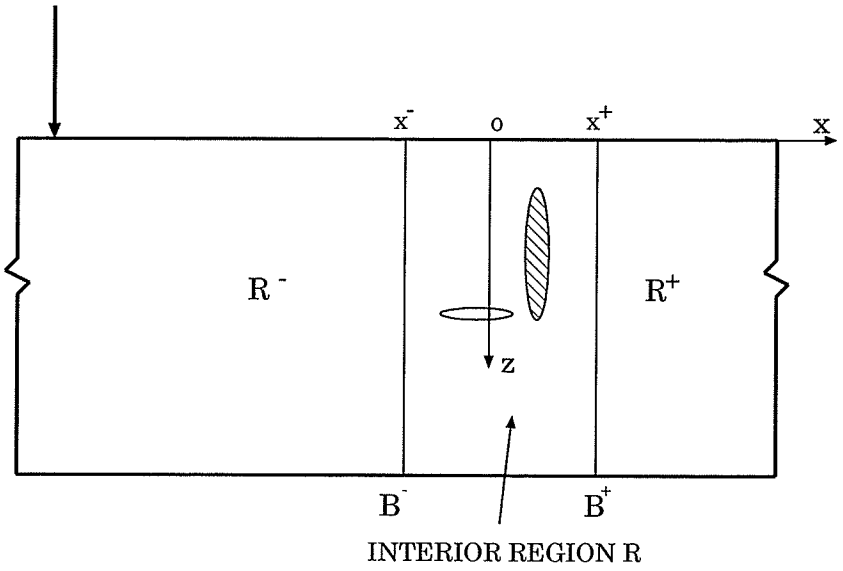

Figure 3.1: Region division of a plate

3.3 Hybrid method

The hybrid method combines finite element formulation in a bounded interior region of the plate with a wave function expansion representation in the exterior region. The hybrid method was called by Dong and his co-researchers as Global-Local Finite Element Method (GLFEM) [60, 61, 62]. The interior region consists of the flaw and a small region of the plate surrounding the flaw. The regions are connected along vertical boundaries B^+ at $x = x^+$, and B^- at $x = x^-$ as shown in Figure 3.1.

3.3.1 Wave function expansion for exterior regions

In the exterior regions R^+ and R^-, the total wave field consists of a scattered field and the incident field. Using the wave function representation (Chapter 2) , the displacement vector of the scattered field, $\{\mathbf{q}_x^{s+}\}$, in region R^+ at arbitrary x can be

written as

$$\mathbf{q}_x^{\mathrm{s}} = \sum_{m=1}^{M} A_m^+ \mathbf{q}_m \exp(jk_m x), \qquad x \geq x^+ \tag{3.1}$$

where A_m^+ is the amplitude of the m-th scattered mode in region R^+; $\mathbf{q}_m$ is the displacement shape mode which is arranged according to the order of interface, rather than the degree of freedom as:

$$\mathbf{q}_m^{\mathrm{T}} = \langle\, u_{1m}, \quad w_{1m}, \quad \ldots, \quad u_{im}, \quad w_{im}, \quad , \ldots, \quad u_{(N+1)m}, \quad w_{(N+1)m} \quad \rangle\,. \tag{3.2}$$

Equation (3.1) gives the displacement vector of scattered wave field at the nodes on the boundary B^+ as

$$\mathbf{q}_{\mathrm{B}^+}^{\mathrm{s}} = \mathbf{G}^+ \boldsymbol{\Lambda}^+ \tag{3.3}$$

where

$$\mathbf{G}^+ = [\,\mathbf{q}_1 \quad \mathbf{q}_2 \quad \cdots\cdots \quad \mathbf{q}_m \cdots\cdots \quad \mathbf{q}_M\,] \tag{3.4}$$

$$\boldsymbol{\Lambda}^{+\mathrm{T}} = \langle\, \Lambda_1^+ \quad \Lambda_2^+ \quad \cdots \quad \Lambda_m^+ \quad \cdots \quad \Lambda_M^+ \,\rangle \tag{3.5}$$

$$\Lambda_m^+ = A_m^+ \exp(jk_m x^+), \qquad m = 1, 2, \cdots, M. \tag{3.6}$$

The nodal force vector at the boundary B^+ due to scattered field can be formed as

$$\mathbf{P}_{\mathrm{B}^+}^{\mathrm{s}} = \mathbf{F}^+ \boldsymbol{\Lambda}^+, \tag{3.7}$$

where

$$\mathbf{F}^+ = [\,\mathbf{f}_1 \quad \mathbf{f}_2 \quad \cdots\cdots \quad \mathbf{f}_m \cdots\cdots \quad \mathbf{f}_M\,] \tag{3.8}$$

Following a similar procedure the displacement and force vectors at the boundary B^- due to scattered field can be expressed as

$$\mathbf{q}_{\mathrm{B}^-}^{\mathrm{s}} = \mathbf{G}^- \boldsymbol{\Lambda}^-; \qquad \mathbf{P}_{\mathrm{B}^-}^{\mathrm{s}} = \mathbf{F}^- \boldsymbol{\Lambda}^-. \tag{3.9}$$

It can be shown that $\mathbf{G}^-$ ($\mathbf{F}^-$) can simply be obtained from $\mathbf{G}^+$ ($\mathbf{F}^+$) after replacing each x direction displacement (force) component by the negative value of it; and

$$\mathbf{\Lambda}^{-\mathrm{T}} = \langle\, \Lambda_1^- \quad \Lambda_2^- \quad \cdots \quad \Lambda_m^- \quad \cdots \quad \Lambda_M^- \,\rangle \tag{3.10}$$

where

$$\Lambda_m^- = A_m^- \exp(jk_m|x^-|)$$

in which, A_m^- is the amplitude of m-th scattered mode in region R^-.

3.3.2 Finite element model of interior region

The interior region R is modelled by finite elements. The displacement vector, $\mathbf{u}$, at a point within a typical finite element, e, is interpolated from the nodal displacement vector, $\mathbf{q}^e$, as

$$\mathbf{u} = \mathbf{N}\mathbf{q}^e \tag{3.11}$$

where $\mathbf{N}$ is shape function matrix [63].

The energy functional $\hat{\pi}$ (per unit length in y direction) takes the form

$$\hat{\pi} = \sum_e [\frac{1}{2}\int_{A^e} (\{\bar{\epsilon}\}^{\mathrm{T}}\mathbf{D}\{\epsilon\} - \rho\omega^2\bar{\mathbf{u}}^{\mathrm{T}}\mathbf{u})dA] - \frac{1}{2}[\bar{\mathbf{q}}_T^{\mathrm{T}}\mathbf{P}_T + \bar{\mathbf{q}}_T^{\mathrm{T}}\bar{\mathbf{P}}_T] \tag{3.12}$$

where $\mathbf{D}$ is the constitutive matrix, and

$$\mathbf{q}_T^{\mathrm{T}} = \langle\, \mathbf{q}_{\mathrm{I}}{}^{\mathrm{T}} \quad \mathbf{q}_{\mathrm{B}}{}^{\mathrm{T}} \,\rangle, \quad \mathbf{P}_T^{\mathrm{T}} = \langle\, \mathbf{P}_{\mathrm{I}}{}^{\mathrm{T}} \quad \mathbf{P}_{\mathrm{B}}{}^{\mathrm{T}} \,\rangle \tag{3.13}$$

$\mathbf{q}_{\mathrm{B}}$ and $\mathbf{P}_{\mathrm{B}}$ are, respectively, the nodal displacement and interaction force vectors corresponding to the nodes lying on the boundaries (B^+ and B^-), while $\mathbf{q}_{\mathrm{I}}$ and $\mathbf{P}_{\mathrm{I}}$ represent those vectors corresponding to the nodes within the interior region; the integral is over the area of element e and $\sum_e$ implies summation over all the finite elements; and overbar denotes complex conjugate.

After the conventional assembly process in the finite element method, equation (3.12) can be written as

$$\hat{\pi} = \frac{1}{2}\bar{\mathbf{q}}_{\mathrm{T}}^{\mathrm{T}}\mathbf{S}\mathbf{q}_{\mathrm{T}} - \frac{1}{2}[\bar{\mathbf{q}}_{\mathrm{T}}^{\mathrm{T}}\mathbf{P}_{\mathrm{T}} + \mathbf{q}_{\mathrm{T}}{}^{\mathrm{T}}\bar{\mathbf{P}}_{\mathrm{T}}] \tag{3.14}$$

where

$$\mathbf{S} = \mathbf{K}_{\mathrm{T}} - \omega^2\mathbf{M}_{\mathrm{T}} = \begin{bmatrix} \mathbf{S}_{\mathrm{II}} & \mathbf{S}_{\mathrm{IB}} \\ \mathbf{S}_{\mathrm{BI}} & \mathbf{S}_{\mathrm{BB}} \end{bmatrix}. \tag{3.15}$$

In the above, $\mathbf{K}_{\mathrm{T}}$ and $\mathbf{M}_{\mathrm{T}}$ are, respectively, the global stiffness and mass matrices of the interior region.

The governing equation of the entire interior region can be obtained by minimizing the energy functional as:

$$\delta\hat{\pi} = \delta\bar{\mathbf{q}}_{\mathrm{T}}^{\mathrm{T}}\mathbf{S}\mathbf{q}_{\mathrm{T}} - \delta\bar{\mathbf{q}}_{\mathrm{T}}^{\mathrm{T}}\mathbf{P}_{\mathrm{T}} = 0 \tag{3.16}$$

where δ implies first variation.

3.3.3 Global solution

The global solution is obtained by imposing the following continuity conditions on displacements and tractions at the mesh boundaries:

$$\begin{aligned} \mathbf{q}_{\mathrm{B}} &= \mathbf{q}_{\mathrm{B}}^{\mathrm{in}} + \mathbf{q}_{\mathrm{B}}^{\mathrm{s}}, \\ \mathbf{P}_{\mathrm{B}} &= \mathbf{P}_{\mathrm{B}}^{\mathrm{in}} + \mathbf{P}_{\mathrm{B}}^{\mathrm{s}} \end{aligned} \tag{3.17}$$

where

$$\mathbf{q}_{\mathrm{B}}^{in\,\mathrm{T}} = \langle\, \mathbf{q}_{\mathrm{B}+}^{\mathrm{in}\,\mathrm{T}} \quad \mathbf{q}_{\mathrm{B}-}^{\mathrm{in}\,\mathrm{T}} \,\rangle; \quad \mathbf{P}_{\mathrm{B}}^{\mathrm{in}\,\mathrm{T}} = \langle\, \mathbf{P}_{\mathrm{B}+}^{\mathrm{in}\,\mathrm{T}} \quad \mathbf{P}_{\mathrm{B}-}^{\mathrm{in}\,\mathrm{T}} \,\rangle \tag{3.18}$$

$$\mathbf{q}_{\mathrm{B}}^{s\,\mathrm{T}} = \langle\, \mathbf{q}_{\mathrm{B}+}^{s\,\mathrm{T}} \quad \mathbf{q}_{\mathrm{B}-}^{s\,\mathrm{T}} \,\rangle; \quad \mathbf{P}_{\mathrm{B}}^{s\,\mathrm{T}} = \langle\, \mathbf{P}_{\mathrm{B}+}^{s\,\mathrm{T}} \quad \mathbf{P}_{\mathrm{B}-}^{s\,\mathrm{T}} \,\rangle \tag{3.19}$$

and superscript *in* indicates incident field. In equation (3.17), those quantities on the left hand side of the equal sign are from the interior region while those on the right hand side are from the exterior region.

Substituting equations (3.13) and (3.15) into (3.16), together with the incorporation of equation (3.17) results in

$$\begin{aligned} \delta\bar{\mathbf{q}}_{\mathrm{I}}^{\mathrm{T}} \quad & [\mathbf{S}_{\mathrm{II}}\mathbf{q}_{\mathrm{I}} + \mathbf{S}_{\mathrm{IB}}(\mathbf{q}_{\mathrm{B}}^{\mathrm{in}} + \mathbf{q}_{\mathrm{B}}^{\mathrm{s}}) - \mathbf{P}_{\mathrm{I}}] \\ + \quad & \delta\bar{\mathbf{q}}_{\mathrm{B}}^{\mathrm{T}}[\mathbf{S}_{\mathrm{BI}}\mathbf{q}_{\mathrm{I}} + \mathbf{S}_{\mathrm{BB}}(\mathbf{q}_{\mathrm{B}}^{\mathrm{in}} + \mathbf{q}_{\mathrm{B}}^{\mathrm{s}}) - \mathbf{P}_{\mathrm{B}}^{\mathrm{in}}] = 0. \end{aligned} \tag{3.20}$$

Above equation gives:

$$\mathbf{S}_{\mathrm{II}}\mathbf{q}_{\mathrm{I}} + \mathbf{S}_{\mathrm{IB}}(\mathbf{q}_{\mathrm{B}}^{\mathrm{in}} + \mathbf{q}_{\mathrm{B}}^{\mathrm{s}}) - \mathbf{P}_{\mathrm{I}} = 0 \tag{3.21}$$

$$\bar{\mathbf{G}}^{\mathrm{T}}[\mathbf{S}_{\mathrm{BI}}\mathbf{q}_{\mathrm{I}} + \mathbf{S}_{\mathrm{BB}}(\mathbf{q}_{\mathrm{B}}^{\mathrm{in}} + \mathbf{q}_{\mathrm{B}}^{\mathrm{s}}) - \mathbf{P}_{\mathrm{B}}^{\mathrm{in}}] = 0. \tag{3.22}$$

From equation (3.21) one obtains

$$\mathbf{q}_{\mathrm{I}} = \mathbf{S}_{\mathrm{II}}^{-1}\mathbf{P}_{I} - \mathbf{S}_{\mathrm{II}}^{-1}\mathbf{S}_{\mathrm{IB}}(\mathbf{q}_{\mathrm{B}}^{\mathrm{in}} + \mathbf{q}_{\mathrm{B}}^{\mathrm{s}}). \tag{3.23}$$

Substituting the above equation into (3.22) yields:

$$\bar{\mathbf{G}}^{\mathrm{T}}(\mathbf{S}_{\mathrm{BB}}^{*}\mathbf{G} - \mathbf{F})\mathbf{\Lambda} = \bar{\mathbf{G}}^{\mathrm{T}}(\mathbf{P}_{\mathrm{B}}^{\mathrm{in}} - \mathbf{S}_{\mathrm{BI}}\mathbf{S}_{\mathrm{II}}\mathbf{P}_{\mathbf{I}} - \mathbf{S}_{\mathrm{BB}}^{*}\mathbf{q}_{\mathrm{B}}^{\mathrm{in}}) \tag{3.24}$$

where

$$\mathbf{S}_{\mathrm{BB}}^{*} = \mathbf{S}_{\mathrm{BB}} - \mathbf{S}_{\mathrm{BI}}\mathbf{S}_{\mathrm{II}}^{-1}\mathbf{S}_{\mathrm{IB}}, \tag{3.25}$$

$$\mathbf{G} = \begin{bmatrix} \mathbf{G}^{-} & \mathbf{0} \\ \mathbf{0} & \mathbf{G}^{+} \end{bmatrix}; \quad \mathbf{F} = \begin{bmatrix} \mathbf{F}^{-} & \mathbf{0} \\ \mathbf{0} & \mathbf{F}^{+} \end{bmatrix}. \tag{3.26}$$

$$\mathbf{\Lambda}^{\mathrm{T}} = \langle\, \mathbf{\Lambda}^{-\mathrm{T}} \quad \mathbf{\Lambda}^{+\mathrm{T}} \,\rangle\,. \tag{3.27}$$

In the above, $\mathbf{P}_{\mathrm{B}}^{\mathrm{in}}$ and $\mathbf{q}_{\mathrm{B}}^{\mathrm{in}}$ can be computed from application of Green's functions. Now that $\mathbf{\Lambda}$ is known, the scattered field can be determined by equation (3.1).

3.4 Boundary element method

The boundary element method (BEM) also known as the boundary integral equation (BIE) method has been firmly established in many engineering disciplines as an alternative numerical technique to the finite element method. The attraction of BEM can be largely attributed to the reduction in the dimensionality of the problem; for two-dimensional problems, only the line-boundary of the domain needs to be discretized into elements and for three-dimensional problems only the surface of the domain needs to be discretized. This means that, compared to a FEM domain type analysis, a boundary analysis results in a substantial reduction in data preparation and a much smaller system of algebraic equations to be solved numerically. Furthermore, this simpler description of the body means that regions of high stress concentration (i.e. crack tip area) can be modelled more efficiently because the high concentration of grid points is confined to one less dimension.

Other advantages of BEM include the automatic satisfaction of boundary conditions for infinite and semi-infinite domains, thus avoiding the need for numerical discretization of remote boundaries. This useful feature of automatic satisfaction of boundary conditions can be extended to several other configurations with finite boundaries, such as plates, half-plane and half-space. This is achieved through the employment of appropriate fundamental solutions which satisfy the boundary conditions.

3.4.1 Formulation

Consider a linearly elastic body of volume V bounded by a regular surface S. The boundary integral equation in the Fourier transformed frequency domain can be derived by combining the fundamental point-force solution with Betti's reciprocal the-

orem [64] as

$$c_{ij}(\mathbf{x}')u_j(\mathbf{x}') = \int_s [G_{ij}(\mathbf{x},\mathbf{x}')t_j(\mathbf{x}) - H_{ij}(\mathbf{x},\mathbf{x}')u_j(\mathbf{x})]dS + \int_v G_{ij}(\mathbf{x},\mathbf{x}')b_j(\mathbf{x})dV, \quad (3.28)$$

where u_i and t_i are the displacement and traction vectors, respectively; b_i is body force vector. $G_{ij}(\mathbf{x},\mathbf{x}')$ is displacement Green's function and represents the displacements at a point $\mathbf{x}$ due to a unit harmonic point force applied at a point $\mathbf{x}'$. $H_{ij}(\mathbf{x},\mathbf{x}')$ is traction Green's function and represents the tractions at the point $\mathbf{x}$ due to the same load. The tensor c_{ij} in equation (3.28) is the discontinuity term and has the following characteristics

(i) $c_{ij} = \delta_{ij}$ for a point $\mathbf{x}'$ inside the body V,

(ii) $c_{ij} = 0.5\delta_{ij}$ for a point $\mathbf{x}'$ on a smooth surface S, and

(iii) $c_{ij} = 0$ for a point $\mathbf{x}'$ outside the body V and surface S,

with δ_{ij} being the Kronecker delta.

Equation (3.28) cannot, in general, be solved analytically and therefore resort must be made to numerical methods of solution. For the numerical implementation, the boundary is divided into N elements connected to boundary nodes as shown in Figure 3.2, so that equation (3.28) becomes

$$c_{ij}(\mathbf{x}')u_j(\mathbf{x}') = \sum_{n=1}^{N} \int_{S_n} [G_{ij}(\mathbf{x},\mathbf{x}')t_j(\mathbf{x}) - H_{ij}(\mathbf{x},\mathbf{x}')u_j(\mathbf{x})]dS_n + \int_v G_{ij}(\mathbf{x},\mathbf{x}')b_j(\mathbf{x})dV, \quad (3.29)$$

where $S = \sum_{n=1}^{N} S_n$.

On each element, the boundary parameter $\mathbf{x}$, the unknown displacement field $u_j(\mathbf{x})$ and the traction field $t_j(\mathbf{x})$ are approximated using interpolation function. A discretized boundary element formulation can be obtained as

$$c_{ij}(\mathbf{x}')u_j(\mathbf{x}') + \sum_{n=1}^{N}\sum_{\alpha=1}^{l} H_{ij}^{n}(\mathbf{x},\mathbf{x}')u_j^{\alpha}(\mathbf{x}) = \sum_{n=1}^{N}\sum_{\alpha=1}^{l} G_{ij}^{n}(\mathbf{x},\mathbf{x}')t_j^{\alpha}(\mathbf{x}) + b_i^e \quad (3.30)$$

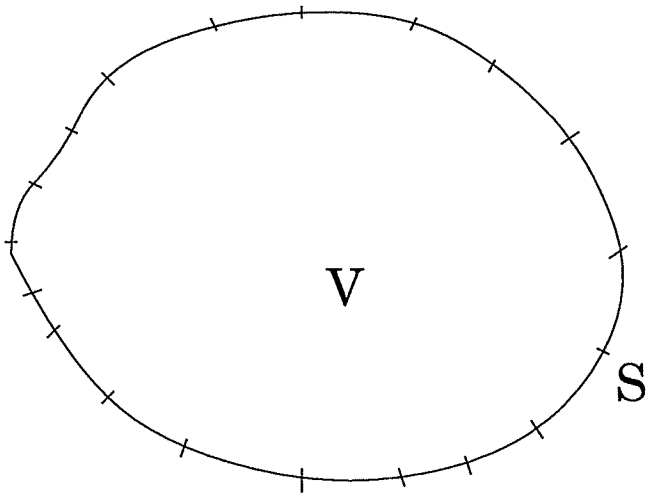

Figure 3.2: Discretization of boundary into elements

where l is the number of nodes of a boundary element. u^α and t^α are the values of the functions at node α. The coefficients H_{ij}^n and G_{ij}^n are defined in terms of integrals over S_n; and b_i^e represent the effect of body force.

Collecting equation at each of the boundary nodes gives a system of algebraic equations in a matrix form as

$$\mathbf{Hu} = \mathbf{Gt} + \mathbf{b} \tag{3.31}$$

where, matrix $\mathbf{H}$ contains the c_{ij} tensor and the traction kernel integrals, matrix $\mathbf{G}$ contains the displacement kernel integrals, and $\mathbf{u}$ and $\mathbf{t}$ are composed of the displacements and tractions at the nodes, respectively; and $\mathbf{b}$ is due to the body force.

Among the different applications of equation (3.29), problems concerning elastic waves scattering by cavities or cracks in plates are of interest.

If the fundamental solutions are defined for the plate, for example, the Green's functions from Chapter 2, the traction free conditions on the top and bottom surfaces of the plate are automatically satisfied. This important feature renders the discretization of these surfaces unnecessary. The displacements of the points on these surfaces,

which are important to the nondestructive evaluation technique, can be computed in the same manner as those of internal points.

3.4.2 Evaluation of CPV and weakly singular integrals

The diagonal 2×2 block of the assembled $\mathbf{H}$ matrix contains the tensor c_{ij} as well as the CPV of the traction kernel integrals; also, the diagonal 2×2 block of the assembled $\mathbf{G}$ matrix contains the weakly singular displacement kernel integrals. An effective technique to handle these singular integrals is critical to the accuracy of the boundary element solution. Most of the existing methods to treat these singular integrals are based on the properties of full space Green's functions.

A technique is developed here to evaluate the CPV and weakly singular integrals simultaneously. Although only two-dimensional formulation is taken for illustration purpose, the principle and the procedure established are valid for general case.

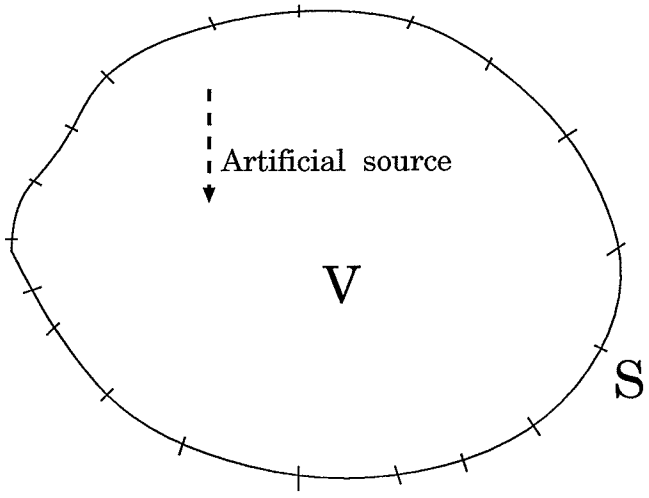

Figure 3.3: Artificial source

Figure 3.3 represents the geometry and boundary element mesh of the problem being solved. The technique starts with the concept of artificial source. Without loss of

generality this artificial source can be assumed to be a concentrated load, as shown in Figure 3.3. From the methods presented in Chapter 2 (or any other fundamental solutions according to the problem being solved), the displacement and traction Green's functions at the boundary nodes due to the artificial source can be computed. These tractions together with the artificial point load, form a well posed boundary value problem. Assuming we solve this problem by boundary element method with exactly the same discretization, we expect to obtain the displacements at the boundary nodes same as computed before (i. e., the displacement Green's functions) provided that the CPV and weakly singular integrals were evaluated accurately. Now, we invert the procedure. We assume that the diagonal 2×2 block elements of $\mathbf{H}$ ($h_{i,i}, h_{i,i+1}, h_{i+1,i}$ and $h_{i+1,i+1}$) and $\mathbf{G}$ ($g_{i,i}, g_{i,i+1}, g_{i+1,i}$ and $g_{i+1,i+1}$) for each boundary node, I, are unknown, while the displacements and tractions are known. Writing the boundary integral equations for each node I, we obtain:

$$\begin{aligned} h_{i,i}u_i + h_{i,i+1}u_{i+1} &- g_{i,i}t_i - g_{i,i+1}t_{i+1} \\ &= \sum_{j \neq i,i+1} (-h_{i,j}u_j + g_{i,j}t_j) + b_i \qquad (3.32) \\ h_{i+1,i}u_i + h_{i+1,i+1}u_{i+1} &- g_{i+1,i}t_i - g_{i+1,i+1}t_{i+1} \\ &= \sum_{j \neq i,i+1} (-h_{i+1,j}u_j + g_{i+1,j}t_j) + b_{i+1} \qquad (3.33) \end{aligned}$$

where u_j and t_j are the known displacements and tractions (Green's functions) due to the artificial source; $h_{i,j}$ and $g_{i,j}$ $(j \neq i, i+1)$ at the right hand side are the known elements of the matrices $\mathbf{H}$ and $\mathbf{G}$, and contain only regular integrals. With the concept of artificial source we obtain two equations for the eight unknowns. By choosing four independent artificial sources, we can establish eight linear algebraic

equations to solve the eight unknowns as:

$$\begin{bmatrix} u_i^1 & u_{i+1}^1 & -t_i^1 & -t_{i+1}^1 & 0 & 0 & 0 & 0 \\ 0 & 0 & 0 & 0 & u_i^1 & u_{i+1}^1 & -t_i^1 & -t_{i+1}^1 \\ u_i^2 & u_{i+1}^2 & -t_i^2 & -t_{i+1}^2 & 0 & 0 & 0 & 0 \\ 0 & 0 & 0 & 0 & u_i^2 & u_{i+1}^2 & -t_i^2 & -t_{i+1}^2 \\ u_i^3 & u_{i+1}^3 & -t_i^3 & -t_{i+1}^3 & 0 & 0 & 0 & 0 \\ 0 & 0 & 0 & 0 & u_i^3 & u_{i+1}^3 & -t_i^3 & -t_{i+1}^3 \\ u_i^4 & u_{i+1}^4 & -t_i^4 & -t_{i+1}^4 & 0 & 0 & 0 & 0 \\ 0 & 0 & 0 & 0 & u_i^4 & u_{i+1}^4 & -t_i^4 & -t_{i+1}^4 \end{bmatrix} \begin{Bmatrix} h_{i,i} \\ h_{i,i+1} \\ g_{i,i} \\ g_{i,i+1} \\ h_{i+1,i} \\ h_{i+1,i+1} \\ g_{i+1,i} \\ g_{i+1,i+1} \end{Bmatrix} = \begin{Bmatrix} r_i^1 \\ r_{i+1}^1 \\ r_i^2 \\ r_{i+1}^2 \\ r_i^3 \\ r_{i+1}^3 \\ r_i^4 \\ r_{i+1}^4 \end{Bmatrix} \tag{3.34}$$

where u_i^n and u_{i+1}^n represent the displacements at node I due to the nth artificial source, t_i^n and t_{i+1}^n are the corresponding tractions, r_i^n and r_{i+1}^n are obtained by substituting the displacements and tractions due to the nth artificial source into the right hand side of equation (3.33).

3.4.3 Numerical aspect

To illustrate the accuracy of the technique to evaluate the singular integrals we consider first a semi-infinite homogeneous isotropic plate with a vertical boundary at $x = 0$, as shown in Figure 3.4. As an example, the normalized frequency $(\omega H/c_s)$ equals to 1.0 with c_s being the shear wave speed.

The Green's functions from Chapter 2 satisfy the traction free conditions on the top and bottom surfaces automatically. The vertical boundary is discretized with ten quadratic boundary elements and twenty-one nodes (being numbered sequentially from top to bottom of the plate). By applying the technique to evaluate the singular integrals, the diagonal blocks of the assembled $\mathbf{G}$ and $\mathbf{H}$ matrices are obtained. Table 3.1 gives the results of $g_{i,i+1}$, $g_{i+1,i}$, $h_{i,i}$ and $h_{i+1,i+1}$ obtained. The four artificial sources

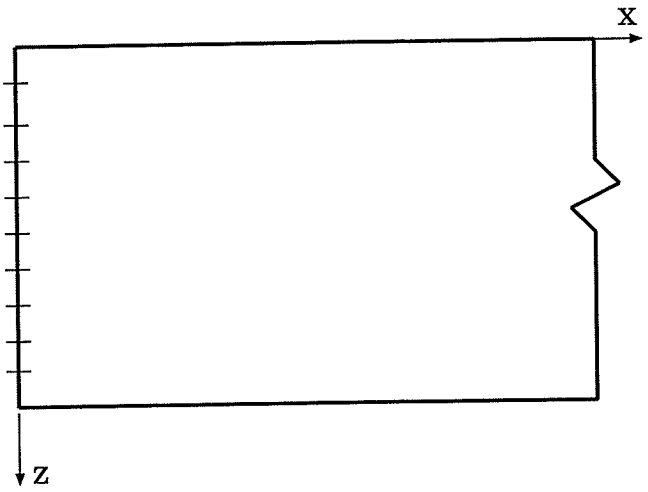

Figure 3.4: Configuration of a semi-infinite plate

are: x direction loads at points $(10H, 0)$ and $(20H, 0)$, respectively, and z direction loads at the same points.

It is to be noted that due to the symmetric conditions about the vertical line in an infinite plate and the property of the tensor c_{ij} the exact values are:

$$g_{i,i+1} = g_{i+1,i} = 0, \quad h_{i,i} = h_{i+1,i+1} = 0.5 \tag{3.35}$$

Comparing Table 2.1 with equation (3.35), we can see that the technique developed here gives good results. Also, detailed computations show that the results are very stable with the change of the artificial sources.

It may be noticed that the off-diagonal elements $g_{i,i+1}$ and $g_{i+1,i}$ in the diagonal blocks of matrix $\mathbf{G}$ do not actually contain singular integrals. In the application of the technique illustrated above, these elements are not necessary to be involved as unknowns as in equation (3.34), but they can serve as checkmarks.

Table 3.1: The diagonal block elements of $\mathbf{G}$ and $\mathbf{H}$.

node	$\lvert g_{i,i+1}\rvert$	$\lvert g_{i+1,i}\rvert$	$\lvert h_{i,i}\rvert$	$\lvert h_{i+1,i+1}\rvert$
1	0.00000	0.00000	0.50000	0.50000
2	0.00010	0.00004	0.49999	0.50011
3	0.00025	0.00019	0.50006	0.50026
4	0.00008	0.00007	0.49997	0.50007
5	0.00004	0.00030	0.50002	0.50028
6	0.00001	0.00010	0.50001	0.50008
7	0.00006	0.00036	0.49992	0.50017
8	0.00004	0.00010	0.50006	0.50012
9	0.00007	0.00024	0.49988	0.50005
10	0.00002	0.00004	0.50005	0.50010
11	0.00000	0.00000	0.49991	0.50006
12	0.00002	0.00004	0.50005	0.50010
13	0.00007	0.00024	0.49988	0.50005
14	0.00004	0.00010	0.50006	0.50012
15	0.00006	0.00036	0.49992	0.50017
16	0.00001	0.00010	0.50001	0.50008
17	0.00004	0.00030	0.50002	0.50028
18	0.00008	0.00007	0.49997	0.50007
19	0.00025	0.00019	0.50006	0.50026
20	0.00010	0.00004	0.49999	0.50011
21	0.00000	0.00000	0.50000	0.50000

3.4.4 Treatment of corner points

The evaluation of the singular integrals around corner points of the boundary contour possesses more difficulties due to the discontinuity of normals across the corner points. A double nodes technique is incorporated together with the artificial source concept.

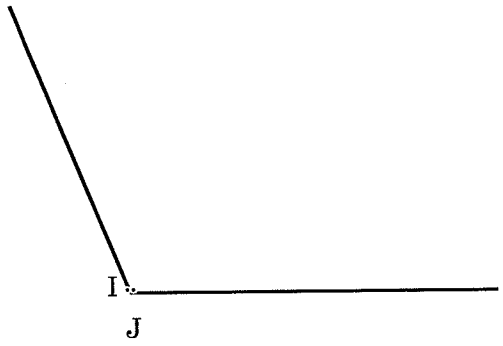

Figure 3.5: Configuration of corner points

As shown in Figure 3.5, two nodes, I and J, with the same coordinates are set on the two sides of a corner point. Applying equations (3.32) and(3.33) to point I and noticing that one more off-diagonal 2×2 block of $\mathbf{H}$ and other two off-diagonal elements in $\mathbf{G}$ corresponding to node J contain singular integrals on the right hand side of the equations (3.32) and (3.33), we can manipulate these equations as:

$$\begin{aligned} & u_i(h_{i,i} + h_{i,j}) + u_{i+1}(h_{i,i+1} + h_{i,j+1}) - t_i g_{i,i} - t_j g_{i,j} \\ = & \sum_{l \neq i,i+1,j,j+1} (-h_{i,l} u_l + g_{i,l} t_l) + g_{i,i+1} t_{i+1} + g_{i,j+1} t_{j+1} + b_i \end{aligned} \tag{3.36}$$

$$\begin{aligned} & u_i(h_{i+1,i} + h_{i+1,j}) + u_{i+1}(h_{i+1,i+1} + h_{i+1,j+1}) - t_{i+1} g_{i+1,i+1} - t_{j+1} g_{i+1,j+1} \\ = & \sum_{l \neq i,i+1,j,j+1} (-h_{i+1,l} u_l + g_{i+1,l} t_l) + g_{i+1,i} t_i + g_{i+1,j} t_j + b_{i+1} \end{aligned} \tag{3.37}$$

In the above the continuity conditions

$$u_i = u_j, \quad u_{i+1} = u_{j+1} \tag{3.38}$$

are employed. To simplify the analysis and expression, $g_{i,i+1}$ and $g_{i+1,i}$ are treated as regular terms in equations (3.36) and (3.37) since they do not actually contain singular integrals.

Applying the concept of artificial source to each of the equations (3.36) and (3.37) and choosing four artificial sources, we can establish the following two sets of linear equations:

$$\begin{bmatrix} u_i^1 & u_{i+1}^1 & -t_i^1 & -t_j^1 \\ u_i^2 & u_{i+1}^2 & -t_i^2 & -t_j^2 \\ u_i^3 & u_{i+1}^3 & -t_i^3 & -t_j^3 \\ u_i^4 & u_{i+1}^4 & -t_i^4 & -t_j^4 \end{bmatrix} \begin{Bmatrix} h_{i,i} + h_{i,j} \\ h_{i,i+1} + h_{i,j+1} \\ g_{i,i} \\ g_{i,j} \end{Bmatrix} = \begin{Bmatrix} r_i^1 \\ r_i^2 \\ r_i^3 \\ r_i^4 \end{Bmatrix} \tag{3.39}$$

$$\begin{bmatrix} u_i^1 & u_{i+1}^1 & -t_{i+1}^1 & -t_{j+1}^1 \\ u_i^2 & u_{i+1}^2 & -t_{i+1}^2 & -t_{j+1}^2 \\ u_i^3 & u_{i+1}^3 & -t_{i+1}^3 & -t_{j+1}^3 \\ u_i^4 & u_{i+1}^4 & -t_{i+1}^4 & -t_{j+1}^4 \end{bmatrix} \begin{Bmatrix} h_{i+1,i} + h_{i+1,j} \\ h_{i+1,i+1} + h_{i+1,j+1} \\ g_{i+1,i+1} \\ g_{i+1,j+1} \end{Bmatrix} = \begin{Bmatrix} r_{i+1}^1 \\ r_{i+1}^2 \\ r_{i+1}^3 \\ r_{i+1}^4 \end{Bmatrix} \tag{3.40}$$

Also, equations corresponding to nodes I and J in (3.31) are modified according to the continuity condition (3.38) so that the solutions from (3.39) and (3.40) can be applied.

3.5 Application of BEM in crack problems

As is known, the direct boundary element method for a crack geometry fails: the discretization of the whole domain boundary, including both crack surfaces, yields a singular system of equation.

3.5.1 Difficulties in crack modelling

It is recalled (equation (3.28)) that the displacement at an interior point $\mathbf{x}'$, in the absence of a body force term b_j, is given by

$$u_i(\mathbf{x}') = \int_{S+\Gamma^+ +\Gamma^-} [G_{ij}(\mathbf{x},\mathbf{x}')t_j(\mathbf{x}) - H_{ij}(\mathbf{x},\mathbf{x}')u_j(\mathbf{x})]dS \tag{3.41}$$

where Γ^+ and Γ^- represent the upper and lower crack surfaces and S represents the remaining regular boundary, as shown in Figure 3.6. Mathematically, Γ^+ and Γ^- occupy the same points. So the displacement kernel G_{ij} and the traction kernel H_{ij} for points on the upper $\mathbf{x}^+$ and lower $\mathbf{x}^-$ crack surfaces have the property that

$$\begin{aligned} G_{ij}(\mathbf{x}^+,\mathbf{x}') &= G_{ij}(\mathbf{x}^-,\mathbf{x}') \\ H_{ij}(\mathbf{x}^+,\mathbf{x}') &= -H_{ij}(\mathbf{x}^-,\mathbf{x}'). \end{aligned} \tag{3.42}$$

The change in sign in (3.42) is because the direction of the normal is opposite on the crack surfaces.

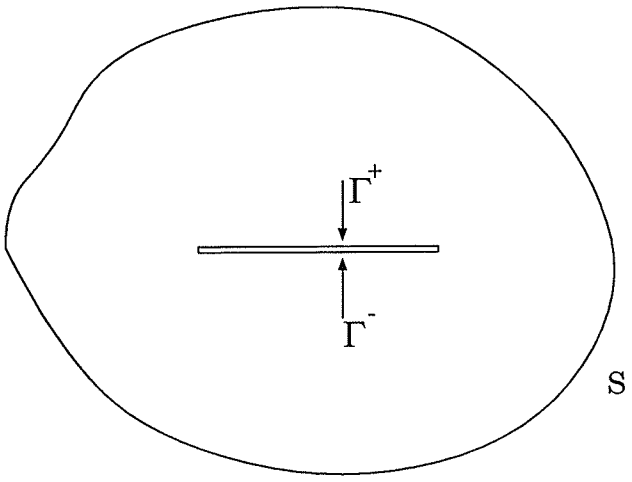

Figure 3.6: Crack surface geometry

By collapsing the two crack surfaces equation (3.41) becomes

$$u_i(\mathbf{x}') = \int_S [G_{ij}(\mathbf{x},\mathbf{x}')t_j(\mathbf{x}) - H_{ij}(\mathbf{x},\mathbf{x}')u_j(\mathbf{x})]dS$$

$$+ \int_\Gamma [G_{ij}(\mathbf{x},\mathbf{x}')\Sigma t_j(\mathbf{x}) - H_{ij}(\mathbf{x},\mathbf{x}')\Delta u_j(\mathbf{x})]d\Gamma \tag{3.43}$$

where Γ represents the midsurface, and

$$\begin{aligned} \Delta u_j &= u_j(\mathbf{x}^+) - u_j(\mathbf{x}^-) \\ \Sigma t_j &= t_j(\mathbf{x}^+) + t_j(\mathbf{x}^-) \end{aligned} \tag{3.44}$$

In the usual crack problems the tractions on the two crack surfaces are equal and opposite, such that $\Sigma t_j = 0$.

Following the conventional BEM derivation, let $\mathbf{x}' \to \mathbf{x}$ on the boundary Γ, we obtain:

$$\begin{aligned} u_i(\mathbf{x}') - \Delta u_i(\mathbf{x}')/2 &= \int_S [G_{ij}(\mathbf{x},\mathbf{x}')t_j(\mathbf{x}) - H_{ij}(\mathbf{x},\mathbf{x}')u_j(\mathbf{x})]dS \\ &- \int_\Gamma H_{ij}(\mathbf{x},\mathbf{x}')\Delta u_j(\mathbf{x})d\Gamma \end{aligned} \tag{3.45}$$

Equation (3.45) has two serious deficiencies:

1. any set of equal and opposite tractions on the crack surface Γ will result in the same equation.

2. there are now two unknown displacement variables on Γ, namely Δu_i and u_i.

3.5.2 Multidomain technique

The essence of multidomain technique is multidomain discretizations. By writing the bounadry integral equation (3.28) for each domain, invoking the auxiliary constraints on the interface, we can obtain sufficient number of equations to solve the crack problem.

As shown in Figure 3.7, the cracked body is divided into two regions (or domains), with each region containing one crack surface. The boundary integral equations are

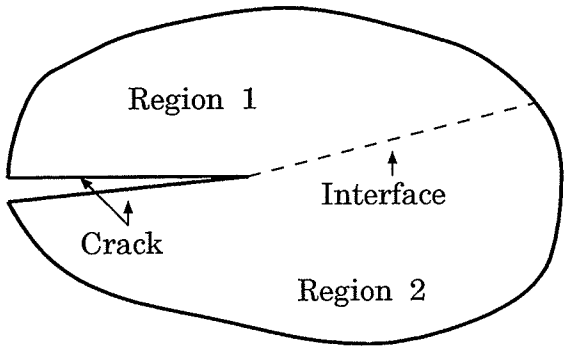

Figure 3.7: partitioning of a cracked body

written for each domain, respectively. If $\mathbf{u}_I^{(i)}$ and $\mathbf{t}_I^{(i)}$ are the vectors of displacements and tractions on the interface boundaries of region i, then they satisfy:

$$\begin{aligned} \mathbf{u}_I^{(1)}(\mathbf{x}) &= \mathbf{u}_I^{(2)}(\mathbf{x}) \quad (= \mathbf{u}_I) \\ \mathbf{t}_I^{(1)}(\mathbf{x}) &= -\mathbf{t}_I^{(2)}(\mathbf{x}) \quad (= \mathbf{t}_I) \end{aligned} \tag{3.46}$$

The matrix representation (3.31) is modified as following:

$$[\mathbf{H}^{(1)} \quad \mathbf{H}_I^{(1)}] \begin{Bmatrix} \mathbf{u}^{(1)} \\ \mathbf{u}_I^{(1)} \end{Bmatrix} = [\mathbf{G}^{(1)} \quad \mathbf{G}_I^{(1)}] \begin{Bmatrix} \mathbf{t}^{(1)} \\ \mathbf{t}_I^{(1)} \end{Bmatrix} \tag{3.47}$$

for region 1, and

$$[\mathbf{H}^{(2)} \quad \mathbf{H}_I^{(2)}] \begin{Bmatrix} \mathbf{u}^{(2)} \\ \mathbf{u}_I^{(2)} \end{Bmatrix} = [\mathbf{G}^{(2)} \quad \mathbf{G}_I^{(2)}] \begin{Bmatrix} \mathbf{t}^{(2)} \\ \mathbf{t}_I^{(2)} \end{Bmatrix} \tag{3.48}$$

for region 2, where $\mathbf{H}_I^{(i)}$ and $\mathbf{G}_I^{(i)}$ are the matrix coefficient entries corresponding to nodes on the interface.

Combining the coefficient matrices for the two regions, applying the interface continuity conditions results in the system of equations as

$$\begin{bmatrix} \mathbf{H}^{(1)} & \mathbf{H}_I^{(1)} & -\mathbf{G}_I^{(1)} & 0 & \\ 0 & \mathbf{H}_I^{(2)} & -\mathbf{G}_I^{(2)} & \mathbf{H}^{(2)} & 0 \end{bmatrix} \begin{Bmatrix} \mathbf{u}^{(1)} \\ \mathbf{u}_I \\ \mathbf{t}_I \\ \mathbf{u}^{(2)} \end{Bmatrix} = \begin{bmatrix} \mathbf{G}^{(1)} & 0 \\ 0 & \mathbf{G}^{(2)} \end{bmatrix} \begin{Bmatrix} \mathbf{t}^{(1)} \\ \mathbf{t}^{(2)} \end{Bmatrix} \tag{3.49}$$

The multidoman technique illustrated above is a general method in the boundary element analysis. It is widely used in the analysis of large structures, domains with different materials, and domains with cracks.

3.5.3 Crack-tip elements

The stress field is singular $O(1/\sqrt{r})$ at the crack tip and the displacement field varies as $O(\sqrt{r})$, with r being the distance from the crack tip. Therefore modelling crack regions with the usual shape functions, which allow for polynomial variation only, does not lead to accurate solutions unless extremely fine meshes are used in the region near the crack-tip.

Henshell and Shaw [65] and Barsoum [66] showed that an 8-node quadrilateral element will possess the required singularity if the mid-side nodes are placed at quarter-points in the vicinity of the crack tip. Barsoum [67] also showed that the quarter-point six-node triangular element will have the correct behaviour in the radial direction if it is obtained by collapsing on side of the 8-node quadrilateral element.

As shown in Figure 3.8, a quarter-point crack-tip element is obtained by moving the mid-side node of a quadratic element to a quarter point position. The displacement and traction dependence on r is obtained as

$$\mathbf{u} = \mathbf{u}^1 + (-3\mathbf{u}^1 + 4\mathbf{u}^2 - \mathbf{u}^3)\sqrt{r/L} + 2(\mathbf{u}^1 - 2\mathbf{u}^2 + \mathbf{u}^3)r/L \tag{3.50}$$

$$\mathbf{t} = \mathbf{t}^1\sqrt{L/r} + (-3\mathbf{t}^1 + 4\mathbf{t}^2 - \mathbf{t}^3) + 2(\mathbf{t}^1 - 2\mathbf{t}^2 + \mathbf{t}^3)\sqrt{r/L} \tag{3.51}$$

where L is the length of the element, $\mathbf{u}^1$ and $\mathbf{t}^1$ represent the displacement and traction at the crack tip, respectively.

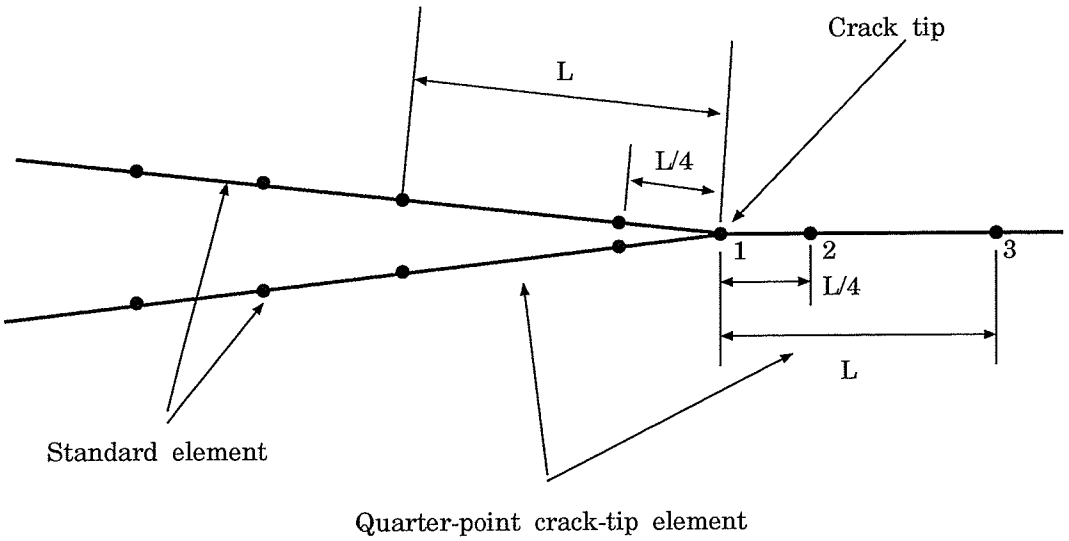

Figure 3.8: Quarter-point crack-tip elements

3.6 Numerical applications

The hybrid method and the boundary element method developed in this chapter are used to study the wave scattering problem for the following examples:

Example 1. – a homogeneous uniaxial graphite-epoxy plate with fibers aligned along the x-axis. The flaw considered is a surface-breaking vertical crack with length $L = H$ located at $x = 0$, as shown in Figure 3.9. The vertical load is applied on the top surface at $x = -10H$. The relevant elastic constants characterizing the plate material are the same as example 2 in Chapter 2. The normalized cut-off frequencies $(\omega H/c_s)$ for the first two symmetric and antisymmetric modes are $2.20, 3.14$ and $1.57, 4.40$, respectively.

Example 2. – the configuration of the plate is same as in example 1, but the flaw considered is a horizontal crack. The geometry of the problem is illustrated in Figure 3.10. The vertical load is applied on the top surface of the plate at a distance 3.5H to the left of the origin.

Example 3. – two 8-layer graphite-epoxy cross-ply laminated plates with 0°/90°/0°/90°/90°/0°/90°/0° configurations are joined edgewise by a thin isotropic elastic layer of thickness 0.05H, with and without a crack on one of the joint interface, as shown in Figure 3.11. The material properties of the 0° and 90° laminae are given in Table 2.1. The material properties of the bond layer are: density $\rho = 0.67\rho_{(\text{composite})}$, the Poisson's ratio, ν, and the shear modulus, μ, are taken to be 0.354 and 1.95 GPa, respectively. The concentrated load acts at $(-10H, 0)$.

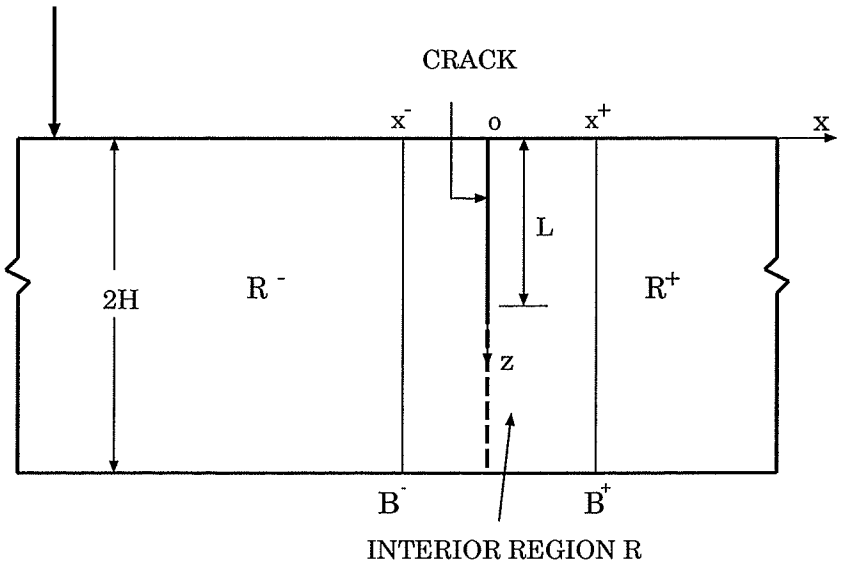

Figure 3.9: Configuration of a surface-breaking crack

The time-dependence of the load is assumed as

$$f(\tau) = \frac{2}{\sqrt{2\pi}} e^{-(\tau-\tau_0)^2/2} sin(\Omega_c \tau) \tag{3.52}$$

for examples 2 and 3, where the normalized time $\tau = c_s t/H$. The time delay τ_0 was taken as 3.0, and the normalized central frequency $\Omega_c (= \omega H/c_s)$ was taken as 3.14. The time- and frequency-dependence of the load are presented in Figures 3.12 (a) and (b). It is seen that the amplitudes approach zero after $\Omega > 6.0$. Therefore, the high frequency responses are filtered out.

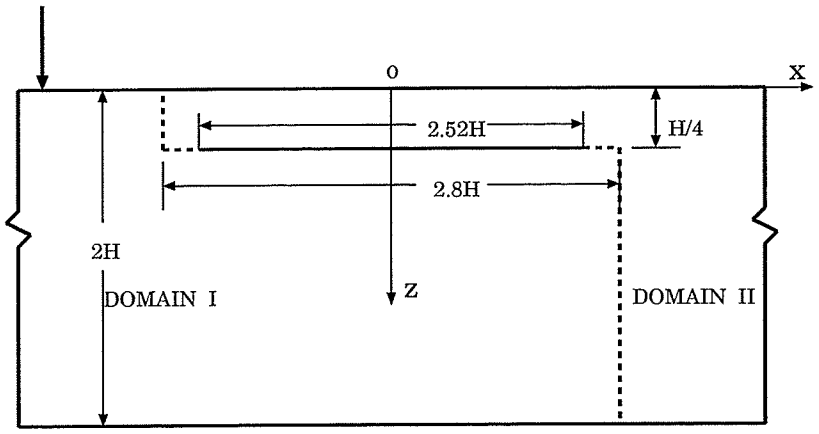

Figure 3.10: Configuration of a surface-breaking crack

Example 1. Surface-breaking crack

This example is designated to compare the results from the hybrid method and boundary element method.

In the employment of the hybrid method, the finite element region containing the crack is confined within the vertical boundaries B^- and B^+, which are taken to be $x = -0.25H$ and $x = 0.25H$, respectively. The finite element mesh consists of 64 quadratic elements and 293 nodes.

In the boundary element analysis, to circumvent the difficulties associated with the presence of the crack, the multidomain technique is employed. The plate is divided into two domains by a vertical fictitious boundary extended from the crack configuration (dashed line along z-axis as shown in Figure 3.9). The boundary element mesh is composed of 32 quadratic elements and 49 nodes. The response spectra (the amplitude of vertical displacement versus frequency) of observation points on the top surface are obtained from the two methods. Figure 3.13 represents the results of points $(-0.25H, 0)$ (which is close to the crack) and $(5H, 0)$ (which is far from the crack). In the figures FEM represents results from the hybrid method. It is seen that

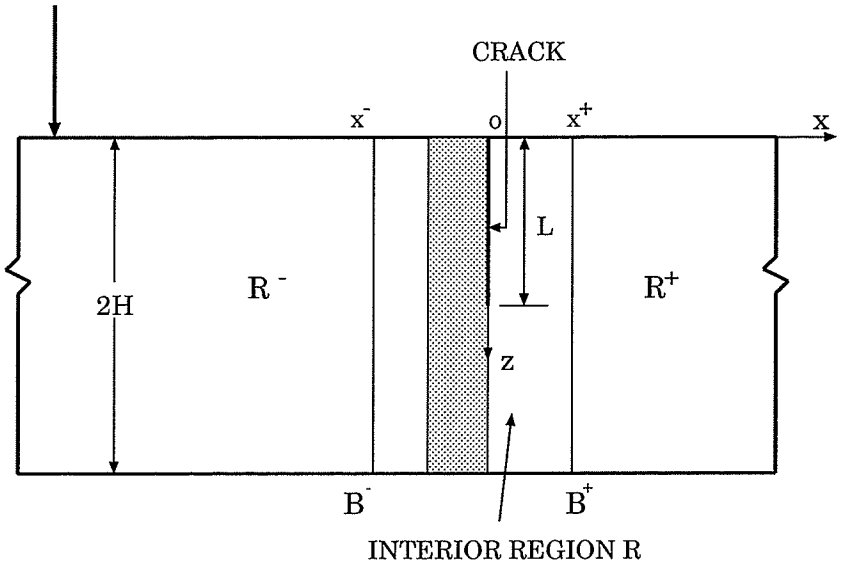

Figure 3.11: Configuration of jointed composite plate

the results from the two methods for both the near and far fields are in very good agreement.

Example 2. Horizontal crack

In the boundary element analysis the plate is divided into two domains by the crack and the fictitious boundaries (Figure 3.10, dashed line). The boundary element mesh is composed of 124 quadratic elements and 204 nodes. Eight crack tip singular elements are used. In the application of hybrid method the plate is divided into two regions: interior region bounded by two vertical boundaries at $x = -1.4H$ and $x = 1.4H$, and exterior region. The finite element mesh is composed of 392 quadratic elements and 1280 nodes.

The vertical displacements at two sections, $x = -1.4H$ and $x = 5H$, from the two methods are presented in Figure 3.14 for $\Omega = 1$ (the results from hybrid method are referred as FEM in the figure). It is noted that due to a fairly large discretized

region, the accuracy of the hybrid method degenerates especially in the near field. The results in the far field are in better agreement, as expected. The CPU time to solve this problem on an IBM RS6000/590 computer is: 4 minutes and 20 seconds for BEM, 20 minutes and 55 seconds for hybrid method.

Figures 3.15 (a) and (b) show the frequency response of the top surface in the absence and presence of crack, respectively. The peaks at the cut-off frequencies for the first symmetric (2.20) and the second antisymmetric (4.40) are clearly seen in the absence of crack in Figure 3.15(a). In the presence of crack, two significant features are observed which can be exploited to determine its size and location. First, the peaks at the cut-off frequency for the first antisymmetric mode (1.57) are prominent at the points between the crack tips. Specifically, the surface response shows two pronounced maxima almost symmetric about the origin above the center of the crack center, as illustrated in Figure 3.16. It is noted that each peak is at the point with $L/4$ distance from the origin (L is the crack length). This feature can be used to estimate the crack length. For example, the left peak in Figure 3.16 is at $-0.63H$, which gives the crack length to be $2.52H$. Secondly, there is a pronounced peak at $\Omega = 0.55$ (also shown in Figure 3.17 for the origin). This peak is due to the resonance of the plate of finite length L above the crack. This feature can be used to determine the depth of crack. Since the ratio of crack length ($2.52H$) to its depth ($H/4$) is large (> 10), we can use locally the plate bending theory to determine the resonance frequency. The natural frequency of this plate is 0.54 for simply supported ends. The same results were observed by Datta et al. [26]. Similar conclusions were drawn by Keer et al. [68] and Cawley and Theodorakopoulos [69] that the resonance frequency for a defect may be predicted by using plate theory with length equal to crack length and thickness equal to crack depth.

Transient response of the top surface, for the load acting at the same location as before, in the absence and presence of crack is presented in Figures 3.18(a) and (b),

respectively. It is seen that the predominant response is due to the Rayleigh wave that is traveling at a speed, determined as about 1.8 $mm/\mu s$ in the absence of crack. In the presence of crack, however, the surface response is fairly complicated. Due to the diffraction of Rayleigh waves by the left crack tip, both dilatational and shear waves are generated. These waves, together with the Rayleigh waves, travel between top surface of the plate and the new boundary – crack surface. Multiple reflections of waves between the boundary surfaces occur in this part with mode conversions. This is reflected in the complicated surface response at early time above the crack (Figure 3.18(b)). Figure 3.19 shows the response at the point above the right crack tip. The presence of the crack is seen to greatly modify the signal.

Example 3. Jointed composite plates

It may be noted that the boundary element technique illustrated above is not directly applicable to solve this problem. Therefore, the hybrid method is employed.

Figures 3.20 and 3.21 show the frequency spectrum and dispersion curves for the eight-layer cross-ply laminated plate. Table 3.2 shows the normalized cut–off frequencies for $\Omega < 10$.

Figures 3.22 (a) and (b) show the displacement spectra at two observation points, $(-0.2H, 0)$ and $(0.15H, 0)$, in the cases of non-crack, crack lengths $H/2$ and H. In these figures, the sharp changes at first symmetric (2.204) and third antisymmetric (4.408) cut-off frequencies are prominent. It can be seen from Figure 3.23(a) that the response to the cut-off frequency of first antisymmetric mode (1.277) is invoked only by the longer crack, and the reflection of waves with central freqency around this frequency from the longer crack dominates the response. On the other hand, Figure 3.22(a) also shows that the reflection of waves with central frequency around $\Omega = 3.0$ from the shorter crack is more predominant, while the transmission of these

Table 3.2: Cut–off frequencies in a 8-layered cross-ply composite plate.

Mode	Symmetric	Antisymmetric
1	2.204	1.277
2	2.447	3.840
3	5.094	4.408
4	6.612	6.300
5	7.081	8.817
6		9.162

waves is greatly reduced by the longer crack, as shown in Figure 3.22(b).

Figure 3.23 represents the time-domain response of the two observation points. The arrival time of the maximum response at point $(-0.2H, 0)$ being at $\tau = 15.2$ gives the Rayleigh wave velocity at $0.776c_s$ (noting that the maximum of the load reaches at $\tau = 2.5$), while the Rayleigh wave velocity is determined at $0.79c_s$ from Figure 3.21. The estimated error is less than 3 percent.

The dynamic response of point $(-0.2H, 0)$, as shown in Figure 3.23(a), is magnified after the arrival of the Rayleigh waves due to the reflection from cracks. Also, it is seen that the reflection from the shorter crack is larger than that from longer crack. This is because reflection of incident waves with central frequency at $\Omega_c = 3.14$ is more predominant with the shorter crack.

It is seen in Figure 3.23(b) that the arrival time of the waves increases with the length of the crack. Also the amplitude of the response in the presence of longer crack is significantly reduced.

3.7 Concluding remarks

In this chapter, a general boundary element method for solving elastic wave scattering by cracks in laminated composite plates has been presented. A new technique is developed to evaluate the Cauchy Principal Value and weakly singular integrals arising in the boundary integral equations. This technique is also extended to treat the corner points where the normals are discontinuous.

A hybrid method is also extended to analyze the wave scattering problem due to external load on the laminated composite plate. Since the incident field is computed by employing the Green's functions, the extenal load can be applied anywhere on the plate.

Numerical results from the hybrid method and boundary element method for plates with surface-breaking and horizontal cracks are in very good agreement. It is shown that the application of these techniques in nondestructive evaluation of defects is very promising.

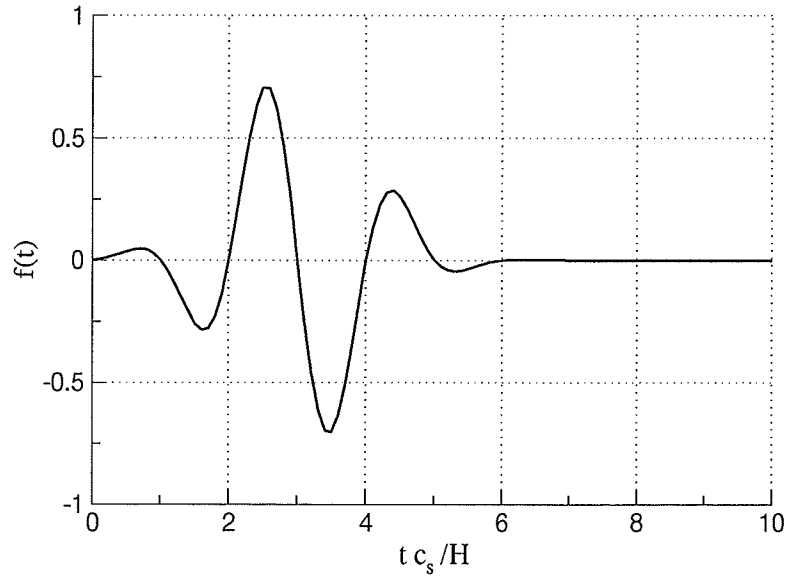

(a)

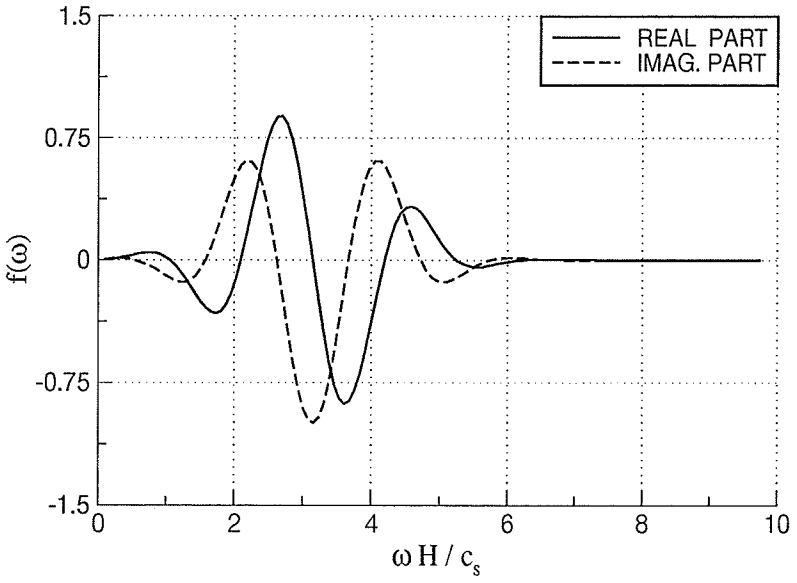

(b)

Figure 3.12: The configuration of load. (a) time–dependence, (b) frequency–dependence

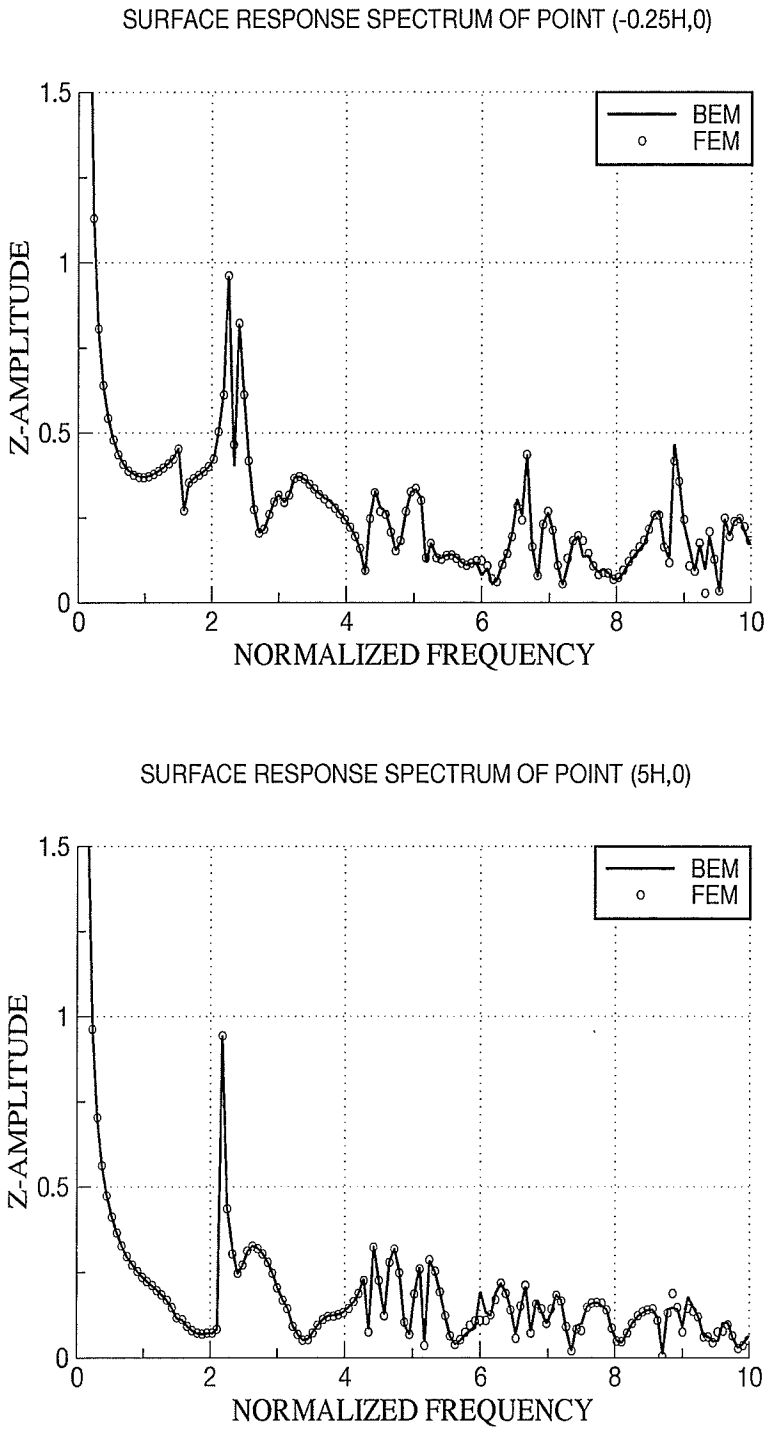

Figure 3.13: Surface response spectra of points $(-0.25H, H)$ and $(5H, 0)$.

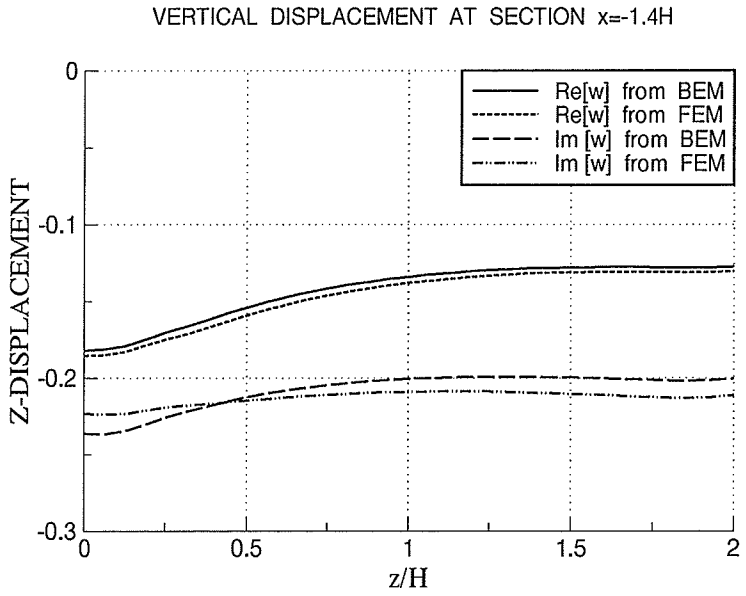

(a)

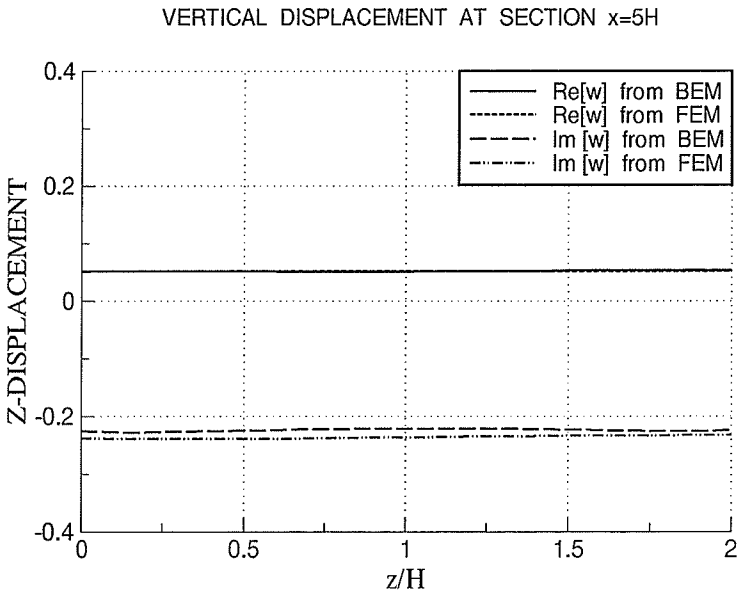

(b)

Figure 3.14: Vertical displacement at two sections for $\Omega = 1$, (a) $x = -1.4H$, (b) $x = 5H$.

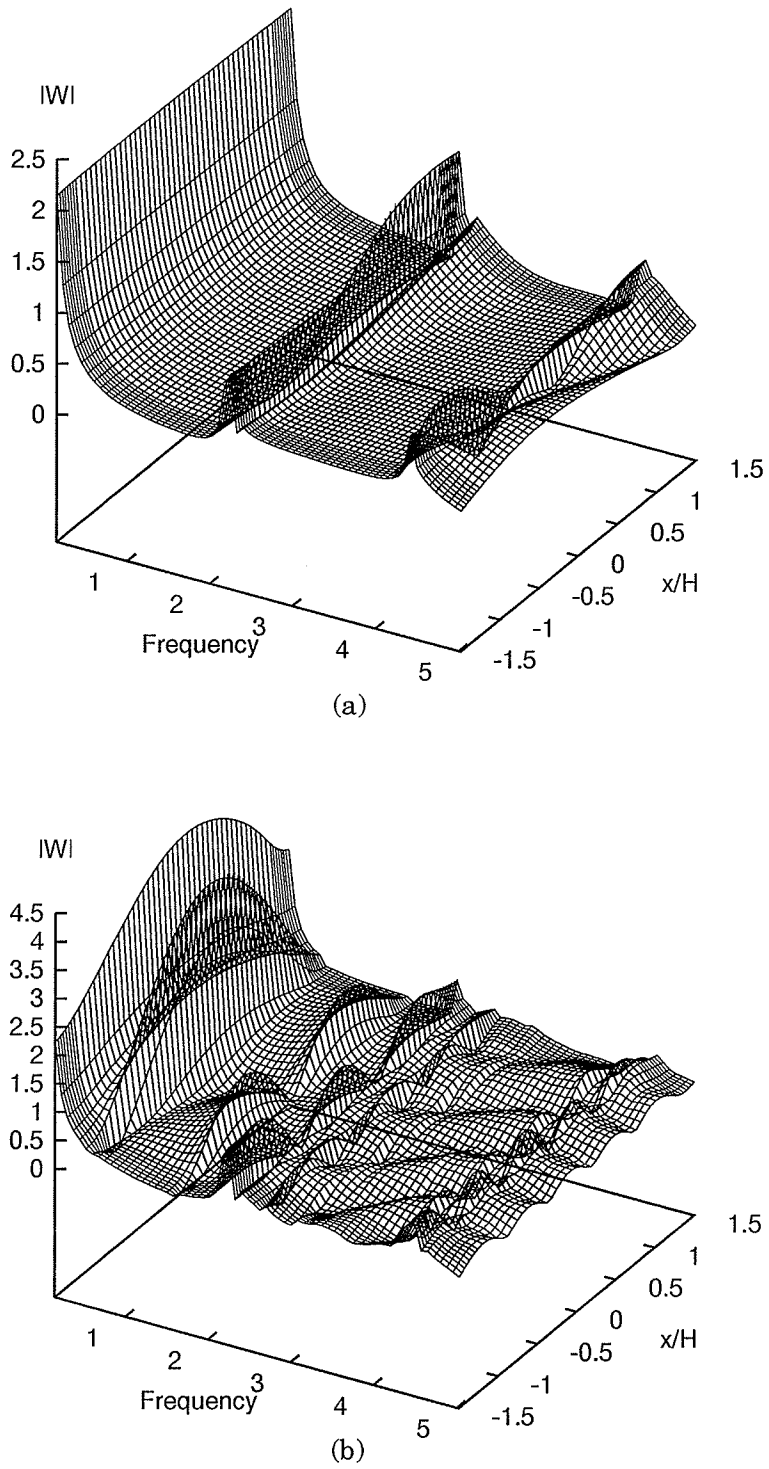

Figure 3.15: Response spectra at top surface, (a) without crack, (b) with crack.

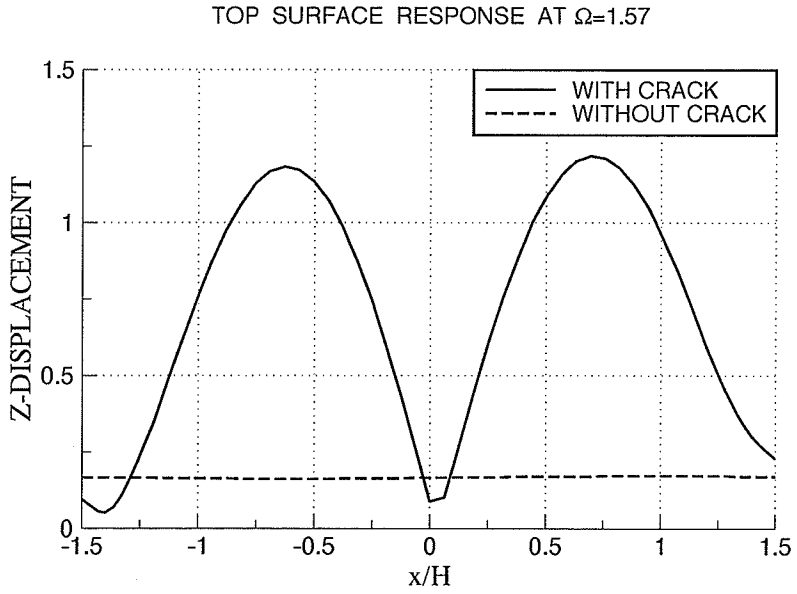

Figure 3.16: Top surface response at $\Omega = 1.57$.

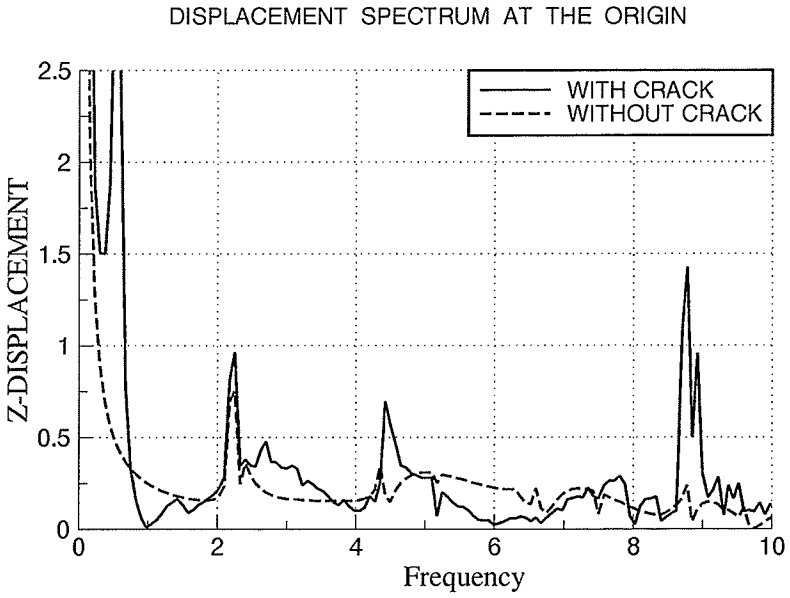

Figure 3.17: Displacement spectrum at the origin.

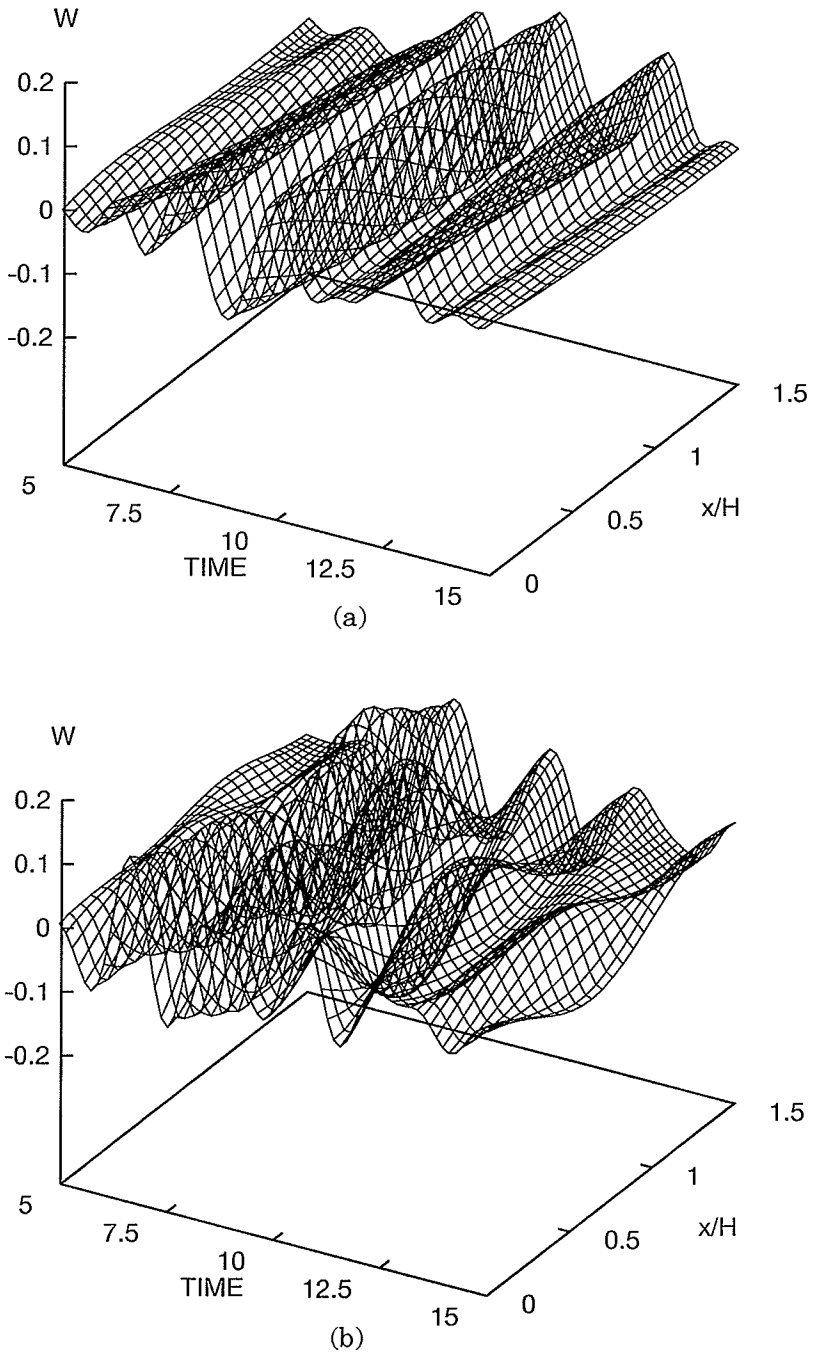

Figure 3.18: Transient response of top surface, (a) without crack, (b) with crack.

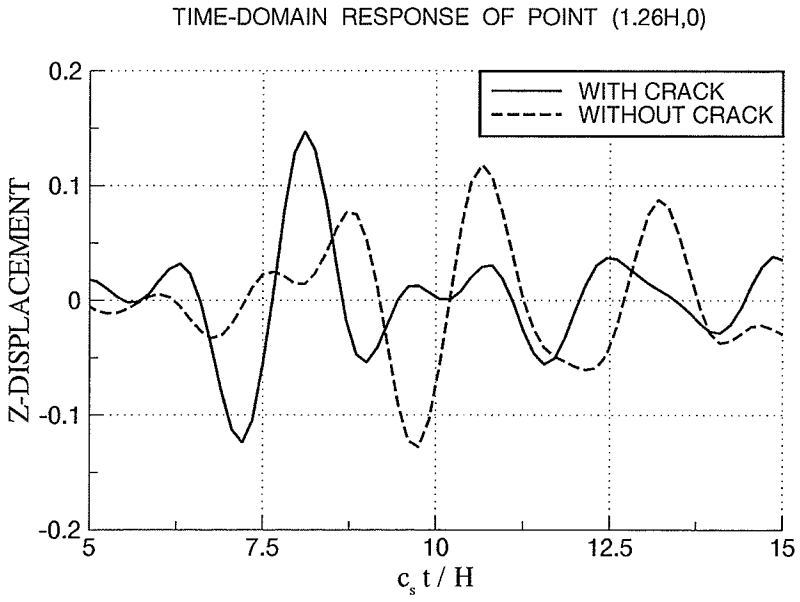

Figure 3.19: Transient response of point (1.26H,0).

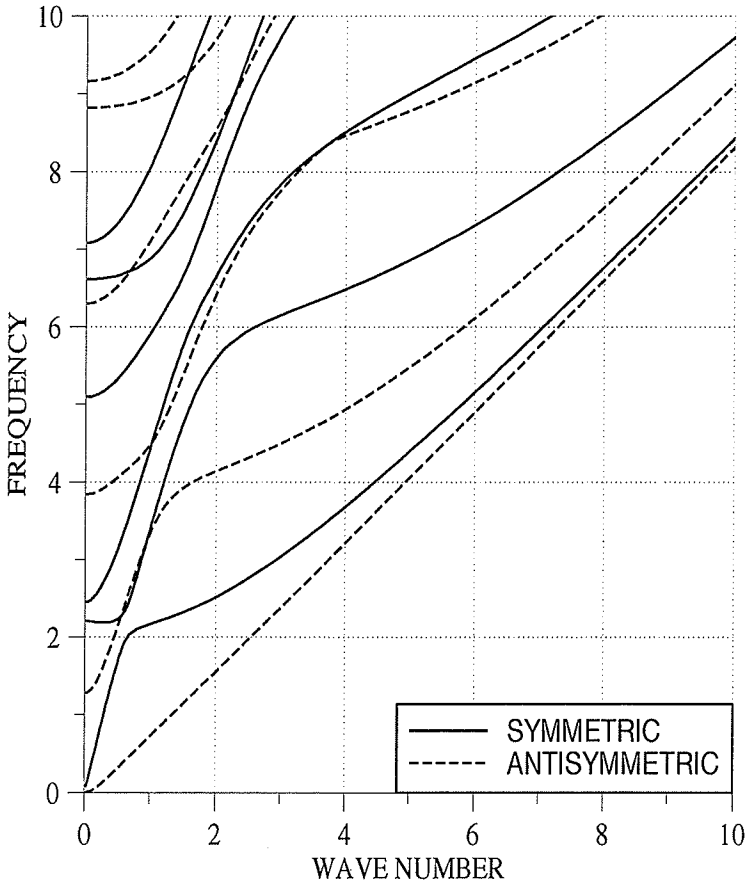

Figure 3.20: Frequency spectrum for 8-layer plate.

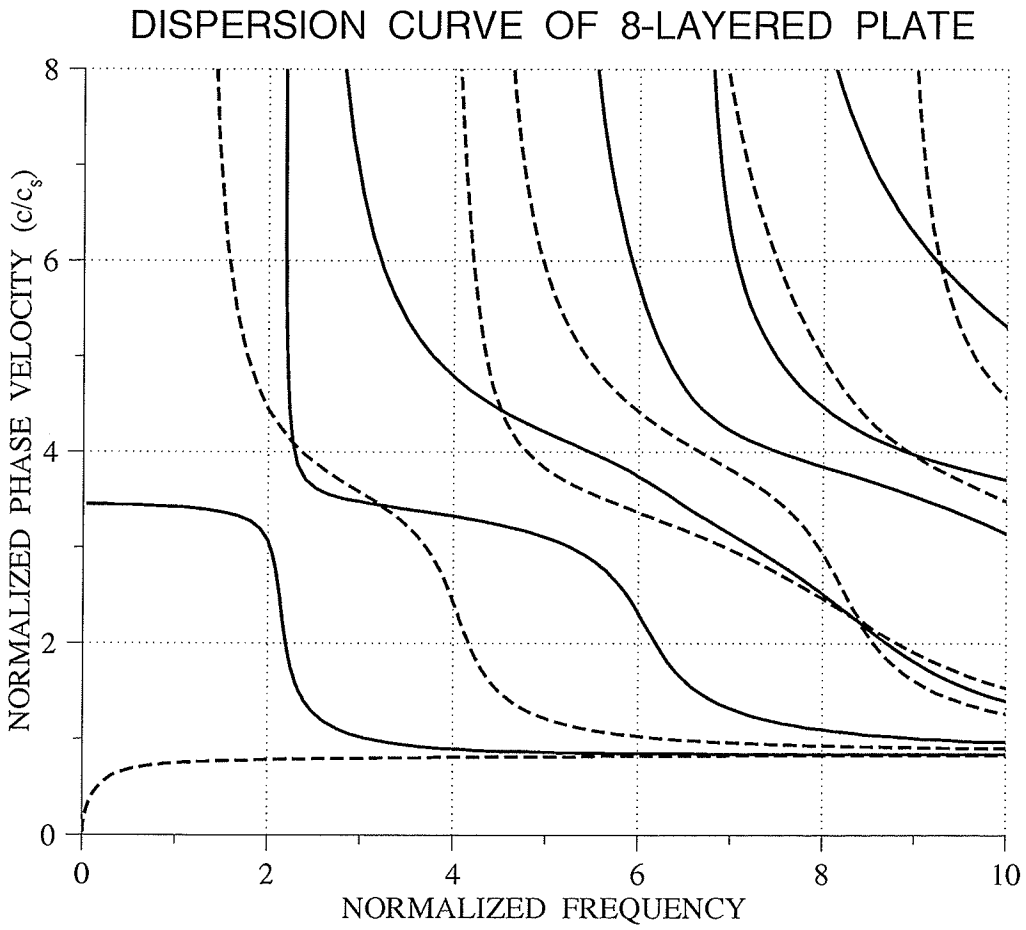

Figure 3.21: Dispersion curves for 8-layer composite plate. Solid lines: symmetric mode; dashed lines: antisymmetric mode.

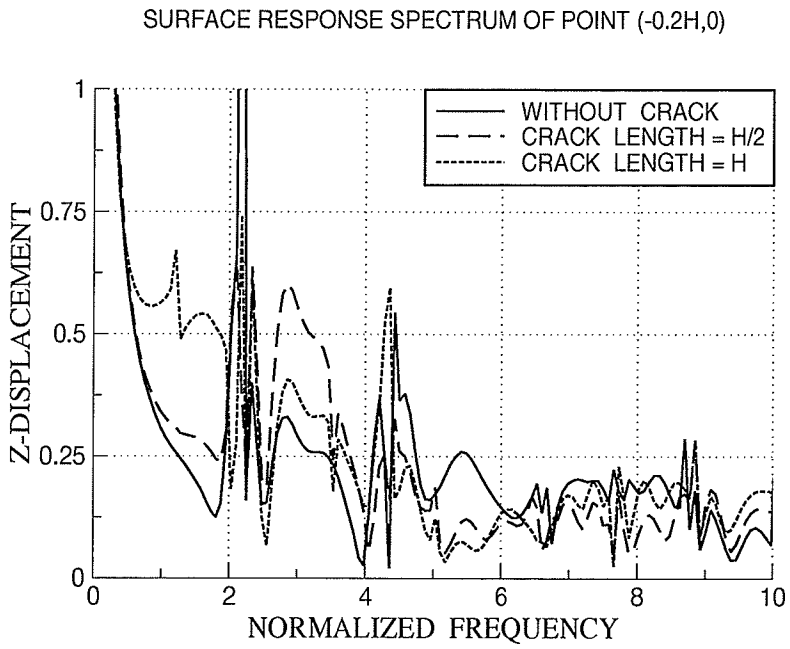

(a)

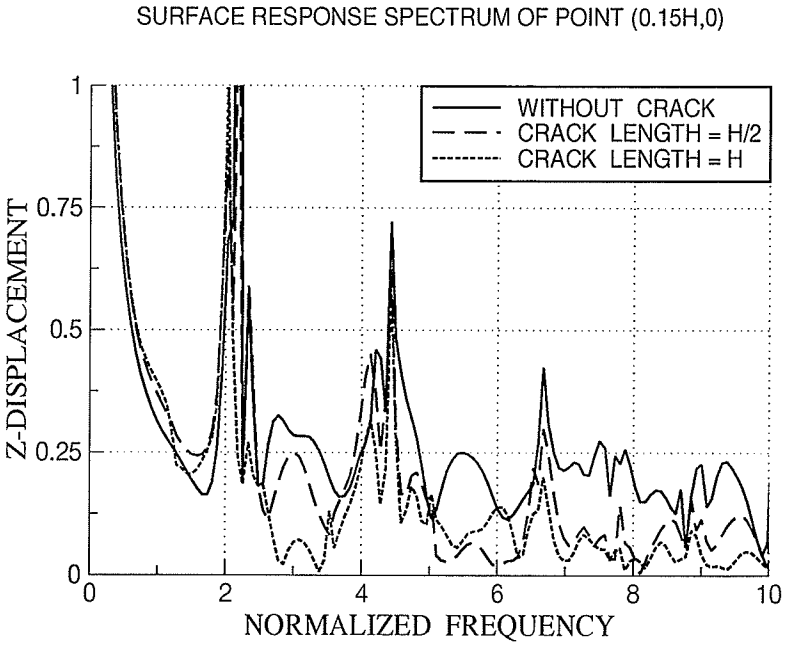

(b)

Figure 3.22: Vertical displacement spectra of surface points. (a) point (-0.2H,0), (b) point (0.15H,0).

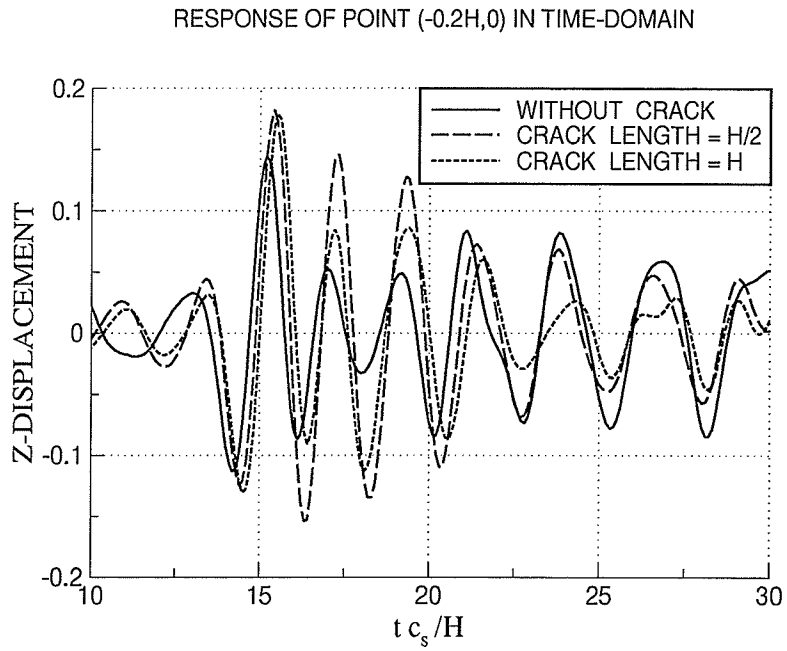

(a)

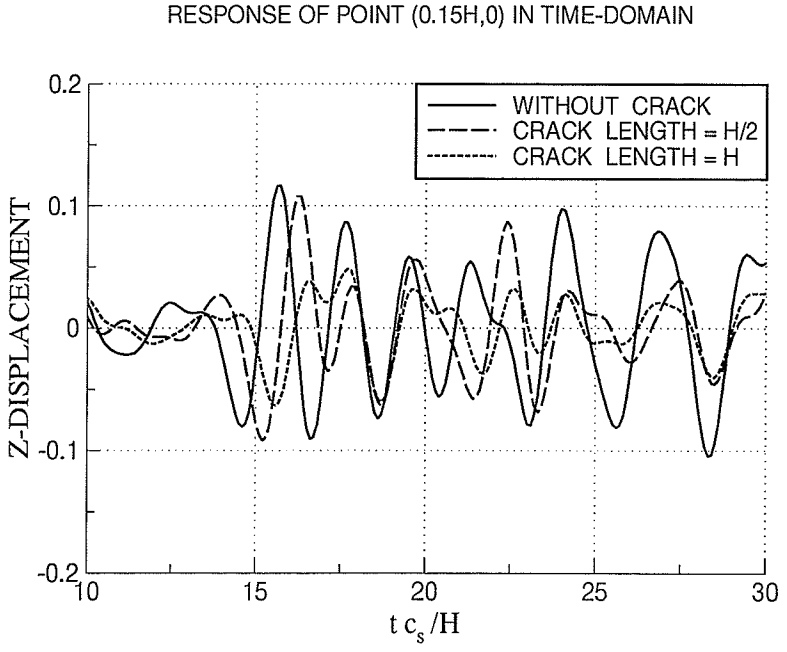

(b)

Figure 3.23: Transient response spectra of surface points. (a) point (-0.2H,0), (b) point (0.15H,0).

Chapter 4

3-D Waves in Isotropic Plates

4.1 General

Many engineering problems for elastic wave scattering are three dimensional. Very few computationally efficient methods exist for the analysis of three-dimensional wave phenomena in plates. This Chapter and the following one focus on these problems.

An analytical formulation for frequency equation and wave functions is derived for the investigation of circular-crested waves in an isotropic plate. The hybrid method presented in Chapter 3 for plane strain analysis is extended to compute the dynamic response of the plate due to a vertical load (axisymmetric problem).

By employing Fourier transform, a decomposition technique is developed to analyze the three-dimensional waves. It is shown that the three-dimensional wave propagation problem can be decomposed into a series of plane-strain and antiplane problems. The application of Rayleigh-Ritz type approximation based stiffness method and modal summation technique gives a general formulation for Green's functions corresponding to point loads in *arbitrary* directions. Numerical results from the two models are in very good agreement.

Boundary element method is exploited in the analysis of three-dimensional wave scattering problem. The technique developed in Chapter 3 for the evaluation of singular integrals arising from boundary integral equations is extended to three-dimensional analysis.

4.2 Description of the problem

Time-harmonic elastic wave propagation and scattering in an infinite isotropic plate is considered. Two coordinate systems (x, y, z) and (r, θ, z) are chosen on top of the plate, as shown in Figure 4.1. The thickness of the plate is assumed to be $2H$.

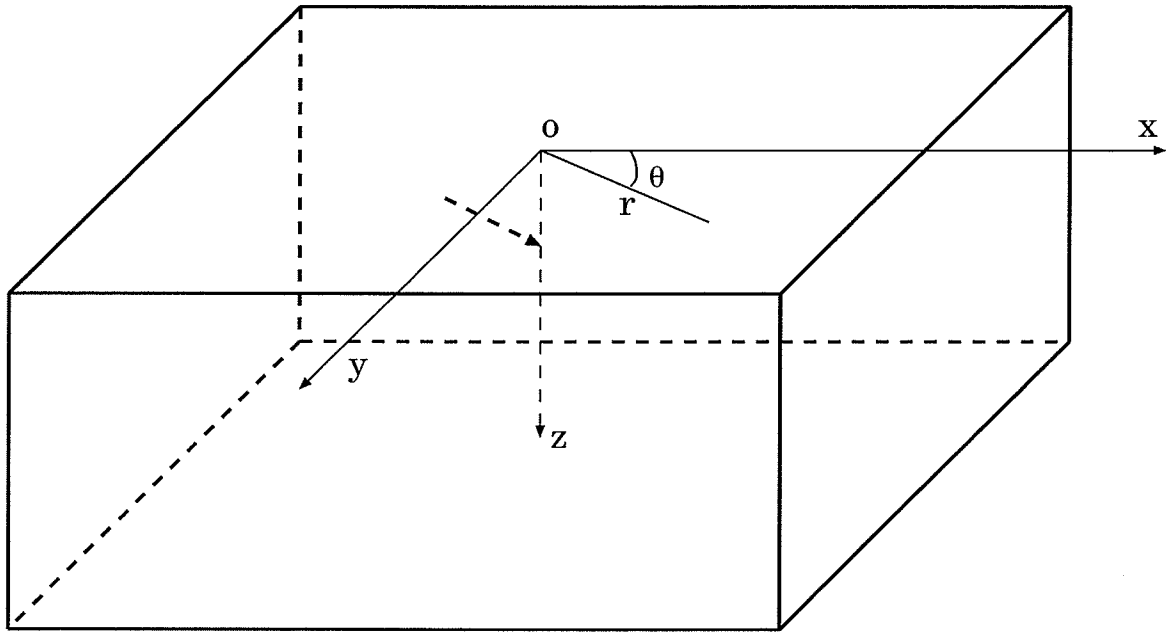

Figure 4.1: Configuration of an isotropic plate

4.3 3-D wave propagation and Green's functions

In this section, three-dimensional wave phenomenon in an isotropic plate is considered. An analytical formulation is established to analyze circular-crested waves generated by a vertical point load. Axisymmetric condition is utilized in the analysis. To compute the dynamic response of the plate to the vertical load, the hybrid method is explored. A decomposition technique is developed in the study of general case of three-dimensional wave propagation. Green's functions for point loads in arbitrary directions are derived in modal summation forms.

4.3.1 Axisymmetric case

Circular crest waves generated by a vertical direction point load are investigated. In this case, axisymmetric condition holds.

4.3.1.1 Governing equations

The displacement-strain relation in the (r, θ, z) coordinate system can be expressed as

$$\epsilon = \mathbf{L}\mathbf{u} \tag{4.1}$$

where

$$\mathbf{u}^T = \{\, u \quad w \,\}, \tag{4.2}$$

u and w are displacements in r and z directions, and

$$\mathbf{L}^T = \begin{bmatrix} \frac{\partial}{\partial r} & 1/r & 0 & \frac{\partial}{\partial z} \\ 0 & 0 & \frac{\partial}{\partial z} & \frac{\partial}{\partial r} \end{bmatrix} \tag{4.3}$$

$$\{\epsilon\}^T = [\, \epsilon_{rr} \quad \epsilon_{\theta\theta} \quad \epsilon_{zz} \quad \epsilon_{rz} \,] \tag{4.4}$$

ϵ_{ij} represents strain components in the (r, θ, z) coordinate system.

The stress-strain relation is given by

$$\begin{aligned} \sigma_{rr} &= \lambda\Delta + 2\mu\epsilon_{rr} \\ \sigma_{\theta\theta} &= \lambda\Delta + 2\mu\epsilon_{\theta\theta} \\ \sigma_{zz} &= \lambda\Delta + 2\mu\epsilon_{zz} \\ \sigma_{rz} &= 2\mu\epsilon_{rz} \end{aligned} \tag{4.5}$$

where λ and μ are Lame's constants, and

$$\Delta = \epsilon_{rr} + \epsilon_{\theta\theta} + \epsilon_{zz} \tag{4.6}$$

The equations of motion can be expressed in terms of u, w and Δ as

$$\begin{aligned} (\lambda+\mu)\frac{\partial\Delta}{\partial r} + \mu\nabla^2 u - \mu\frac{u}{r^2} + b_r &= -\rho\omega^2 u \\ (\lambda+\mu)\frac{\partial\Delta}{\partial z} + \mu\nabla^2 w + b_z &= -\rho\omega^2 w \end{aligned} \tag{4.7}$$

where b_r and b_z are body forces in r and z directions, respectively, ρ the mass density, ω the circular frequency, and

$$\nabla^2 = \frac{\partial^2}{\partial r^2} + \frac{1}{r}\frac{\partial}{\partial r} + \frac{\partial^2}{\partial z^2} \tag{4.8}$$

4.3.1.2 Wave functions

The appropriate solutions to equation (4.7) in the absence of body forces are:

$$\begin{aligned} u &= U(z')H_1^{(1)}(kr) \\ w &= W(z')H_0^{(1)}(kr) \end{aligned} \tag{4.9}$$

where $z' = z - H$; k is the wavenumber; $H_0^{(1)}(kr)$ and $H_1^{(1)}(kr)$ are Hankel functions of first kind; and the functions (wave functions) through the thickness are

$$\begin{aligned} U(z') &= k(-Bsin\alpha z' + C\beta sin\beta z'), \\ W(z') &= \alpha Bcos\alpha z' + Ck^2\beta cos\beta z', \end{aligned} \tag{4.10}$$

for antisymmetric case, and

$$\begin{aligned} U(z') &= -k(Acos\alpha z' + D\beta cos\beta z'), \\ W(z') &= -\alpha Acos\alpha z' + Dk^2 sin\beta z', \end{aligned} \tag{4.11}$$

for symmetric case, where

$$\alpha^2 = \omega^2/c_p^2 - k^2, \quad \beta^2 = \omega^2/c_s^2 - k^2 \tag{4.12}$$

$$\begin{aligned} B/C &= 2\beta k^2 sin\beta H/(k^2-\beta^2)sin\alpha H, \\ A/D &= -2\beta k^2 cos\beta H/(k^2-\beta^2)cos\alpha H, \end{aligned} \tag{4.13}$$

c_p and c_s are the longitudinal and shear wave speeds, respectively.

The stresses corresponding to the displacement field (4.9) are

$$\begin{aligned} \sigma_{rr} &= (-\gamma^2 Bsin\alpha z' + 2\beta k^2 Csin\beta z')H_0^{(1)}(kr) \\ &\quad +2\mu k/r(Bsin\alpha z' - C\beta sin\beta z')H_1^{(1)}(kr), \\ \sigma_{zz} &= [-B(\beta^2-k^2)sin\alpha z' - 2\beta k^2 Csin\beta z']H_0^{(1)}(kr), \\ \sigma_{rz} &= [-2\alpha Bcos\alpha z' + C(\beta^2-k^2)cos\beta z']kH_1^{(1)}(kr) \end{aligned} \tag{4.14}$$

for antisymmetric case, and

$$\begin{aligned} \sigma_{rr} &= -(\gamma^2 Acos\alpha z' + 2\beta k^2 Dcos\beta z')H_0^{(1)}(kr) \\ &\quad +2\mu k/r(Acos\alpha z' + D\beta cos\beta z')H_1^{(1)}(kr), \\ \sigma_{zz} &= [-A(\beta^2-k^2)cos\alpha z' + 2\beta k^2 Dcos\beta z']H_0^{(1)}(kr), \\ \sigma_{rz} &= [2\alpha Asin\alpha z' + D(\beta^2-k^2)sin\beta z']kH_1^{(1)}(kr) \end{aligned} \tag{4.15}$$

for symmetric case, where

$$\gamma^2 = (\lambda + 2\mu)k^2 + \lambda\alpha^2 \tag{4.16}$$

Frequency equations are obtained by satisfying the traction free conditions on the surfaces of the plate as:

$$(k^2 - \beta^2)^2 sin\alpha H cos\beta H + 4\alpha\beta k^2 cos\alpha H sin\beta H = 0 \tag{4.17}$$

for antisymmetric case, and

$$(k^2 - \beta^2)^2 cos\alpha H sin\beta H + 4\alpha\beta k^2 sin\alpha H cos\beta H = 0 \tag{4.18}$$

for symmetric case.

Equations (4.17) and (4.18) are the same as the Rayleigh-Lamb frequency equations for straight-crested waves (plane strain). For given ω, these equations serve as implicit transcendental functions of k. By solving these equations wavenumbers are obtained. The wave functions can be computed from equations (4.10) and (4.11).

It may be noted that the solution to equation (4.7) can be expressed either in terms of Bessel functions of first and second order, $J_0(kr), J_1(kr)$ and $Y_0(kr), Y_1(kr)$, respectively, or in terms of Hankel functions of the first and second kind, $H_0^{(1),(2)}, H_1^{(1),(2)}$. The choice of these functions is dependent upon the physics of the problem [70]. In this study, Hankel function of first kind are adopted to represent the outgoing circular-crested waves.

4.3.1.3 Hybrid method to compute Green's functions

To compute the dynamic response of a plate to a vertical point load applied at $(0, 0, z_0)$ (Green's functions) the hybrid method, presented in Chapter 3 to analyze the plane strain problem, is adopted and extended. It is noted that the axisymmetric condition about z-axis holds for the present situation. As illustrated in Figure 4.2, the plate is divided into exterior and interior regions by a cylindrical surface with radius r_0.

Wave function expansion for exterior region

In the exterior region R, the plate is divided into a number of sublayers to evaluate the wave functions according to equations (4.10) and (4.11). The displacement field is represented by the modal sum of a finite number (M) of modes in the form as

$$\begin{aligned} u &= \sum_{m=1}^{M} A_m U_m H_1^{(1)}(k_m r) \\ w &= \sum_{m=1}^{M} A_m W_m H_0^{(1)}(k_m r) \end{aligned} \tag{4.19}$$

where A_m is the amplitude of the m-th mode. Equation (4.19) gives the displacements at boundary nodes as

$$\mathbf{q}_B = \mathbf{G}\mathbf{\Lambda} \tag{4.20}$$

where the subscript B represents boundary, and

$$\mathbf{G} = [\,\mathbf{q}_1 \quad \mathbf{q}_2 \quad \cdots\cdots \quad \mathbf{q}_m \cdots\cdots \quad \mathbf{q}_M\,] \tag{4.21}$$

$$\mathbf{q}_m^{\mathrm{T}} = \langle\, U_{1m}, \quad W_{1m} \quad ..., \quad U_{im}, \quad W_{im}, ..., \quad U_{(N+1)m}, \quad W_{(N+1)m} \quad \rangle\,. \tag{4.22}$$

$$\mathbf{\Lambda}^{\mathrm{T}} = \langle\, A_1 H_1^{(1)}(k_m r_0), \quad A_1 H_0^{(1)}(k_m r_0), \quad \cdots \quad A_M H_1^{(1)}(k_M r_0), \quad A_M H_0^{(1)}(k_M r_0)\,\rangle \tag{4.23}$$

The nodal force vector at the boundary nodes can be formed as

$$\mathbf{P}_B = \mathbf{F}\mathbf{\Lambda}, \tag{4.24}$$

where

$$\mathbf{F} = [\,\mathbf{f}_1 \quad \mathbf{f}_2 \quad \cdots\cdots \quad \mathbf{f}_m \cdots\cdots \quad \mathbf{f}_M\,] \tag{4.25}$$

The force shape mode vector $\mathbf{f}_i$ is formed by the consistent load vector formulation.

Finite element model of interior region

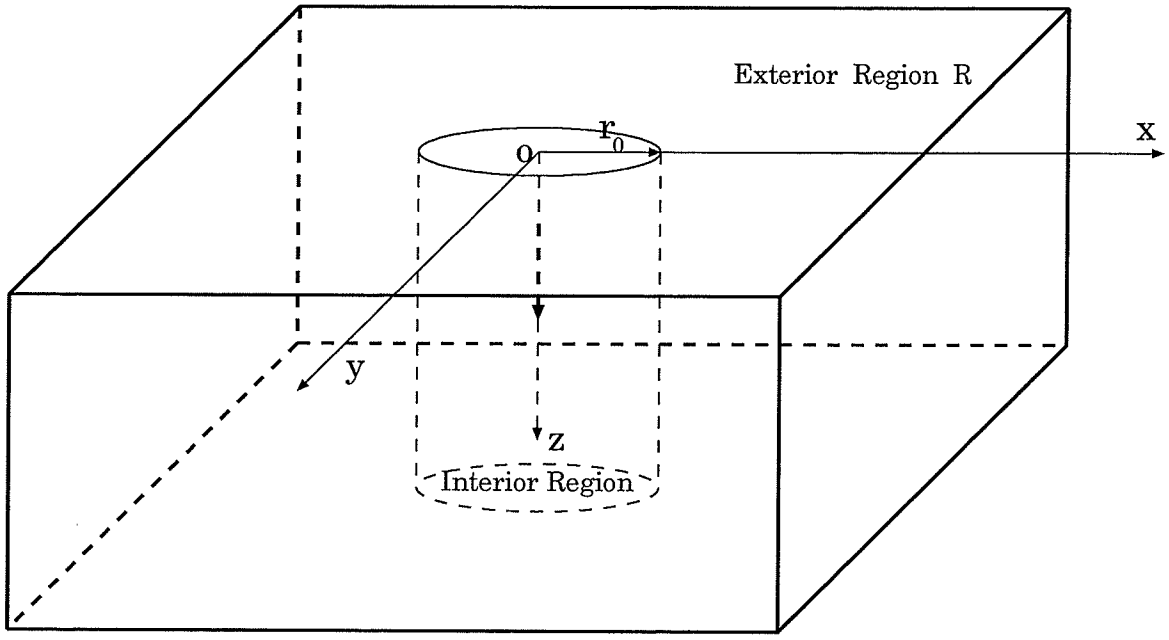

Figure 4.2: Divided regions of an isotropic plate

The interior region is modelled by axisymmetric finite elements. Following the conventional assembly process in the finite element method, minimizing the energy functional, we obtain:

$$\delta\hat{\pi} = \delta\bar{\mathbf{q}}_T^T \mathbf{S}\mathbf{q}_T - \delta\bar{\mathbf{q}}_T^T \mathbf{P}_T = 0. \tag{4.26}$$

where

$$\mathbf{q}_T^T = \langle\, \mathbf{q}_I{}^T \quad \mathbf{q}_B{}^T \,\rangle; \quad \mathbf{P}_T^T = \langle\, \mathbf{P}_I{}^T \quad \mathbf{P}_B{}^T \,\rangle \tag{4.27}$$

$$\mathbf{S} = \mathbf{K}_T - \omega^2 \mathbf{M}_T = \begin{bmatrix} \mathbf{S}_{II} & \mathbf{S}_{IB} \\ \mathbf{S}_{BI} & \mathbf{S}_{BB} \end{bmatrix}. \tag{4.28}$$

In the above, $\mathbf{q}_I$ and $\mathbf{P}_I$ are the nodal displacement and force vectors corresponding to interior nodes; $\mathbf{q}_B$ and $\mathbf{P}_B$ represent those vectors corresponding to boundary nodes; and $\mathbf{K}_T$ and $\mathbf{M}_T$ are, respectively, the global stiffness and mass matrices of the interior region. The stiffness and mass matrices for each element are defined as

$$\mathbf{k}^e = 2\pi \int_{A^e} \mathbf{B}^T \mathbf{D}\mathbf{B} r dr dz$$

$$\mathbf{m}^e = 2\pi \int_{A^e} \rho \mathbf{N}^{\mathrm{T}} \mathbf{N} r dr dz \tag{4.29}$$

where $\mathbf{N}$ is the shape function matrix, and

$$\mathbf{B} = \mathbf{L}\mathbf{N} \tag{4.30}$$

Global solution

The global solution is obtained by imposing the continuity conditions of displacements and tractions on the boundary nodes. Following the similar procedure as illustrated in Chapter 3, imposing the conditions

$$\mathbf{q}_{\mathrm{B}}^{\mathrm{in}} = 0; \quad \mathbf{P}_{\mathrm{B}}^{\mathrm{in}} = 0 \tag{4.31}$$

due to the fact that there is no load applied in the exterior region, we obtain:

$$\bar{\mathbf{G}}^{\mathrm{T}}(\mathbf{S}_{\mathrm{BB}}^{*}\mathbf{G} - \mathbf{F})\mathbf{\Lambda} = -\bar{\mathbf{G}}^{\mathrm{T}}\mathbf{S}_{\mathrm{BI}}\mathbf{S}_{\mathrm{II}}\mathbf{P}_{\mathbf{I}} \tag{4.32}$$

where

$$\mathbf{S}_{\mathrm{BB}}^{*} = \mathbf{S}_{\mathrm{BB}} - \mathbf{S}_{\mathrm{BI}}\mathbf{S}_{\mathrm{II}}^{-1}\mathbf{S}_{\mathrm{IB}}, \tag{4.33}$$

Write $\mathbf{\Lambda}$ known, the amplitude A_m is determined by equation (4.23), and Green's function due to the vertical load can be computed by equation (4.19).

4.3.2 General formulation

The three-dimensional waves generated by arbitrary point load in an isotropic plate is studied in this subsection. A decomposition technique is established. The Green's functions for the plate is obtained.

4.3.2.1 Decomposition of the problem

The time-harmonic three-dimensional wave motion equation for an isotropic plate can be written in (x, y, z) coordinate system as

$$\mu\nabla^2\mathbf{u} + (\lambda+\mu)\nabla(\nabla\cdot\mathbf{u}) + \mathbf{b} + \rho\omega^2\mathbf{u} = 0 \tag{4.34}$$

where

$$\nabla^2 = \frac{\partial^2}{\partial x^2} + \frac{\partial^2}{\partial y^2} + \frac{\partial^2}{\partial z^2} \tag{4.35}$$

$$\mathbf{u}^{\mathrm{T}} = \langle\, u \quad v \quad w \,\rangle\,; \qquad \mathbf{b}^{\mathrm{T}} = \langle\, b_x \quad b_y \quad b_z \,\rangle \tag{4.36}$$

u, v and w represent displacements, b_x, b_y and b_z represent body forces, in the x, y and z directions, respectively.

The double integral Fourier transform pair with respect to x and y are

$$\tilde{f}(\xi,\eta,z) = \int_{-\infty}^{\infty}\int_{-\infty}^{\infty} f(x,y,z)e^{-j\xi x - j\eta y}dxdy \tag{4.37}$$

$$f(x,y,z) = \frac{1}{(2\pi)^2}\int_{-\infty}^{\infty}\int_{-\infty}^{\infty} \tilde{f}(\xi,\eta,z)e^{j\xi x + j\eta y}d\xi d\eta \tag{4.38}$$

where parameters ξ and η represent wavenumbers in x and y directions. The application of (4.37) to (4.34) leads to:

$$\mathbf{A}_1\frac{\mathrm{d}^2\tilde{\mathbf{u}}}{\mathrm{d}z^2} - j\mathbf{A}_2\frac{\mathrm{d}\tilde{\mathbf{u}}}{\mathrm{d}z} - \mathbf{A}_3\tilde{\mathbf{u}} + \tilde{\mathbf{b}} + \rho\omega^2\tilde{\mathbf{u}} = 0 \tag{4.39}$$

where $\tilde{\mathbf{u}}$ and $\tilde{\mathbf{b}}$ are Fourier transforms of $\mathbf{u}$ and $\mathbf{b}$, respectively, and

$$\mathbf{A_1} = \begin{bmatrix} \mu & 0 & 0 \\ 0 & \mu & 0 \\ 0 & 0 & (\lambda+2\mu) \end{bmatrix}; \quad \mathbf{A_2} = (\lambda+\mu)\begin{bmatrix} 0 & 0 & \xi \\ 0 & 0 & \eta \\ \xi & \eta & 0 \end{bmatrix}$$

$$\mathbf{A_3} = \begin{bmatrix} (\lambda+2\mu)\xi^2+\mu\eta^2 & (\lambda+\mu)\xi\eta & 0 \\ (\lambda+\mu)\xi\eta & (\lambda+2\mu)\eta^2+\mu\xi^2 & 0 \\ 0 & 0 & \mu(\xi^2+\eta^2) \end{bmatrix}. \tag{4.40}$$

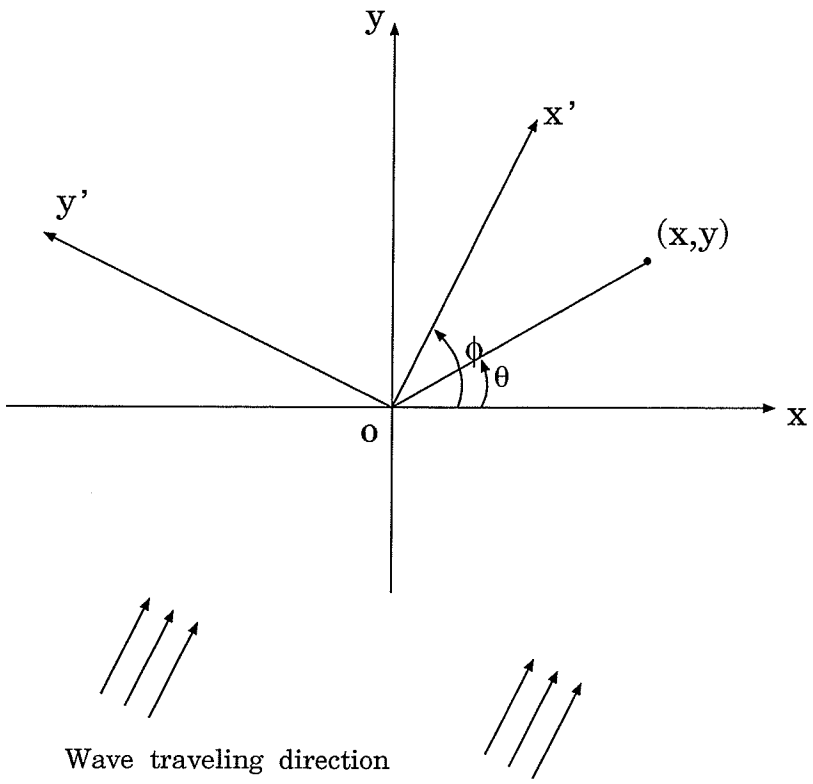

Figure 4.3: Coordinate systems and wave traveling direction

Define k as the wavenumber in a direction x' which has an angle ϕ with x axis (shown in Figure 4.3), then

$$\xi = kcos\phi, \quad \eta = ksin\phi \tag{4.41}$$

The displacement and body force vectors in the (x', y', z) coordinate system are obtained as

$$\begin{aligned} \hat{\tilde{\mathbf{u}}} &= \langle \hat{\tilde{u}} \quad \hat{\tilde{v}} \quad \hat{\tilde{w}} \rangle^{\mathrm{T}} = \mathbf{T}\tilde{\mathbf{u}} \\ \hat{\tilde{\mathbf{b}}} &= \langle \hat{\tilde{b}}_{x'} \quad \hat{\tilde{b}}_{y'} \quad \hat{\tilde{b}}_{z} \rangle^{\mathrm{T}} = \mathbf{T}\tilde{\mathbf{b}} \end{aligned} \tag{4.42}$$

where

$$\mathbf{T} = \begin{bmatrix} cos\phi & sin\phi & 0 \\ -sin\phi & cos\phi & 0 \\ 0 & 0 & 1 \end{bmatrix} \tag{4.43}$$

The wave motion equation in (x', y', z) coordinate system is derived as (noticing $\mathbf{T}^{-1} = \mathbf{T}^{\mathrm{T}}$):

$$\mathbf{A}_1\mathbf{T}^{\mathrm{T}}\frac{\mathrm{d}^2\hat{\tilde{\mathbf{u}}}}{\mathrm{d}z^2} - j\mathbf{A}_2\mathbf{T}^{\mathrm{T}}\frac{\mathrm{d}\hat{\tilde{\mathbf{u}}}}{\mathrm{d}z} - \mathbf{A}_3\mathbf{T}^{\mathrm{T}}\hat{\tilde{\mathbf{u}}} + \mathbf{T}^{\mathrm{T}}\hat{\tilde{\mathbf{b}}} + \rho\omega^2\mathbf{T}^{\mathrm{T}}\hat{\tilde{\mathbf{u}}} = 0 \tag{4.44}$$

Multiplying the above equation with $\mathbf{T}$ gives:

$$\hat{\mathbf{A}}_1\frac{\mathrm{d}^2\hat{\tilde{\mathbf{u}}}}{\mathrm{d}z^2} - j\hat{\mathbf{A}}_2\frac{\mathrm{d}\hat{\tilde{\mathbf{u}}}}{\mathrm{d}z} - \hat{\mathbf{A}}_3\hat{\tilde{\mathbf{u}}} + \hat{\tilde{\mathbf{b}}} + \rho\omega^2\hat{\tilde{\mathbf{u}}} = 0 \tag{4.45}$$

where

$$\begin{aligned}
\hat{\mathbf{A}}_1 &= \mathbf{T}\mathbf{A}_1\mathbf{T}^{\mathrm{T}} = \begin{bmatrix} \mu & 0 & 0 \\ 0 & \mu & 0 \\ 0 & 0 & (\lambda+2\mu) \end{bmatrix}, \\
\hat{\mathbf{A}}_2 &= \mathbf{T}\mathbf{A}_2\mathbf{T}^{\mathrm{T}} = (\lambda+\mu)\begin{bmatrix} 0 & 0 & k \\ 0 & 0 & 0 \\ k & 0 & 0 \end{bmatrix}, \\
\hat{\mathbf{A}}_3 &= \mathbf{T}\mathbf{A}_3\mathbf{T}^{\mathrm{T}} = k^2\begin{bmatrix} (\lambda+2\mu) & 0 & 0 \\ 0 & \mu & 0 \\ 0 & 0 & \mu \end{bmatrix}.
\end{aligned} \tag{4.46, 4.47}$$

Equation (4.45) can be expanded as

$$\mu\frac{\mathrm{d}^2\hat{\tilde{u}}}{\mathrm{d}z^2} - (\lambda+2\mu)k^2\hat{\tilde{u}} - j(\lambda+\mu)k\frac{\mathrm{d}\hat{\tilde{w}}}{\mathrm{d}z} + \hat{\tilde{b}}_{x'} + \rho\omega^2\hat{\tilde{u}} = 0 \tag{4.48}$$

$$(\lambda+2\mu)\frac{\mathrm{d}^2\hat{\tilde{w}}}{\mathrm{d}z^2} - \mu k^2\hat{\tilde{w}} - j(\lambda+\mu)k\frac{\mathrm{d}\hat{\tilde{u}}}{\mathrm{d}z} + \hat{\tilde{b}}_z + \rho\omega^2\hat{\tilde{w}} = 0 \tag{4.49}$$

$$\mu\frac{\mathrm{d}^2\hat{\tilde{v}}}{\mathrm{d}z^2} - \mu k^2\hat{\tilde{v}} + \hat{\tilde{b}}_{y'} + \rho\omega^2\hat{\tilde{v}} = 0 \tag{4.50}$$

Equations (4.48) and (4.49) represent a plane-strain problem while equation (4.50) represents an antiplane problem with waves travelling in x' direction. The wave fields (displacements, stresses) are independent of y' coordinate. It is concluded that three-dimensional wave propagation in an isotropic plate can be decomposed into plane-strain and antiplane problems. It is a very important characteristic since we have investigated plane-strain problem. The analysis of antiplane problem is analogous to and even simpler than the plane-strain analysis.

4.3.2.2 Green's functions

A point load applied at $(0, 0, z_0)$ can be expressed as

$$\mathbf{f} = \mathbf{f}_0 \delta(x)\delta(y) \tag{4.51}$$

where

$$\mathbf{f_0}^{\mathrm{T}} = \langle\, f_x \quad f_y \quad f_z \,\rangle \tag{4.52}$$

represents the amplitude of the load in x, y and z directions. Application of Fourier transform gives

$$\tilde{\mathbf{f}} = \int_{-\infty}^{\infty}\int_{-\infty}^{\infty} \mathbf{f}_0 \delta(x)\delta(y) e^{-j(\xi x+\eta y)} dxdy = \mathbf{f}_0 \tag{4.53}$$

In (x', y', z) coordinate system the load is obtained as

$$\hat{\tilde{\mathbf{f}}} = \begin{Bmatrix} \hat{\tilde{f}}_{x'} \\ \hat{\tilde{f}}_{y'} \\ \hat{\tilde{f}}_{z} \end{Bmatrix} = \mathbf{T}\tilde{\mathbf{f}} \;=\; \begin{Bmatrix} f_x cos\phi + f_y sin\phi \\ -f_x sin\phi + f_y cos\phi \\ f_z \end{Bmatrix} \tag{4.54}$$

Following the procedure for the analysis of plane-strain problem, the displacement vector $< \hat{\tilde{u}} \quad \hat{\tilde{w}} >^{\mathrm{T}}$ can be obtained in a modal summation form as (refer to equation (2.80)):

$$\begin{Bmatrix} \hat{\tilde{u}} \\ \hat{\tilde{w}} \end{Bmatrix} = \sum_{m=1}^{2M_p} \frac{\mathbf{\Phi}^L_{m2} \hat{\tilde{\mathbf{F}}}_{x'z}}{(k_m - k)B_m} \begin{Bmatrix} U_m \\ W_m \end{Bmatrix} \tag{4.55}$$

where M_p represents the number of modes of plane strain waves travelling in x' direction; U_m and W_m are the plane-strain modal displacements in x' and z directions, respectively; $\mathbf{\Phi}^{\mathrm{L}}_{m2}$ is part of the left eigenvector $\mathbf{\Phi}^{\mathrm{L}}_{m}$; B_m is the orthogonality coefficient; and $\tilde{\mathbf{F}}_{x'z}$ is the external force vector in the transformed domain as

$$\hat{\tilde{\mathbf{F}}}_{x'z} = \langle 0, \quad 0, \cdots \quad \hat{\tilde{f}}_{x'}, \quad \hat{\tilde{f}}_{z}, \quad 0, \quad \cdots \quad 0 \rangle^{\mathrm{T}}. \tag{4.56}$$

Similarly, the displacement $\hat{\tilde{v}}$ corresponding to the antiplane problem can be obtained as

$$\hat{\tilde{v}} = \sum_{m=1}^{2M_a} \frac{\mathbf{\Phi}^{L}_{m2} \hat{\tilde{\mathbf{F}}}_{y'}}{(k_m - k)B_m} V_m \tag{4.57}$$

where M_a represents the number of modes of antiplane waves travelling in x' direction; V_m is the antiplane modal displacement in y' direction; and

$$\hat{\tilde{\mathbf{F}}}_{y'} = \langle 0, \quad 0, \cdots \quad \hat{\tilde{f}}_{y'}, \quad 0, \quad \cdots \quad 0 \rangle^{\mathrm{T}}. \tag{4.58}$$

<u>z-direction load</u>

A z-direction unit load ($f_z = 1$) applied at $(0, 0, z_0)$ gives

$$\mathbf{\Phi}^{L}_{m2} \hat{\tilde{\mathbf{F}}}_{x'z} = \psi_3; \qquad \mathbf{\Phi}^{L}_{m2} \hat{\tilde{\mathbf{F}}}_{y'} = 0 \tag{4.59}$$

where ψ_3 is the corresponding element in the vector $\mathbf{\Phi}^{\mathrm{L}}_{\mathrm{m2}}$. It is seen that the displacements due to the antiplane problem are zero.

The displacements in the transformed domain can be written in the (r, θ, z) coordinate (refer to Figure 4.3) as

$$\begin{Bmatrix} \tilde{u}_r \\ \tilde{u}_\theta \\ \tilde{w} \end{Bmatrix} = \sum_{m=1}^{2M_p} \frac{\psi_3}{(k_m - k)B_m} \begin{Bmatrix} U_m cos(\phi - \theta) \\ U_m sin(\phi - \theta) \\ W_m \end{Bmatrix} \tag{4.60}$$

Application of the inverse Fourier transform to equation (4.60) leads to [71]:

$$\begin{Bmatrix} u_r \\ u_\theta \\ w \end{Bmatrix} = \frac{1}{(2\pi)^2}\int\int_{(k,\phi)} \begin{Bmatrix} \tilde{u}_r \\ \tilde{u}_\theta \\ \tilde{w} \end{Bmatrix} e^{jkrcos(\phi-\theta)} k\mathrm{d}k\mathrm{d}\phi$$

$$= \frac{1}{(2\pi)^2}\int\int_{(k,\phi)} \sum_{m=1}^{2M_p} \frac{\psi_3 k}{(k_m-k)B_m} \begin{Bmatrix} U_m cos(\phi-\theta) \\ U_m sin(\phi-\theta) \\ W_m \end{Bmatrix} e^{jkrcos(\phi-\theta)}\mathrm{d}k\mathrm{d}\phi$$

$$= -\frac{1}{(2\pi)^2}\int\int_{(k,\phi)} \sum_{m=1}^{2M_p} \frac{\psi_3}{B_m}(1+\frac{k_m}{k-k_m}) \begin{Bmatrix} U_m cos(\phi-\theta) \\ U_m sin(\phi-\theta) \\ W_m \end{Bmatrix} e^{jkrcos(\phi-\theta)}\mathrm{d}k\mathrm{d}\phi \tag{4.61}$$

where

$$x = rcos\theta; \qquad y = rsin\theta \tag{4.62}$$

As stated in Chapter 2, only half of the $2M_p$ modes correspond to the waves propagating away from the source toward field points are of interest. Let

$$-\frac{\pi}{2} \le \varphi = \phi - \theta \le \frac{\pi}{2} \tag{4.63}$$

we obtain:

$$\begin{Bmatrix} u_r \\ u_\theta \\ w \end{Bmatrix} = -\frac{1}{(2\pi)^2}\int_{-\pi/2}^{\pi/2}\int_{-\infty}^{\infty} \sum_{m=1}^{M_p} \frac{\psi_3}{B_m}(1+\frac{k_m}{k-k_m}) \begin{Bmatrix} U_m cos\varphi \\ U_m sin\varphi \\ W_m \end{Bmatrix} e^{jkrcos\varphi}\mathrm{d}k\mathrm{d}\varphi$$

$$= -\frac{1}{(2\pi)^2}\int_{-\pi/2}^{\pi/2} \sum_{m=1}^{M_p} \frac{\psi_3}{B_m}\Big(\int_{-\infty}^{\infty} e^{jkrcos\varphi}\mathrm{d}k + \int_{-\infty}^{\infty} \frac{k_m}{k-k_m} e^{jkrcos\varphi}\mathrm{d}k\Big) \begin{Bmatrix} U_m cos\varphi \\ U_m sin\varphi \\ W_m \end{Bmatrix} \mathrm{d}\varphi \tag{4.64}$$

Employing the definition of Delta function

$$\int_{-\infty}^{\infty} e^{jkrcos\varphi}\mathrm{d}k = 2\pi\delta(rcos\varphi) \tag{4.65}$$

and applying Cauchy residue theorem to the last integral in (4.64) leads to:

$$\left\{\begin{array}{c} u_r \\ u_\theta \\ w \end{array}\right\} = -\frac{1}{(2\pi)} \sum_{m=1}^{M_p} \frac{\psi_3}{B_m} \left(\int_{-\pi/2}^{\pi/2} [\delta(r cos\varphi) + j k_m e^{j k_m r cos\varphi}] \left\{\begin{array}{c} U_m cos\varphi \\ U_m sin\varphi \\ W_m \end{array}\right\} \mathrm{d}\varphi \right. \quad (4.66)$$

In the derivation of equation (4.66) the isotropic material property, *i.e.* the eigenvalues and eigenvectors are independent of ϕ, is incorporated. Following expressions are obtained from the properties of δ function [72],

$$\begin{aligned} \int_{-\pi/2}^{\pi/2} \delta(r cos\varphi) \mathrm{d}\varphi &= -\frac{2}{r} \\ \int_{-\pi/2}^{\pi/2} \delta(r cos\varphi) cos\varphi \mathrm{d}\varphi &= 0 \\ \int_{-\pi/2}^{\pi/2} \delta(r cos\varphi) sin\varphi \mathrm{d}\varphi &= 0 \end{aligned} \quad (4.67)$$

The displacements are expressed as

$$\left\{\begin{array}{c} u_r \\ w \end{array}\right\} = \frac{1}{2} \sum_{m=1}^{M_p} \frac{\psi_3}{B_m} \left\{\begin{array}{c} k_m \hat{H}_1(k_m r) U_m \\ [\frac{2}{\pi r} - j k_m \hat{H}_0(k_m r)] W_m \end{array}\right\} \quad (4.68)$$

where

$$\hat{H}_n(kr) = \frac{e^{-n\pi/2}}{\pi} \int_{-\pi/2}^{\pi/2} e^{j k_m r cos\varphi + jn\varphi} \mathrm{d}\varphi \quad (4.69)$$

and

$$u_\theta = 0$$

since

$$\int_{-\pi/2}^{\pi/2} sin\varphi e^{jkr cos\varphi} \mathrm{d}\varphi = 0 \quad (4.70)$$

It may be noted that $\hat{H}_n$ are not Hankel functions.

<u>x-direction load</u>

A x-direction unit load ($f_x = 1$) applied at $(0, 0, z_0)$ gives

$$\mathbf{\Phi}^L_{m2}\hat{\tilde{\mathbf{F}}}_{x'z} = \psi_1 cos\phi; \qquad \mathbf{\Phi}^L_{m2}\hat{\tilde{\mathbf{F}}}_{y'} = -\psi_2 sin\phi \tag{4.71}$$

where ψ_1 and ψ_2 are the corresponding elements in $\mathbf{\Phi}^L_{m2}$. The displacements in (r, θ, z) coordinate system are obtained as

$$\begin{Bmatrix} \tilde{u}_r \\ \tilde{u}_\theta \\ \tilde{w} \end{Bmatrix} = \sum_{m=1}^{2M_p} \frac{\psi_1}{(k_m - k)B_m} \begin{Bmatrix} U_m cos\phi cos(\phi - \theta) \\ U_m cos\phi sin(\phi - \theta) \\ W_m cos\phi \end{Bmatrix} - \sum_{m=1}^{2M_a} \frac{\psi_2}{(k_m - k)B_m} \begin{Bmatrix} V_m sin\phi sin(\phi - \theta) \\ V_m sin\phi cos(\phi - \theta) \\ 0 \end{Bmatrix} \tag{4.72}$$

Through the similar manipulations as used in deriving the Green's functions for z-direction load, we obtain:

$$\begin{Bmatrix} u_r \\ u_\theta \\ w \end{Bmatrix} = -\frac{1}{(2\pi)^2} \int_{-\pi/2}^{\pi/2} \int_{-\infty}^{\infty} [\sum_{m=1}^{M_p} \frac{\psi_1}{B_m}(1 + \frac{k_m}{k - k_m}) \begin{Bmatrix} U_m cos(\varphi + \theta) cos\varphi \\ U_m cos(\varphi + \theta) sin\varphi \\ W_m cos(\varphi + \theta) \end{Bmatrix} + \sum_{m=1}^{2M_a} \frac{\psi_2}{B_m}(1 + \frac{k_m}{k - k_m}) \begin{Bmatrix} V_m sin(\varphi + \theta) sin\varphi \\ -V_m sin(\varphi + \theta) cos\varphi \\ 0 \end{Bmatrix}] e^{jkrcos\varphi} \mathrm{d}\varphi \mathrm{d}k \tag{4.73}$$

Applications of Cauchy residue theorem and the expressions below

$$\begin{aligned} &\int_{-\pi/2}^{\pi/2} \delta(rcos\varphi) cos(\varphi + \theta) sin\varphi \mathrm{d}\varphi = \frac{2}{r} sin\theta \\ &\int_{-\pi/2}^{\pi/2} \delta(rcos\varphi) cos(\varphi + \theta) \mathrm{d}\varphi = 0 \\ &\int_{-\pi/2}^{\pi/2} \delta(rcos\varphi) sin(\varphi + \theta) \mathrm{d}\varphi = 0 \\ &\int_{-\pi/2}^{\pi/2} \delta(rsin\varphi) cos\varphi \mathrm{d}\varphi = 0 \end{aligned} \tag{4.74}$$

result in:

$$\begin{Bmatrix} u_r \\ u_\theta \\ w \end{Bmatrix} = -\frac{1}{2}[\sum_{m=1}^{M_p} \frac{\psi_1}{B_m} \begin{Bmatrix} \frac{jk_m}{2}(\hat{H}_0(k_m r) - \hat{H}_2(k_m r))cos\theta U_m \\ (\frac{2}{\pi r}sin\theta - \frac{jk_m}{2}(\hat{H}_0(k_m r) + \hat{H}_2(k_m r)))sin\theta U_m \\ k_m \hat{H}_0(k_m r)cos\theta W_m \end{Bmatrix} + \sum_{m_1}^{M_a} \frac{\psi_2}{B_m} \begin{Bmatrix} (-\frac{2}{\pi r} + \frac{jk_m}{2}(\hat{H}_0(k_m r) + \hat{H}_2(k_m r)))cos\theta V_m \\ -\frac{jk_m}{2}(\hat{H}_0(k_m r) - \hat{H}_2(k_m r))sin\theta V_m \\ 0 \end{Bmatrix}] \quad (4.75)$$

Similarly, the Green's functions due to y-direction load can be obtained by interchanging $sin\theta$ and $cos\theta$ and changing the sign of u_θ in equation (4.75). It is seen that based on the decomposition technique the Green's functions for an isotropic plate are obtained in modal summation forms.

4.3.2.3 Solutions in (x, y, z) coordinate system

For the applications of boundary element method, it is desirable to have Green's functions in (x, y, z) coordinate system.

1. x-direction load

$$\begin{Bmatrix} u \\ v \\ w \end{Bmatrix} = \frac{1}{2}\sum_{m=1}^{M_p} \frac{\psi_1}{B_m} \begin{Bmatrix} [\frac{2}{\pi r}sin^2\theta + \frac{jk_m}{2}(\hat{H}_2(k_m r)cos2\theta + \hat{H}_0(k_m r))]U_m \\ [-\frac{1}{\pi r} + \frac{jk_m}{2}\hat{H}_2(k_m r)]sin2\theta U_m \\ k_m \hat{H}_1(k_m r)cos\theta W_m \end{Bmatrix} + \frac{1}{2}\sum_{m=1}^{M_a} \frac{\psi_2}{B_m} \begin{Bmatrix} [\frac{2}{\pi r}cos^2\theta - \frac{jk_m}{2}(\hat{H}_2(k_m r)cos2\theta + \hat{H}_0(k_m r))]V_m \\ [\frac{1}{\pi r} - \frac{jk_m}{2}\hat{H}_2(k_m r)]sin2\theta V_m \\ 0 \end{Bmatrix} \quad (4.76)$$

2. y-direction load

$$\begin{Bmatrix} u \\ v \\ w \end{Bmatrix} = \frac{1}{2}\sum_{m=1}^{M_p} \frac{\psi_1}{B_m} \begin{Bmatrix} [-\frac{1}{\pi r} + \frac{jk_m}{2}\hat{H}_2(k_m r)]sin2\theta U_m \\ [\frac{2}{\pi r}cos^2\theta - \frac{jk_m}{2}(\hat{H}_2(k_m r)cos2\theta + \hat{H}_0(k_m r))]U_m \\ k_m \hat{H}_1(k_m r)sin\theta W_m \end{Bmatrix}$$

$$+ \quad \frac{1}{2}\sum_{m=1}^{M_a}\frac{\psi_2}{B_m}\begin{Bmatrix} [\frac{1}{\pi r}-\frac{jk_m}{2}\hat{H}_2(k_m r)]sin2\theta V_m \\ [\frac{2}{\pi r}sin^2\theta-\frac{jk_m}{2}(\hat{H}_0(k_m r)-\hat{H}_2(k_m r)cos2\theta]V_m \\ 0 \end{Bmatrix} \tag{4.77}$$

3. z direction load:

$$\begin{Bmatrix} u \\ v \\ w \end{Bmatrix} = \frac{1}{2}\sum_{m=1}^{M_p}\frac{\psi_3}{B_m}\begin{Bmatrix} k_m\hat{H}_1(k_m r)cos\theta U_m \\ k_m\hat{H}_1(k_m r)sin\theta U_m \\ [\frac{2}{\pi r}-j\hat{H}_0(k_m r)]W_m \end{Bmatrix} \tag{4.78}$$

Here u, v, and w are displacements in x, y, and z directions, respectively.

4.3.3 Numerical results for Green's functions

In this section, a numerical example of computing Green's functions for an isotropic plate is discussed. Two loading conditions are considered:

1. A vertical load acts at $(0, 0, 0.4H)$.

2. A horizontal load in x direction acts at the same location.

The Poisson's ratio ν is taken to be $1/3$. Two normalized frequencies, $\Omega = 1$ and $\Omega = 10$, are considered.

For the vertical load, the axisymmetric condition about z axis holds. The problem is analyzed by both the hybrid method and the decomposition based technique. In the hybrid modelling, the finite element mesh contains 20 quadratic elements and 85 nodes. The boundary is located at $r_0 = 0.2H$ (refer to Figure 4.2). Forty modes are taken in the wavefunction expansion in the exterior region.

Figures 4.4(a) and (b) show the vertical displacements through the thickness at sections $x = 0.3H$ and $x = 10H$, respectively, from the two methods at frequency

$\Omega = 1$; and Figure 4.5 shows the corresponding results at $\Omega = 10$. In these figures, Re refers to the real part of the complex displacement, Im refers to the imaginary part, and the decomposition based technique is referred as stiffness method. Figure 4.4 shows that at low frequencies $Im[w]$ is nearly a constant through the thickness at both near and far fields; and $Re[w]$ varies through the thickness in the near field and almost vanishes in the far field. At high frequencies, both the real and imaginary parts of the vertical displacements vary through thickness at near and far fields, as shown in Figure 4.5. It is noticed that the results from the two models are in very good agreement both in near and far fields, at low and high frequencies.

It is important to note that axisymmetric condition does not hold for a horizontal direction load. The hybrid method developed above for axisymmetric load cannot be applied to analyze this problem. The Green's functions due to the x direction load are computed by the decomposition based technique. A displacement reciprocity relation is applied to check the numerical results.

Figure 4.6(a) shows the vertical displacement w through the thickness at $x = 0.3H$ due to the x direction load at $\Omega = 1$. Also illustrated in this figure is the x direction displacement u at point $(0, 0, 0.4H)$ due to a vertical load acting at $(0.4H, 0, z)$, with z varying from 0 to $2H$. It is seen that the displacements from the two different load conditions are in excellent agreement. The displacement reciprocity relation is satisfied. Figure 4.6(b) represents the displacements from the two load conditions at far fields ($x = 10H$) at $\Omega = 1$. Results for both near ($x = 0.3H$) and far ($x = 10H$) fields at high frequency ($\Omega = 10$) are given in Figure 4.7 for the two load conditions. Very good agreements are observed from these figures. It is seen that the displacement reciprocity relation is satisfied for low as well as high frequencies.

4.4 BEM for 3-D wave scattering

The boundary element method is increasingly being explored as a feasible approach to solve diverse problems related to nondestructive evaluation technique [73, 74]. In this section, we develop a BEM capable of solving scattering from arbitrarily-shaped three dimensional flaws in an isotropic plate. The flaws may be either voids or cracks.

4.4.1 Formulation

The time-harmonic formulation (3.28) of boundary element method for elastodynamics has some features which make it particularly attractive for solving scattering problems. These features include rigorous treatment of radiation condition for an unbounded medium, reduction in the dimensionality of the problem, direct methods for calculating flaw-induced signals, and other instances of computational savings.

The boundary integral equation (3.28) is converted to algebraic equations (3.31) by discretizing the flaw surface into boundary elements. The actual surface geometry is then interpolated by polynomials over each element in terms of nodal coordinates. Each field variable is also represented by an interpolation of nodal quantities. Specifics of this procedure are given in Chapter 3.

The diagonal 3×3 block of the assembled $\mathbf{H}$ matrix contains the tensor c_{ij} as well as the CPV of the traction kernel integrals; also, the diagonal elements of the assembled $\mathbf{G}$ matrix contain the weakly singular displacement kernel integrals. An effective technique to handle these singular integrals is critical to the accuracy of the boundary element solution. The technique developed in Chapter 3 to evaluate singular integrals is extended to three dimensional analysis.

With the concept of artificial source, the boundary integral equations for a typical

boundary node I can be manipulated as:

$$\begin{aligned} h_{i,i}u_i &+ h_{i,i+1}u_{i+1} + h_{i,i+2}u_{i+2} - g_{i,i}t_i \\ &= \sum_{j\neq i,i+1,i+2}(-h_{i,j}u_j) + \sum_{j\neq i}(g_{i,j}t_j) + b_i \qquad (4.79) \\ h_{i+1,i}u_i &+ h_{i+1,i+1}u_{i+1} + h_{i+1,i+2}u_{i+2} - g_{i+1,i+1}t_{i+1} \\ &= \sum_{j\neq i,i+1,i+2}(-h_{i+1,j}u_j) + \sum_{j\neq i+1}(g_{i+1,j}t_j) + b_{i+1} \qquad (4.80) \\ h_{i+2,i}u_i &+ h_{i+2,i+1}u_{i+1} + h_{i+2,i+2}u_{i+2} - g_{i+2,i+2}t_{i+2} \\ &= \sum_{j\neq i,i+1,i+2}(-h_{i+2,j}u_j) + \sum_{j\neq i+2}(g_{i+2,j}t_j) + b_{i+2} \qquad (4.81) \end{aligned}$$

where u_j and t_j are displacement and traction Green's functions due to the artificial source; the diagonal 3×3 block elements of $\mathbf{H}$ ($h_{l,m}, l, m = 1, 2, 3$) and and diagonal elements of $\mathbf{G}$ ($g_{l,l}, l = 1, 2, 3$) are taken as unknowns; $h_{i,j}$ and $g_{i,j}$ at the right hand side are the known elements of the matrices $\mathbf{H}$ and $\mathbf{G}$, and contain only regular integrals. With the concept of artificial source we obtain three equations for the twelve unknowns. By choosing four independent artificial sources, we can establish sufficient number of linear algebraic equations to solve for the unknowns.

Voids are a common class of flaws in structural materials. Computationally, they are simpler to handle compared with cracks. For illustration purposes numerical results for only a crack problem are presented in this section.

4.4.2 Numerical results

The boundary element method is used to study the scattering of waves from a horizontal crack in an isotropic plate of thickness $2H$. The crack (shadowed part in Figure 4.8) has a rectangular profile with length H (along x direction), width $0.4H$ (along y direction), and zero thickness in z direction, respectively; and the crack center is located on the z axis. The crack depth is assumed to be $H/4$. The vertical load is

applied on the top surface at point $(-3.5H, 0, 0)$. The Poisson's ratio, ν, is taken as 1/3. To model the crack tip area quarter-point 8-node quadrilateral elements, as shown in Figure 4.9, are used.

In the boundary element analysis, to circumvent the difficulties associated with the presence of the crack, the multidomain technique (refer to Chapter 3) is employed. The plate is divided into two domains by four vertical fictitious boundary surfaces (as shown in Figure 4.8). The boundary element mesh is composed of 152 quadratic elements and 462 nodes.

Observation points are set in a rectangular area on the top surface above the crack with length $1.5H$ and width $0.6H$. Vertical displacements of the observation points are shown in Figure 4.10 for normalized frequency $\Omega = 1$. It is noted that only half of the observation area is shown in Figure 4.10 since the system is symmetric about x axis. Relatively even distribution of displacements is observed in the absence of crack from Figure 4.10(a). The displacement distribution of the observation points above the crack is significantly changed due to the presence of the crack, as shown in Figure 4.10(b). Specifically, the surface response shows a peak in the central area above the crack, and the response of the surface points outside the crack region almost keeps unchanged.

For comparision, the same problem is solved making plane-strain assumption. The results for vertical displacements are presented in Figure 4.11. The solid line represents the amplitudes of vertical displacements of top surface in the absence of crack, while the dashed line represents the results in the presence of crack. It is seen that the results from plane-strain modelling is much larger that that from three-dimensional modelling.

4.5 Concluding remarks

Three-dimensional wave propagation in isotropic plates is investigated by two models. In the first model, the analytical formulations for frequency equation and wave functions are derived for circular-crested waves which are generated by a vertical load (axisymmetric problem); a hybrid method combining finite element modelling and wave modal representation is established to compute the dynamic response of the plate. The second model is developed based on the decomposition of the three-dimensional wave problem into a series of plane-strain and antiplane problems. The Rayleigh-Ritz type approximation based stiffness method and modal summation technique are employed to construct the Green's functions in explicit forms.

A boundary element technique is exploited to analyze three-dimensional wave scattering by cracks in isotropic plates. The technique based on the concept of artificial source for the evaluation of singular integrals arising from boundary integral equations is extended to three-dimensional analysis. Numerical results show that the presence of cracks significantly modifies the surface response of the plate.

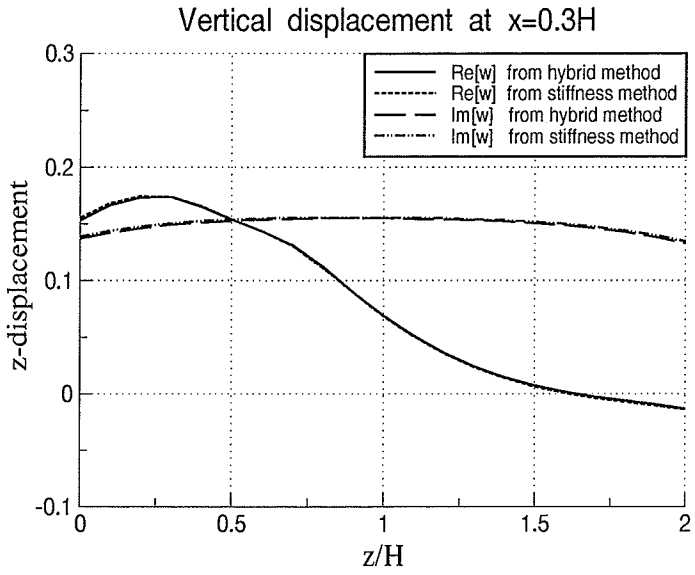

(a)

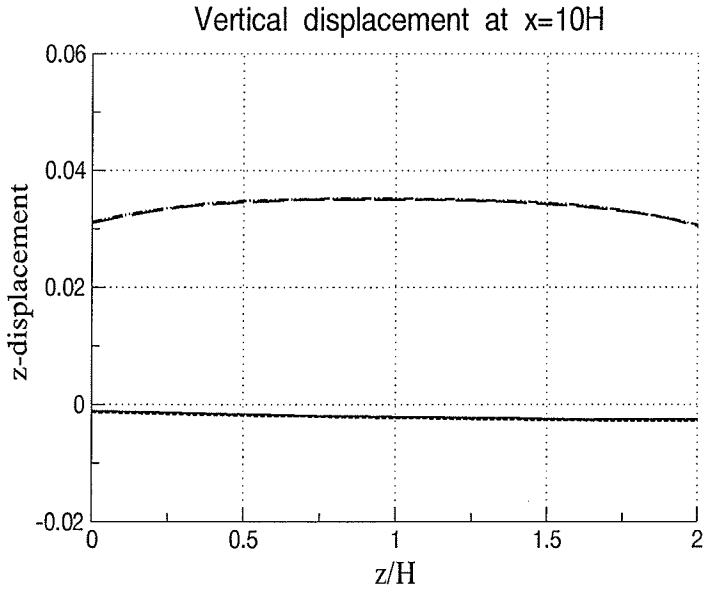

(b)

Figure 4.4: Vertical displacements through thickness, $\Omega = 1$, (a) $x = 0.3H$, (b) $x = 10H$.

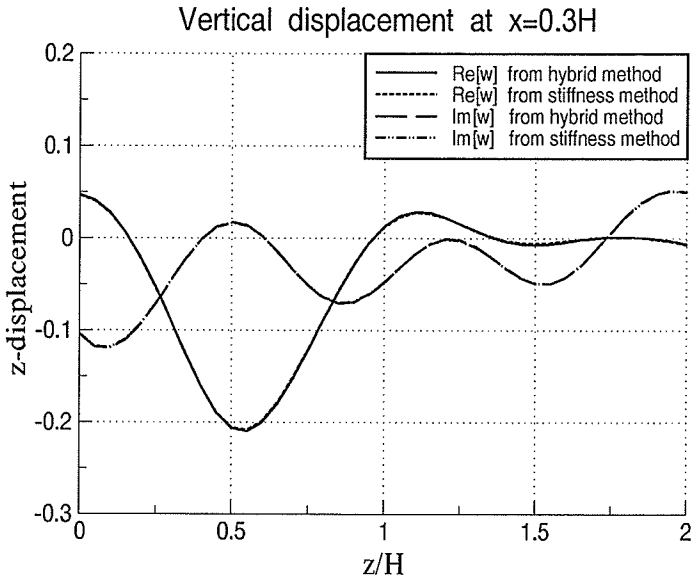

(a)

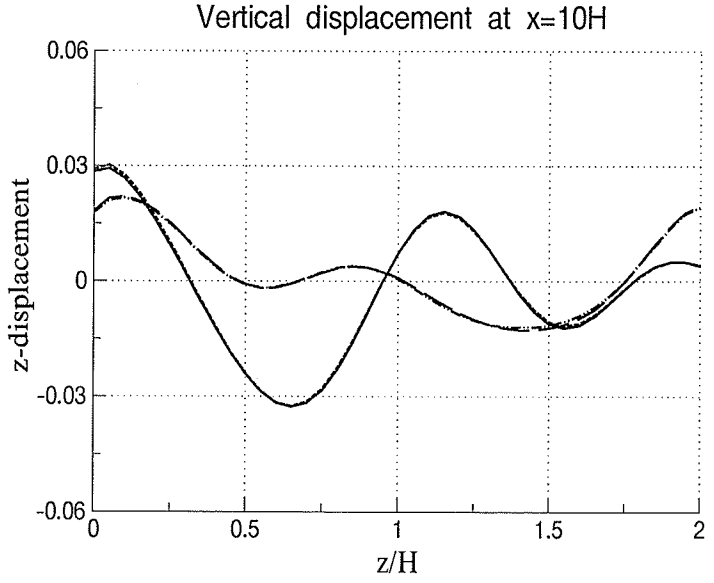

(b)

Figure 4.5: Vertical displacements through thickness, $\Omega = 10$, (a) $x = 0.3H$, (b) $x = 10H$.

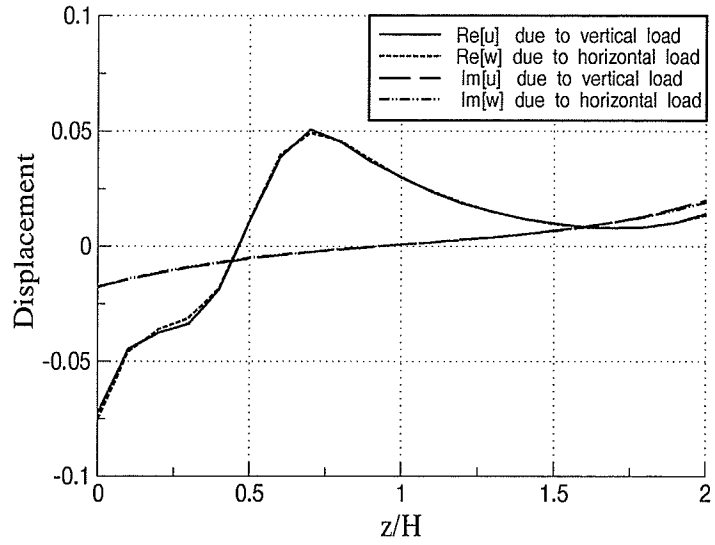

(a)

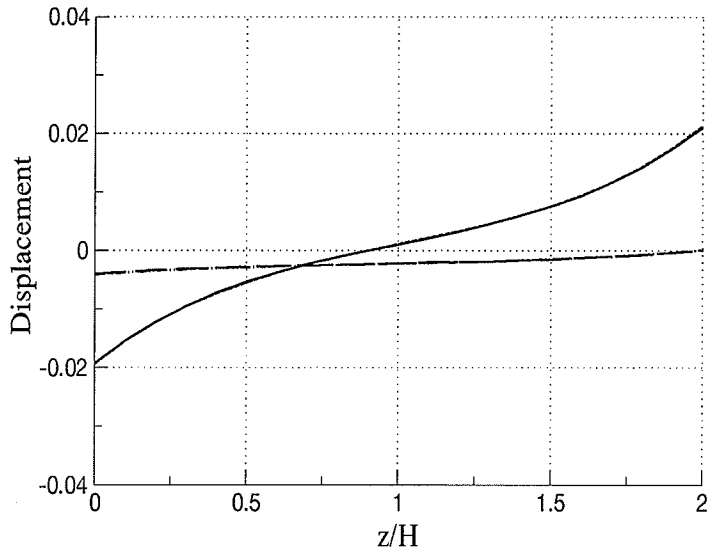

(b)

Figure 4.6: Displacements through thickness, $\Omega = 1$, (a) $x = 0.3H$, (b) $x = 10H$.

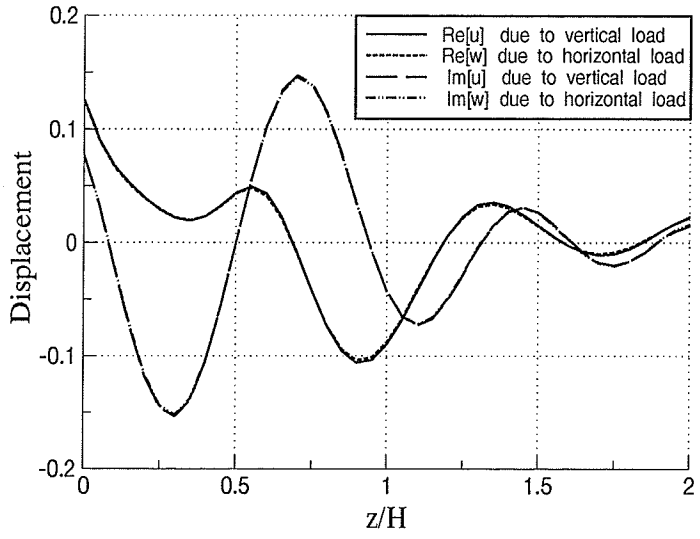

(a)

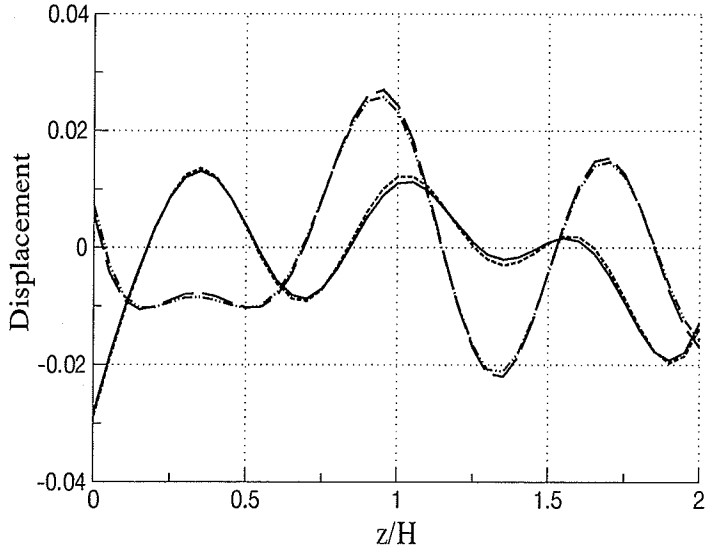

(b)

Figure 4.7: Displacements through thickness, $\Omega = 10$, (a) $x = 0.3H$, (b) $x = 10H$.

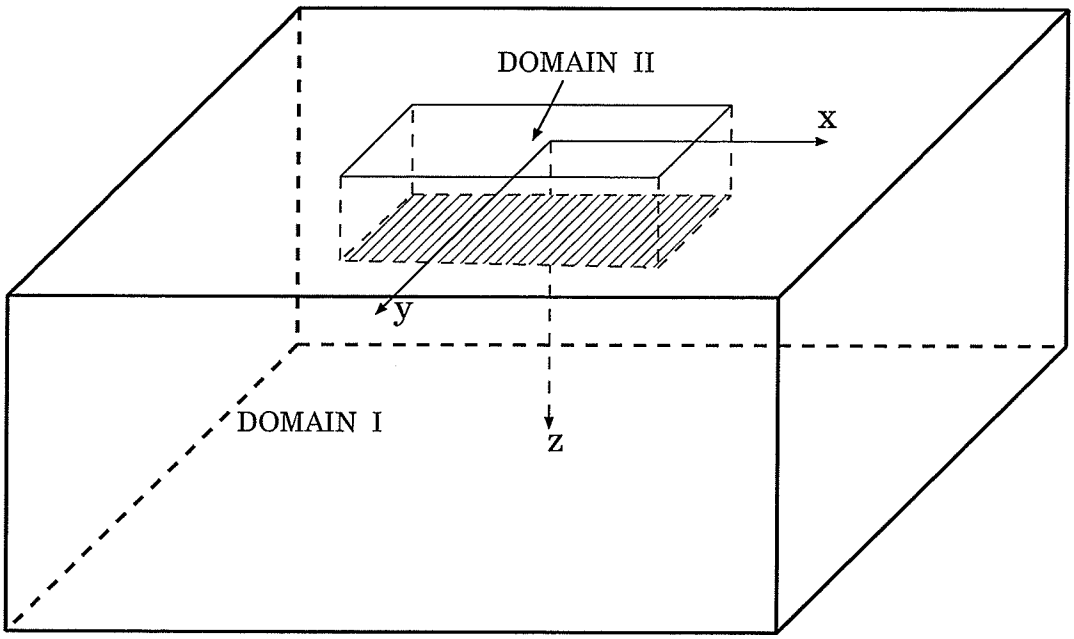

Figure 4.8: Configuration of a rectangular crack

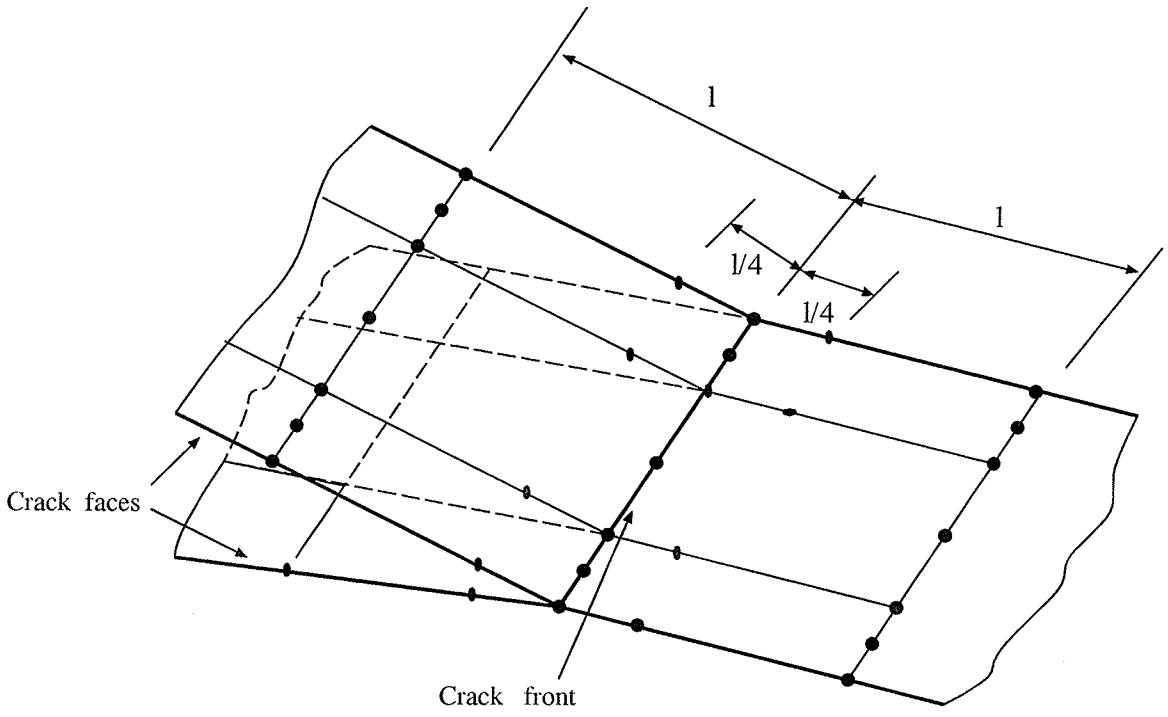

Figure 4.9: Crack-tip elements in 3-D analysis

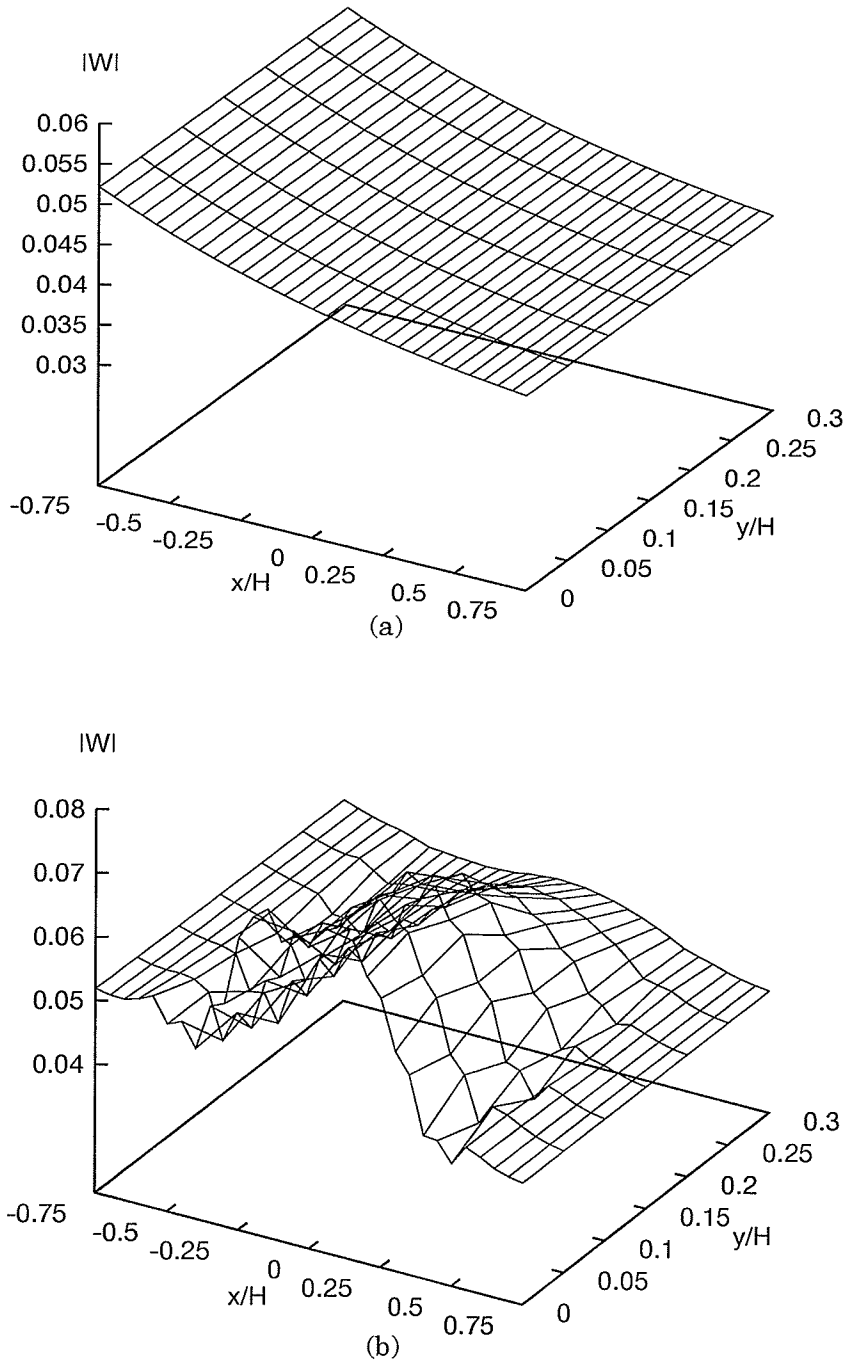

Figure 4.10: Vertical displacement on the top surface at $\Omega = 1$. (a) without crack, (b) with crack.

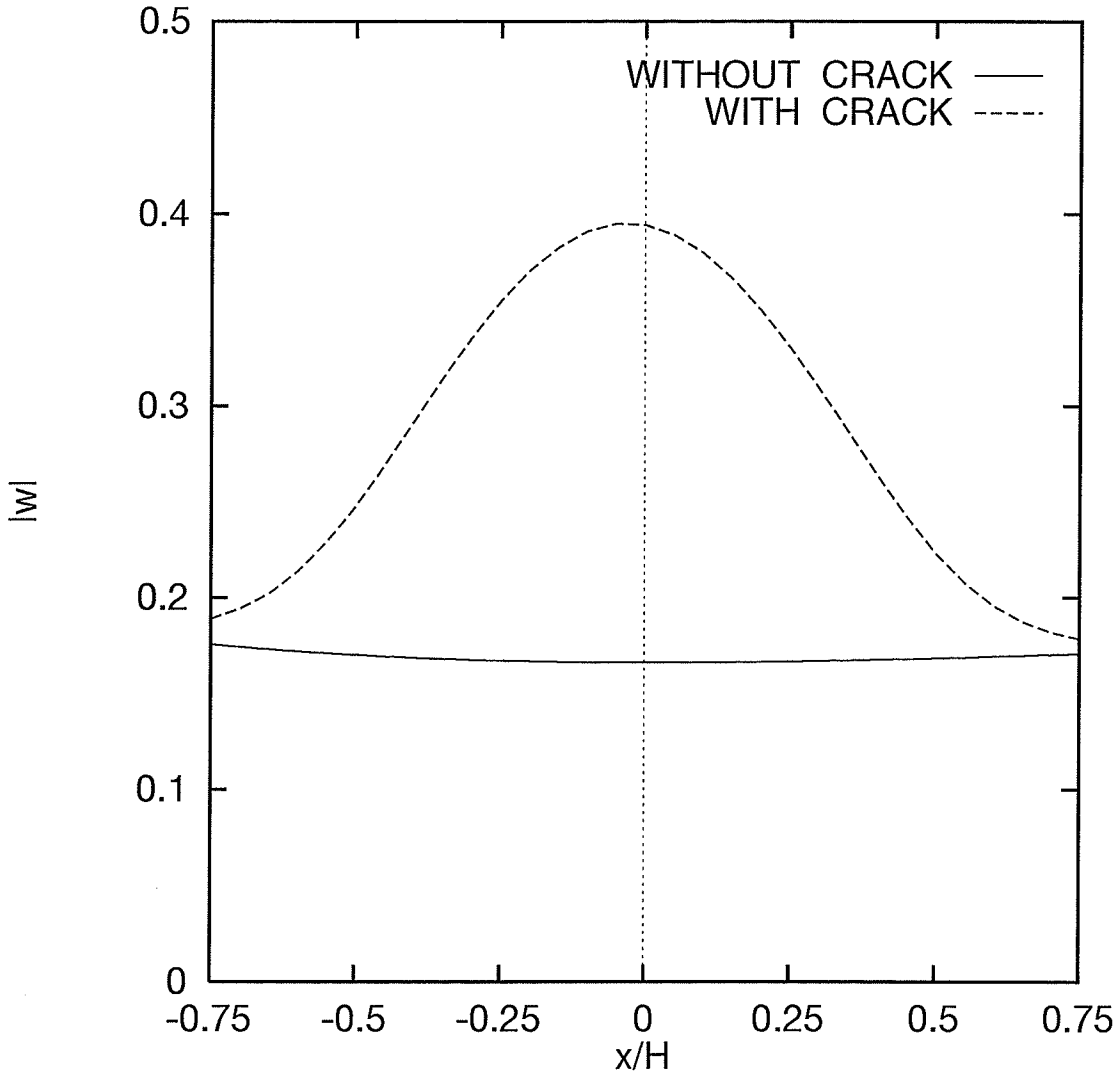

Figure 4.11: Vertical displacement on the top surface at $\Omega = 1$. Plane-strain modelling.

Chapter 5

3-D Green's Functions for Composite Plates

5.1 General

This chapter is concerned with the derivation of three-dimensional Green's functions for laminated composite plates. The technique developed in Chapter 4 is extended to decompose three-dimensional wave problem into a sequence of two dimensional wave problems. The elastic wave field is studied by the stiffness method to deal with the inhomogeneity along the thickness direction. The eigenvalues (wavenumbers) and eigenvectors (distribution through the thickness) are obtained by solving a generalized eigenvalue problem. Green's functions for composite plates are constructed through a numerical quadrature and the modal summation technique. Based on Cauchy residue theorem, Green's functions are expressed in a double series summation form. Numerical examples show the convergence of the method.

5.2 Description of the problem

Time-harmonic elastic wave propagation in an infinite plate composed of perfectly bonded layers with possibly distinct mechanical properties and thickness is considered. The two faces of the plate $z = 0$ and $z = 2H$ are traction-free. The global rectangular cartesian coordinate system (x, y, z) is shown in Figure 5.1.

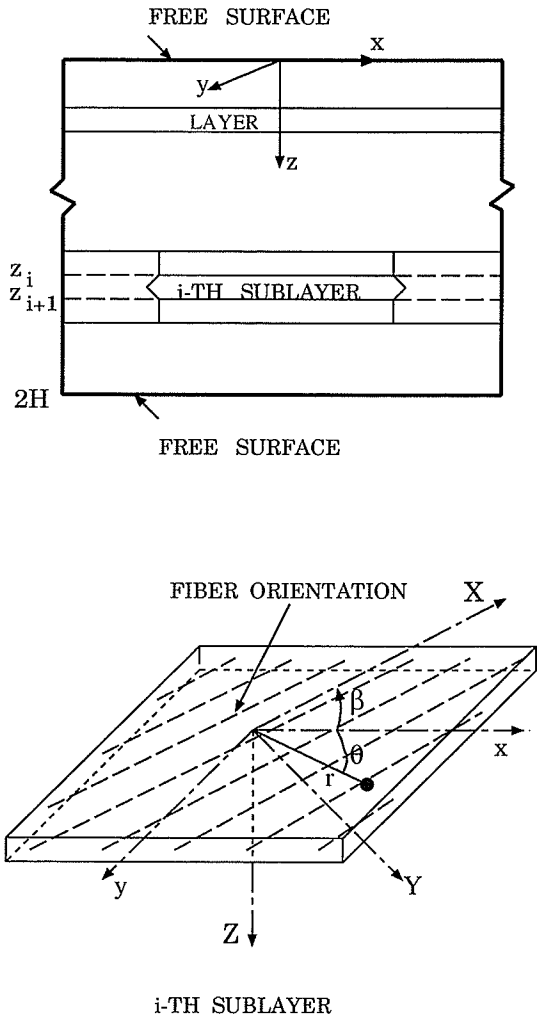

Figure 5.1: Configuration of a 3-D laminated composite plate

In the technique adopted here, each layer is divided into several sub-layers so that the total number of sub-layers through the thickness, $2H$, is N. For simplicity in the analysis, each layer is assumed to have transversely isotropic material properties with the material symmetry axis making an arbitrary angle β with the x- axis.

5.3 Governing Equations

Consider the i-th sub-layer bounded by $z = z_i$ and $z = z_{i+1}$. A local rectangular cartesian coordinate system (X, Y, Z) is chosen in the sub-layer with the origin on the top of the sub-layer, X- axis along the material symmetry axis (fiber direction), Z- axis vertically down, and Y- axis parallel to the plane of the plate, as shown in Figure 5.1. Let $U(X,Y,Z)$, $V(X,Y,Z)$, $W(X,Y,Z)$ be the displacement components of any particle within the sub-layer in X, Y, Z directions, respectively.

The strain-displacement relations within the sub-layer in the local coordinate system are given by

$$\begin{aligned}
\epsilon_{XX} &= \frac{\partial U}{\partial X}, \\
\epsilon_{YY} &= \frac{\partial V}{\partial Y}, \\
\epsilon_{ZZ} &= \frac{\partial W}{\partial Z}, \\
\epsilon_{YZ} &= \tfrac{1}{2}\gamma_{YZ} = \frac{1}{2}\left(\frac{\partial V}{\partial Z} + \frac{\partial W}{\partial Y}\right), \\
\epsilon_{ZX} &= \tfrac{1}{2}\gamma_{ZX} = \frac{1}{2}\left(\frac{\partial U}{\partial Z} + \frac{\partial W}{\partial X}\right), \\
\epsilon_{XY} &= \tfrac{1}{2}\gamma_{XY} = \frac{1}{2}\left(\frac{\partial V}{\partial X} + \frac{\partial U}{\partial Y}\right)
\end{aligned} \tag{5.1}$$

where ϵ_{IJ} represents strain component.

The stress-strain relation of this sub-layer in the local coordinate system is given by [75]

$$\{\sigma_{IJ}\} = \mathbf{C}\{\epsilon_{IJ}\} \tag{5.2}$$

where

$$\{\sigma_{IJ}\}^{\mathrm{T}} = \langle\, \sigma_{XX} \quad \sigma_{YY} \quad \sigma_{ZZ} \quad \sigma_{YZ} \quad \sigma_{ZX} \quad \sigma_{XY} \,\rangle \tag{5.3}$$

$$\{\epsilon_{IJ}\}^{\mathrm{T}} = \langle\, \epsilon_{XX} \quad \epsilon_{YY} \quad \epsilon_{ZZ} \quad \epsilon_{YZ} \quad \epsilon_{ZX} \quad \epsilon_{XY} \,\rangle \tag{5.4}$$

$$\mathbf{C} = \begin{bmatrix} C_{11} & C_{12} & C_{13} & 0 & 0 & 0 \\ C_{12} & C_{22} & C_{23} & 0 & 0 & 0 \\ C_{13} & C_{23} & C_{33} & 0 & 0 & 0 \\ 0 & 0 & 0 & 2C_{44} & 0 & 0 \\ 0 & 0 & 0 & 0 & 2C_{55} & 0 \\ 0 & 0 & 0 & 0 & 0 & 2C_{66} \end{bmatrix} \tag{5.5}$$

In the above σ_{IJ} represents stress component, C_{IJ} is the element of constitutive matrix for the sub-layer. Note that for transversely isotropic material

$$C_{22} = C_{33}, \qquad C_{55} = C_{66}, \qquad C_{12} = C_{13}, \qquad C_{44} = \frac{(C_{22} - C_{23})}{2}. \tag{5.6}$$

The equations of motion in the local coordinate system are given by

$$\begin{aligned} &\frac{\partial \sigma_{XX}}{\partial X} + \frac{\partial \sigma_{XY}}{\partial Y} + \frac{\partial \sigma_{XZ}}{\partial Z} + b_X + \rho\omega^2 U = 0, \\ &\frac{\partial \sigma_{XY}}{\partial X} + \frac{\partial \sigma_{YY}}{\partial Y} + \frac{\partial \sigma_{YZ}}{\partial Z} + b_Y + \rho\omega^2 V = 0, \\ &\frac{\partial \sigma_{XZ}}{\partial X} + \frac{\partial \sigma_{YZ}}{\partial Y} + \frac{\partial \sigma_{ZZ}}{\partial Z} + b_Z + \rho\omega^2 W = 0, \end{aligned} \tag{5.7}$$

where ρ is the density of the sub-layer; b_X, b_Y and b_Z are body forces in the X, Y and Z directions, respectively; and ω is the circular frequency.

Let β be the angle between the global x- axis and the local X- axis measured counterclockwise from the global x- axis. The relations between the displacements in

the two coordinate systems are determined by

$$\begin{aligned} \mathbf{U} &= \mathbf{T}(\beta)\mathbf{u} \\ \mathbf{u} &= [\mathbf{T}(\beta)]^{-1}\mathbf{U} = [\mathbf{T}(\beta)]^{\mathrm{T}}\mathbf{U} \end{aligned} \tag{5.8}$$

where

$$\mathbf{u}^{\mathrm{T}} = \langle\, u \quad v \quad w \,\rangle; \qquad \mathbf{U}^{\mathrm{T}} = \langle\, U \quad V \quad W \,\rangle \tag{5.9}$$

$$\mathbf{T}(\beta) = \begin{bmatrix} cos\beta & sin\beta & 0 \\ -sin\beta & cos\beta & 0 \\ 0 & 0 & 1 \end{bmatrix} \tag{5.10}$$

The stress vector $\{\sigma\}$ and strain vector $\{\epsilon\}$ for the sub-layer in the global (x, y, z) coordinate system are related by

$$\{\sigma\} = \mathbf{D}\{\epsilon\} \tag{5.11}$$

where

$$\begin{aligned} \{\sigma\}^T &= \{\, \sigma_{xx} \quad \sigma_{yy} \quad \sigma_{zz} \quad \sigma_{yz} \quad \sigma_{zx} \quad \sigma_{xy} \,\} \\ \{\epsilon\}^T &= \{\, \epsilon_{xx} \quad \epsilon_{yy} \quad \epsilon_{zz} \quad \epsilon_{yz} \quad \epsilon_{zx} \quad \epsilon_{xy} \,\} \end{aligned} \tag{5.12}$$

$$\mathbf{D} = \Gamma(\beta)\mathbf{C}[\Gamma(\beta)]^{-1} \tag{5.13}$$

where σ_{ij} and ϵ_{ij} represent stress and strain components, respectively, in the (x, y, z) coordinate system. Γ is a 6×6 matrix defined as

$$\Gamma(\beta) = \begin{bmatrix} cos^2\beta & sin^2\beta & 0 & 0 & 0 & sin2\beta \\ sin^2\beta & cos^2\beta & 0 & 0 & 0 & -sin2\beta \\ 0 & 0 & 1 & 0 & 0 & 0 \\ 0 & 0 & 0 & cos\beta & -sin\beta & 0 \\ 0 & 0 & 0 & sin\beta & cos\beta & 0 \\ -\frac{1}{2}sin2\beta & \frac{1}{2}sin2\beta & 0 & 0 & 0 & cos2\beta \end{bmatrix} \tag{5.14}$$

and has the property

$$[\Gamma(\beta)]^{-1} = \Gamma(-\beta) \tag{5.15}$$

For the transversely isotropic sub-layer equation (5.13) gives

$$\mathbf{D} = \begin{bmatrix} D_{11} & D_{12} & D_{13} & 0 & 0 & D_{16} \\ D_{12} & D_{22} & D_{23} & 0 & 0 & D_{26} \\ D_{13} & D_{23} & D_{33} & 0 & 0 & D_{36} \\ 0 & 0 & 0 & D_{44} & D_{45} & 0 \\ 0 & 0 & 0 & D_{45} & D_{55} & 0 \\ D_{16} & D_{26} & D_{36} & 0 & 0 & D_{66} \end{bmatrix} \tag{5.16}$$

D_{ij} are related to C_{IJ} by the equations presented in [76].

The displacement-strain relation is

$$\{\epsilon\} = \mathbf{L}\mathbf{u} \tag{5.17}$$

where

$$\mathbf{L}^T = \begin{bmatrix} \frac{\partial}{\partial x} & 0 & 0 & 0 & \frac{\partial}{\partial z} & \frac{\partial}{\partial y} \\ 0 & \frac{\partial}{\partial y} & 0 & \frac{\partial}{\partial z} & 0 & \frac{\partial}{\partial x} \\ 0 & 0 & \frac{\partial}{\partial z} & \frac{\partial}{\partial y} & \frac{\partial}{\partial x} & 0 \end{bmatrix} \tag{5.18}$$

The time harmonic wave motion equation in global coordinate system can be written as:

$$\mathbf{L}^T\mathbf{D}\mathbf{L}\mathbf{u} + \mathbf{b} + \rho\omega^2\mathbf{u} = \mathbf{0} \tag{5.19}$$

5.4 Decomposition of the equations

The application of double integral Fourier transform (refer to Chapter 4) to the governing equation (5.19) results in

$$\tilde{\mathbf{L}}^T\mathbf{D}\tilde{\mathbf{L}}\tilde{\mathbf{u}} + \tilde{\mathbf{b}} + \rho\omega^2\tilde{\mathbf{u}} = 0 \tag{5.20}$$

where $\tilde{\mathbf{u}}$ and $\tilde{\mathbf{b}}$ are the Fourier transforms of displacement vector $\mathbf{u}$ and body force vector $\mathbf{b}$, respectively, and

$$\tilde{\mathbf{L}}^T = \begin{bmatrix} -j\xi & 0 & 0 & 0 & \frac{\partial}{\partial z} & -j\eta \\ 0 & -j\eta & 0 & \frac{\partial}{\partial z} & 0 & -j\xi \\ 0 & 0 & \frac{\partial}{\partial z} & -j\eta & -j\xi & 0 \end{bmatrix} \tag{5.21}$$

Introducing variables k and ϕ as

$$\xi = kcos\phi; \quad \eta = ksin\phi, \tag{5.22}$$

expressing governing equation in the (x', y', z) coordinate system (refer to Chapter 4, Figure 4.3) we obtain

$$\tilde{\mathbf{L}}^T\mathbf{D}\tilde{\mathbf{L}}[\mathbf{T}(\phi)]^{-1}\hat{\tilde{\mathbf{u}}} + [\mathbf{T}(\phi)]^{-1}\hat{\tilde{\mathbf{b}}} + \rho\omega^2[\mathbf{T}(\phi)]^{-1}\hat{\tilde{\mathbf{u}}} = 0 \tag{5.23}$$

where

$$\begin{aligned} \hat{\tilde{\mathbf{u}}} &= \mathbf{T}(\phi)\tilde{\mathbf{u}} \\ \hat{\tilde{\mathbf{b}}} &= \mathbf{T}(\phi)\tilde{\mathbf{b}} \end{aligned} \tag{5.24}$$

Multiplying equation (5.23) with $\mathbf{T}(\phi)$ yields:

$$\mathbf{T}(\phi)\tilde{\mathbf{L}}^T\mathbf{D}\tilde{\mathbf{L}}[\mathbf{T}(\phi)]^{-1}\hat{\tilde{\mathbf{u}}} + \hat{\tilde{\mathbf{b}}} + \rho\omega^2\hat{\tilde{\mathbf{u}}} = 0 \tag{5.25}$$

Let

$$\mathbf{T}(\phi)\tilde{\mathbf{L}}^{\mathrm{T}} = \mathbf{L}_k^{\mathrm{T}}\Gamma(\phi) \tag{5.26}$$

$\mathbf{L}_k^{\mathrm{T}}$ is obtained by inspection of equation (5.14) as

$$\mathbf{L}_k^T = \begin{bmatrix} -jk & 0 & 0 & 0 & \frac{\partial}{\partial z} & 0 \\ 0 & 0 & 0 & \frac{\partial}{\partial z} & 0 & -jk \\ 0 & 0 & \frac{\partial}{\partial z} & 0 & -jk & 0 \end{bmatrix} \tag{5.27}$$

Equation (5.25) can be arranged as:

$$\mathbf{L}_k^T\mathbf{D}'\mathbf{L}_k\hat{\tilde{\mathbf{u}}} + \hat{\tilde{\mathbf{b}}} + \rho\omega^2\hat{\tilde{\mathbf{u}}} = 0 \tag{5.28}$$

by noticing

$$\tilde{\mathbf{L}}[\mathbf{T}(\phi)]^{-1} = \tilde{\mathbf{L}}[\mathbf{T}(\phi)]^{\mathrm{T}} = [\mathbf{T}(\phi)\tilde{\mathbf{L}}^{\mathrm{T}}]^{\mathrm{T}} = [\Gamma(\phi)]^{\mathrm{T}}\mathbf{L}_k \tag{5.29}$$

where

$$\mathbf{D}' = \Gamma(\phi)\mathbf{D}[\Gamma(\phi)]^{\mathrm{T}} \tag{5.30}$$

Expanding $\mathbf{L}_k^T\mathbf{D}'\mathbf{L}_k$ leads to the governing equation as

$$[\mathbf{A}_1 - jk\mathbf{A}_2\frac{\partial}{\partial z} - k^2\mathbf{A}_3\frac{\partial^2}{\partial z^2} + \rho\omega^2]\hat{\tilde{\mathbf{u}}} + \hat{\tilde{\mathbf{b}}} = 0 \tag{5.31}$$

where

$$\begin{aligned}
\mathbf{A}_1 &= \begin{bmatrix} D'_{55} & D'_{45} & 0 \\ D'_{45} & D'_{44} & 0 \\ 0 & 0 & D'_{33} \end{bmatrix} \\
\mathbf{A}_2 &= \begin{bmatrix} 0 & 0 & D'_{13}+D'_{55} \\ 0 & 0 & D'_{36}+D'_{45} \\ D'_{13}+D'_{55} & D'_{45}+D'_{36} & 0 \end{bmatrix} \\
\mathbf{A}_3 &= \begin{bmatrix} D'_{11} & D'_{16} & 0 \\ D'_{16} & D'_{66} & 0 \\ 0 & 0 & D'_{55} \end{bmatrix}
\end{aligned} \tag{5.32}$$

In the above D'_{ij} is element of $\mathbf{D}'$ matrix.

In the case of isotropic material,

$$\begin{aligned}
D'_{11} &= D'_{33} = \lambda + 2\mu \\
D'_{44} &= D'_{55} = D'_{66} = \mu \\
D'_{13} &= \lambda \\
D'_{16} &= D'_{36} = D'_{45} = 0
\end{aligned} \tag{5.33}$$

and equation (5.31) reduces to equation (4.45) which, as illustrated in Chapter 4, contains governing equations for plane-strain and antiplane problems with waves travelling in x' direction.

Equation (5.31) governs waves traveling in x' direction with wavenumber k. The wave fields are independent of y' direction. It is seen that the three-dimensional wave propagation is decomposed into a series of two-dimensional wave problems with three displacements coupled.

5.5 Green's function

The employment of Rayleigh-Ritz approximation based stiffness method to equation (5.31) gives the approximate governing equation as

$$\hat{\tilde{\mathbf{F}}} = (k^2\mathbf{K}_1 - jk\mathbf{K}_2 + \mathbf{K}_3 - \omega^2\mathbf{M})\hat{\tilde{\mathbf{Q}}} \tag{5.34}$$

where vectors $\hat{\tilde{\mathbf{Q}}}$ and $\hat{\tilde{\mathbf{F}}}$ represent the nodal displacements and tractions through the thickness of the plate in the transformed domain. $\mathbf{M}$ and $\mathbf{K}_i (i = 1, 2, 3)$ are mass matrix and stiffness matrices, respectively [49, 76].

Following the same procedure as illustrated in Chapter 2 a standard eigenvalue problem can be established. The solution to equation (5.34) is obtained through the modal summation technique as:

$$\hat{\tilde{\mathbf{Q}}} = \sum_{m=1}^{2M} \frac{\mathbf{\Phi}^L_{m2}\hat{\tilde{\mathbf{F}}}\mathbf{\Phi}^R_{m1}}{(k_m - k)B_m} \tag{5.35}$$

where k_m is wavenumber, B_m is the orthogonality coefficient, $\mathbf{\Phi}^{\mathrm{L}}_{m2}$ and $\mathbf{\Phi}^{\mathrm{R}}_{m1}$ are left and right eigenvectors.

The Fourier transform of a point load acting at point $(0, 0, z_0)$ is

$$\tilde{\mathbf{f}} = \mathbf{f}_0 = \langle\, f_x \quad f_y \quad f_z \,\rangle^{\mathrm{T}} \tag{5.36}$$

where f_x, f_y and f_z are the amplitudes of the load in x, y and z directions, respectively.

Transferring the $\tilde{\mathbf{f}}$ into (x', y', z) coordinate system

$$\hat{\tilde{\mathbf{f}}} = \begin{Bmatrix} \hat{\tilde{f}}_{x'} \\ \hat{\tilde{f}}_{y'} \\ \hat{\tilde{f}}_{z} \end{Bmatrix} = \mathbf{T}(\phi)\tilde{\mathbf{f}} = \begin{Bmatrix} f_x cos\phi + f_y sin\phi \\ -f_x sin\phi + f_y cos\phi \\ f_z \end{Bmatrix} \tag{5.37}$$

we obtain

$$\hat{\tilde{\mathbf{F}}}^{\mathrm{T}} = \langle 0 \quad \cdots \quad 0 \quad \hat{\tilde{f}}_{x'} \quad \hat{\tilde{f}}_{y'} \quad \hat{\tilde{f}}_{z} \quad 0 \quad \cdots \quad 0 \rangle \tag{5.38}$$

and

$$\begin{aligned} \mathbf{\Phi}^{\mathrm{L}}_{m2}\hat{\tilde{\mathbf{F}}} &= \psi_1 \hat{\tilde{f}}_{x'} + \psi_2 \hat{\tilde{f}}_{y'} + \psi_3 \hat{\tilde{f}}_{z} \\ &= \bar{\psi}_1 cos\phi + \bar{\psi}_2 sin\phi + \bar{\psi}_3 \end{aligned} \tag{5.39}$$

where ψ_1, ψ_2 and ψ_3 are the corresponding elements in $\mathbf{\Phi}^{\mathrm{L}}_{m2}$, and

$$\begin{aligned} \bar{\psi}_1 &= \psi_1 f_x + \psi_2 f_y \\ \bar{\psi}_2 &= \psi_1 f_y - \psi_2 f_x \\ \bar{\psi}_3 &= \psi_3 f_z \end{aligned} \tag{5.40}$$

Let $\hat{\tilde{\mathbf{u}}}$ be a vector which represents displacement of a *nodal point*. Equations (5.35) and (5.39) give

$$\hat{\tilde{\mathbf{u}}} = \sum_{m=1}^{2M} \frac{\bar{\psi}_1 cos\phi + \bar{\psi}_2 sin\phi + \bar{\psi}_3}{(k_m - k)B_m} \begin{Bmatrix} U_m \\ V_m \\ W_m \end{Bmatrix} \tag{5.41}$$

where U_m, V_m and W_m are the corresponding elements in the right eigenvector $\mathbf{\Phi}^{\mathrm{R}}_{m1}$.

Transfer $\hat{\tilde{\mathbf{u}}}$ into (r, θ, z) coordinate system:

$$\begin{aligned} \tilde{\mathbf{u}} &= \begin{Bmatrix} \tilde{u}_r \\ \tilde{u}_\theta \\ \tilde{w} \end{Bmatrix} = [\mathbf{T}(\phi - \theta)]^{-1} \hat{\tilde{\mathbf{u}}} \\ &= \sum_{m=1}^{2M} \frac{\bar{\psi}_1 cos\phi + \bar{\psi}_2 sin\phi + \bar{\psi}_3}{(k_m - k)B_m} \begin{Bmatrix} U_m cos(\phi - \theta) - V_m sin(\phi - \theta) \\ U_m sin(\phi - \theta) + V_m cos(\phi - \theta) \\ W_m \end{Bmatrix} \end{aligned} \tag{5.42}$$

Application of the inverse Fourier transform to the above equation gives the displacements as

$$\mathbf{u} = \begin{Bmatrix} u_r \\ u_\theta \\ w \end{Bmatrix} = \frac{1}{(2\pi)^2} \int\int_{(k,\phi)} \tilde{\mathbf{u}} e^{jkrcos(\phi-\theta)} k dk d\phi$$

$$= \frac{1}{(2\pi)^2} \int\int_{(k,\phi)} \sum_{m=1}^{2M} \frac{\bar{\psi}_1 cos\phi + \bar{\psi}_2 sin\phi + \bar{\psi}_3}{(k_m - k)B_m} \times \begin{Bmatrix} U_m cos(\phi-\theta) - V_m sin(\phi-\theta) \\ U_m sin(\phi-\theta) + V_m cos(\phi-\theta) \\ W_m \end{Bmatrix} e^{jkrcos(\phi-\theta)} k dk d\phi \quad (5.43)$$

Through an analogous procedure as in isotropic plate analysis the displacements are obtained as

$$\begin{Bmatrix} u_r \\ u_\theta \\ w \end{Bmatrix} = -\frac{1}{(2\pi)^2} \int_{-\pi/2}^{\pi/2} \int_{-\infty}^{\infty} \sum_{m=1}^{M} \frac{\bar{\psi}_1 cos(\varphi+\theta) + \bar{\psi}_2 sin(\varphi+\theta) + \bar{\psi}_3}{B_m} \times (1 + \frac{k_m}{k - k_m}) \begin{Bmatrix} U_m cos\varphi - V_m sin\varphi \\ U_m sin\varphi + V_m cos\varphi \\ W_m \end{Bmatrix} e^{jkrcos\varphi} dk d\varphi \quad (5.44)$$

where

$$\varphi = \phi - \theta$$

Numerical quadrature is required to carry out the integrals. Dividing the domain $[-\frac{\pi}{2}, \frac{\pi}{2}]$ into I subdomains with equal intervals leads to

$$\begin{Bmatrix} u_r \\ u_\theta \\ w \end{Bmatrix} = -\frac{1}{(2\pi)^2} [\sum_{i=1}^{I} \int_{\Delta\varphi_i} \int_{-\infty}^{\infty} \sum_{m=1}^{M} \frac{\bar{\psi}_1 cos(\varphi+\theta) + \bar{\psi}_2 sin(\varphi+\theta) + \bar{\psi}_3}{B_m} \times (1 + \frac{k_m}{k - k_m}) \begin{Bmatrix} U_m cos\varphi - V_m sin\varphi \\ U_m sin\varphi + V_m cos\varphi \\ W_m \end{Bmatrix} e^{jkrcos\varphi} dk d\varphi] \quad (5.45)$$

z-direction load

For a z-direction unit load, equation (5.45) is simplified as follows according to equation (5.40) and the property of δ function (Chapter 4):

$$\begin{Bmatrix} u_r \\ u_\theta \\ w \end{Bmatrix} = -\frac{1}{2\pi}[\sum_{i=1}^{I}\int_{\Delta\varphi}\sum_{m=1}^{M}\frac{\bar{\psi}_3}{B_m}\delta(rcos\varphi)\begin{Bmatrix} U_m cos\varphi - V_m sin\varphi \\ U_m sin\varphi + V_m cos\varphi \\ W_m \end{Bmatrix}\mathrm{d}\varphi + \sum_{i=1}^{I}\sum_{m=1}^{M}\frac{\bar{\psi}_3}{B_m}jk_m\begin{Bmatrix} U_m cos\varphi_i - V_m sin\varphi_i \\ U_m sin\varphi_i + V_m cos\varphi_i \\ W_m \end{Bmatrix} e^{jk_m r cos\varphi_i}\Delta\varphi] \quad (5.46)$$

where Cauchy residue theorem (it is noted that $\bar{\psi}_3$, B_m and U_m, V_m and W_m are independent of k) and the middle point integration formula have been applied to derive the second double summation term.

To compute the remaining integral in equation (5.46) following expressions are useful:

$$\begin{aligned} &\int_{\Delta\varphi}\delta(rcos\varphi)\mathrm{d}\varphi = \begin{Bmatrix} -\frac{1}{r} & \pm\frac{\pi}{2}\in\Delta\varphi \\ 0 & \text{otherwise} \end{Bmatrix} \\ &\int_{\Delta\varphi}\delta(rcos\varphi)cos\varphi\mathrm{d}\varphi = 0 \qquad (5.47) \\ &\int_{\Delta\varphi}\delta(rcos\varphi)sin\varphi\mathrm{d}\varphi = \begin{Bmatrix} -\frac{1}{r} & -\frac{\pi}{2}\in\Delta\varphi \\ \frac{1}{r} & \frac{\pi}{2}\in\Delta\varphi \\ 0 & \text{otherwise} \end{Bmatrix} \qquad (5.48) \end{aligned}$$

The displacement vector due to the z-direction unit load is obtained as

$$\begin{Bmatrix} u_r \\ u_\theta \\ w \end{Bmatrix} = \frac{1}{\pi r}\sum_{m=1}^{M}\frac{\bar{\psi}_3^*}{B_m^*}\begin{Bmatrix} 0 \\ 0 \\ W_m^* \end{Bmatrix}$$

$$- \frac{j}{2\pi}\sum_{i=1}^{I}\sum_{m=1}^{M}\frac{\bar{\psi}_3 k_m}{B_m}\begin{Bmatrix} U_m cos\varphi_i - V_m sin\varphi_i \\ U_m sin\varphi_i + V_m cos\varphi_i \\ W_m \end{Bmatrix} e^{jk_m r cos\varphi_i}\Delta\varphi \qquad (5.49)$$

where superscript $*$ represents quantities corresponding to the wave travelling in the direction $\varphi = \phi - \theta = \frac{\pi}{2}$.

x or y-direction load

From equation (5.40), the displacement vector due to x or y direction unit load has the form

$$\begin{Bmatrix} u_r \\ u_\theta \\ w \end{Bmatrix} = -\frac{1}{(2\pi)^2}[\sum_{i=1}^{I}\int_{\Delta\varphi}\int_{-\infty}^{\infty}\sum_{m=1}^{M}\frac{\bar{\psi}_1 cos(\varphi+\theta) + \bar{\psi}_2 sin(\varphi+\theta)}{B_m}$$
$$\times(1+\frac{k_m}{k-k_m})\begin{Bmatrix} U_m cos\varphi - V_m sin\varphi \\ U_m sin\varphi + V_m cos\varphi \\ W_m \end{Bmatrix} e^{jkr cos\varphi} dk d\varphi] \qquad (5.50)$$

Following the same procedure used in deriving the displacement vector due to z-direction load, we obtain:

$$\begin{Bmatrix} u_r \\ u_\theta \\ w \end{Bmatrix} = \frac{1}{\pi r}\sum_{m=1}^{M}\frac{\bar{\psi}_1^* sin\theta - \bar{\psi}_2^* cos\theta}{B_m^*}\begin{Bmatrix} V_m^* \\ U_m^* \\ 0 \end{Bmatrix}$$
$$- \frac{j}{2\pi}\sum_{i=1}^{I}\sum_{m=1}^{M}\frac{\bar{\psi}(\varphi_i)k_m}{B_m}\begin{Bmatrix} U_m cos\varphi_i - V_m sin\varphi_i \\ U_m sin\varphi_i + V_m cos\varphi_i \\ W_m \end{Bmatrix} e^{jk_m r cos\varphi_i}\Delta\varphi \qquad (5.51)$$

where

$$\bar{\psi}(\varphi_i) = \bar{\psi}_1 cos(\varphi_i + \theta) + \bar{\psi}_2 sin(\varphi_i + \theta)$$

Table 5.1: Elastic properties of single layer Graphite/Epoxy fibers (GPa)

C_{11}	C_{33}	C_{13}	C_{23}	C_{55}
160.73	13.92	6.44	6.92	7.07

5.6 Numerical implementation

The technique illustrated above is applied to analyze the three-dimensional wave propagation problem and compute Green's functions for the following examples:

Example 1. - a single layer graphite/epoxy cross-ply laminated plate with fibers being aligned with the x direction. The relevant elastic constants are the same as those of example 2 in Chapter 2. They are reproduced here in Table 5.1 for ease of reference.

Example 2. - a 8-layer graphite/epoxy cross-ply laminated plate with 0°/90°/0°/90°/90°/0°/90°/0° configuration.

A vertical unit load acting at $(0, 0, H/4)$ is supposed for both the examples. The normalized frequency Ω is equal to 1. To compute the wavenumbers and eigenvectors, the plate is divided into sixteen sub-layers for both examples.

Example 1

As is illustrated above, the three-dimensional wave propagation problem can be decomposed into a sequence of two-dimensional problems. Figure 5.2 shows the variation of first three propagating wavenumbers (first three propagating modes) versus the propagation direction in the single layer plate. The horizontal axis represents the

angles between the wave travelling directions and x axis. It is seen that the wavenumbers in a direction, say φ, are same as those in $-\varphi$ direction. That is because the material properties are symmetric about x axis. Figure 5.2 also shows that the first and third wavenumbers reach their minima as the waves travelling in fiber direction ($\varphi = 0°$) while the second wavenumber reaches its maximum at this direction. All these wavenumbers have maximum values as waves travel in the direction ($\varphi = 90°$) perpendicular to the fiber direction.

For the numerical computation of displacement Green's functions the domain $[-\frac{\pi}{2}, \frac{\pi}{2}]$ is divided into a number of subdomains with equal intervals. Different divisions are utilized to investigate the convergence of the numerical quadrature. Figure 5.3 represents the top surface displacement along x axis from three kinds of divisions, the interval $\Delta\varphi$ being 2.5°, 5° and 10°. In this figure, the horizontal axis (labelled as r/H) represents distance from the source point to observation point. It is seen that the results from 5° division are close to those from 2.5° division. Also 10° division gives stable results. Figure 5.4 shows the results along a line making 45° angle with fiber direction. The results from 5° division are in very good agreements with those from 2.5° division. The results from 10° division are oscillating.

The top surface displacement for a line perpendicular to the fiber direction from the same divisions are shown in Figure 5.5. It is seen that the results are not sensitive to the divisions.

Example 2

Figure 5.6 shows the variation of first three propagating wavenumbers with the propagation direction in the 8-layer plate. Similar variations of the wavenumbers are observed as for single layer plate (Figure 5.2). The slope of the third wavenumber in this figure is much smaller than that in Figure 5.2. This is due to the effect of

multilayer configuration of the plate.

Figure 5.7 shows the top surface displacements along lines making 0°, 45° and 90° angles with x axis. The interval is 5° in the numerical quadrature. It is seen that the displacements of the top surface points along x axis are larger than those along other directions.

5.7 Concluding remarks

Three-dimensional waves in laminated composite plates are studied in this Chapter. Double Fourier integral transforms are employed to obtain the governing equations in a transformed wavenumber domain. By introducing a coordinate transform the problem is decomposed into a sequence of two-dimensional problems. Green's functions for the laminated composite plates are constructed through summing the contribution of all the two-dimensional problems and the application of Rayleigh-Ritz procedure and modal summation technique. The numerical efficiency is achieved by replacing the double infinite integrals with two finite summations. Numerical examples show the convergence of the technique.

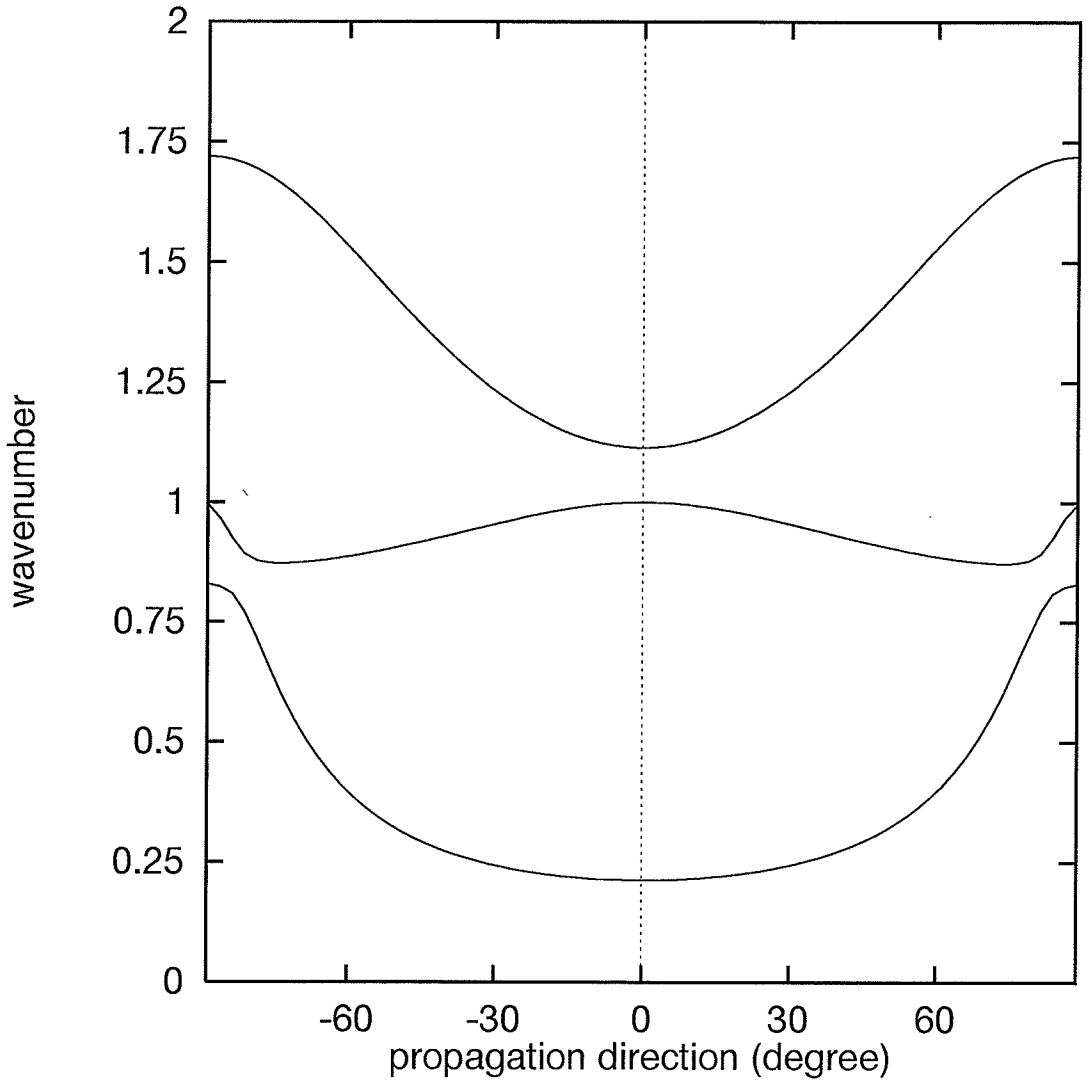

Figure 5.2: Variation of wave numbers versus propagation direction in the single layered plate

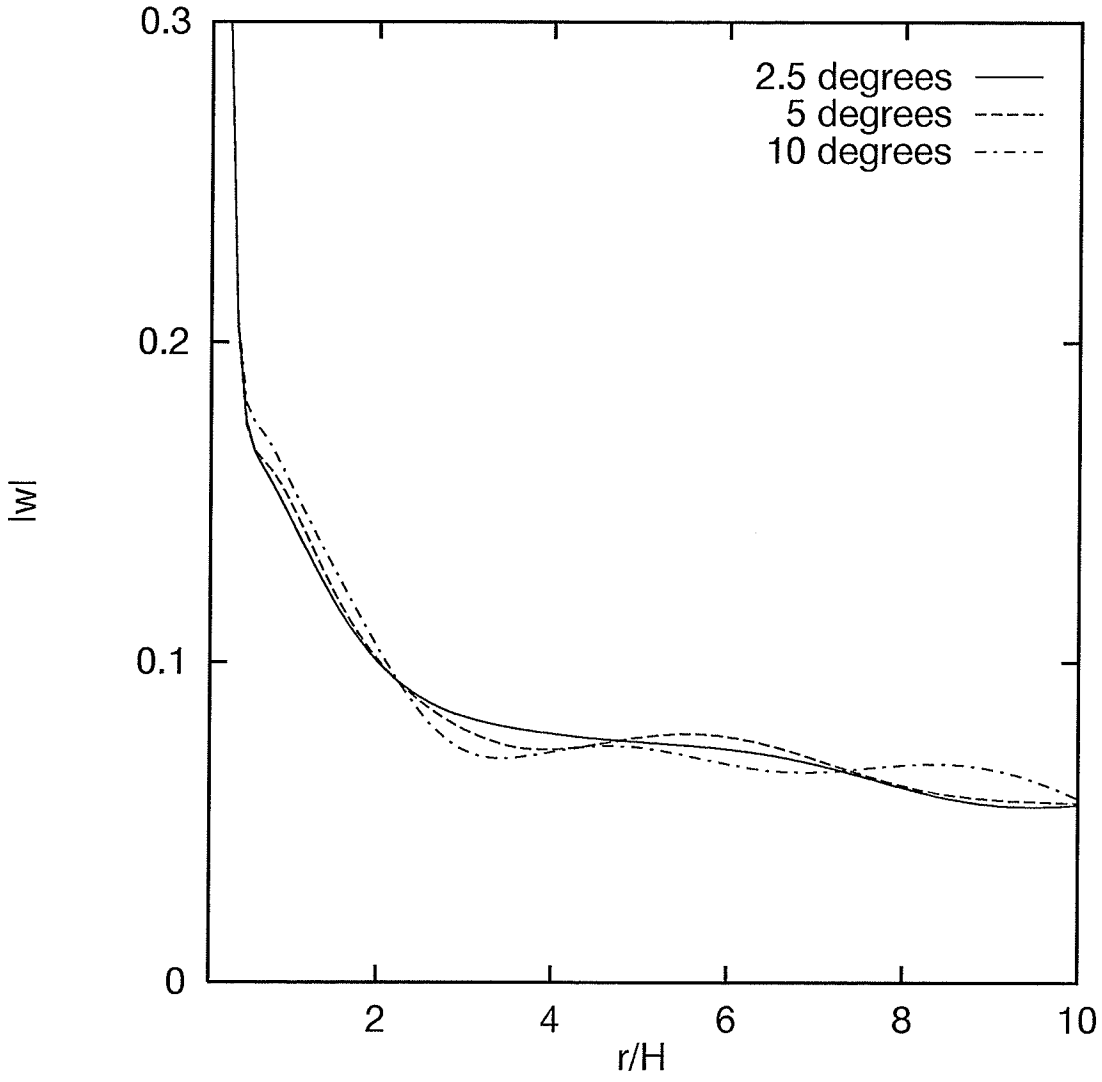

Figure 5.3: Variation of top surface displacement in the single layer plate at 0°

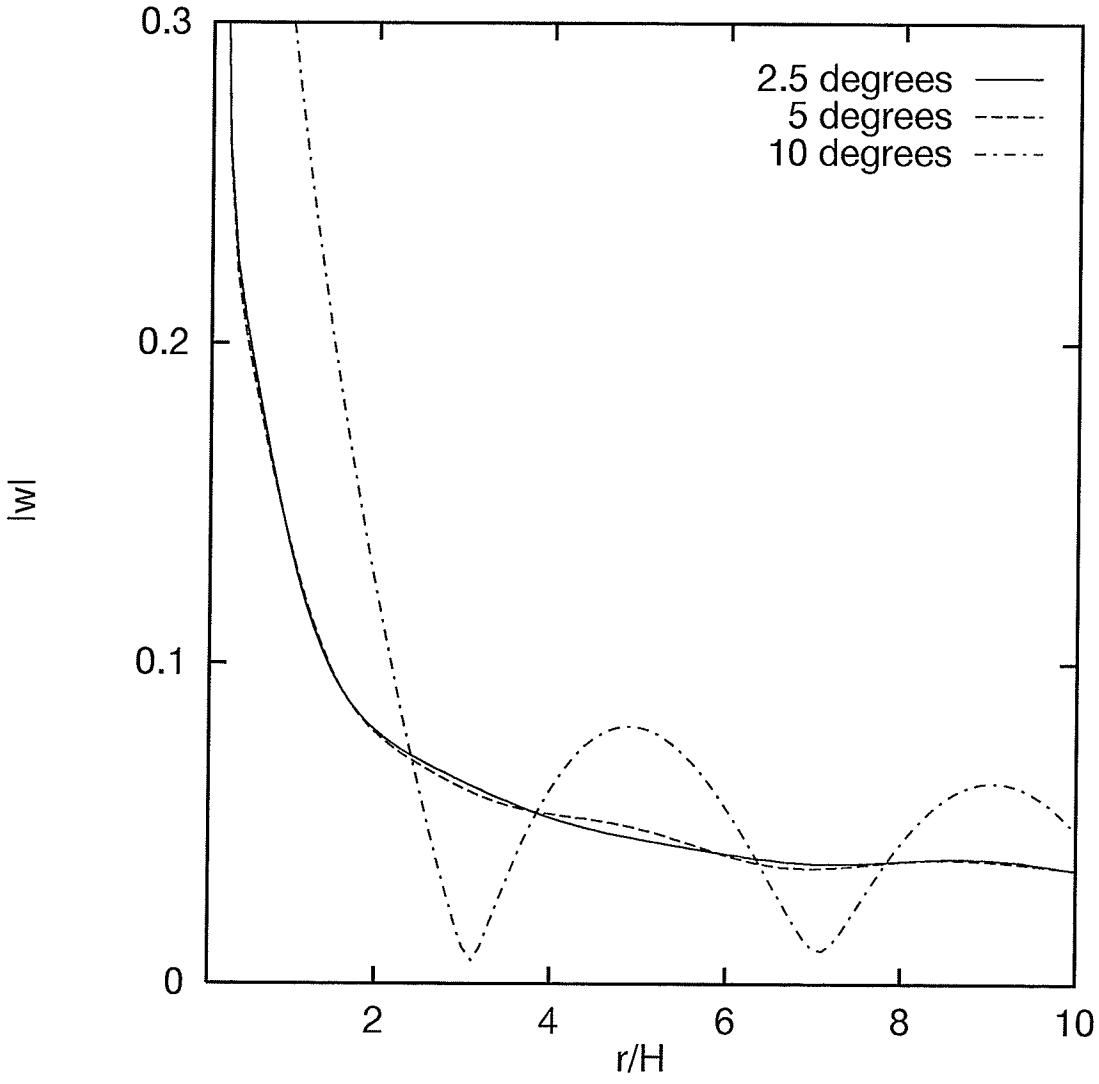

Figure 5.4: Variation of top surface displacement in the single layer plate at 45°

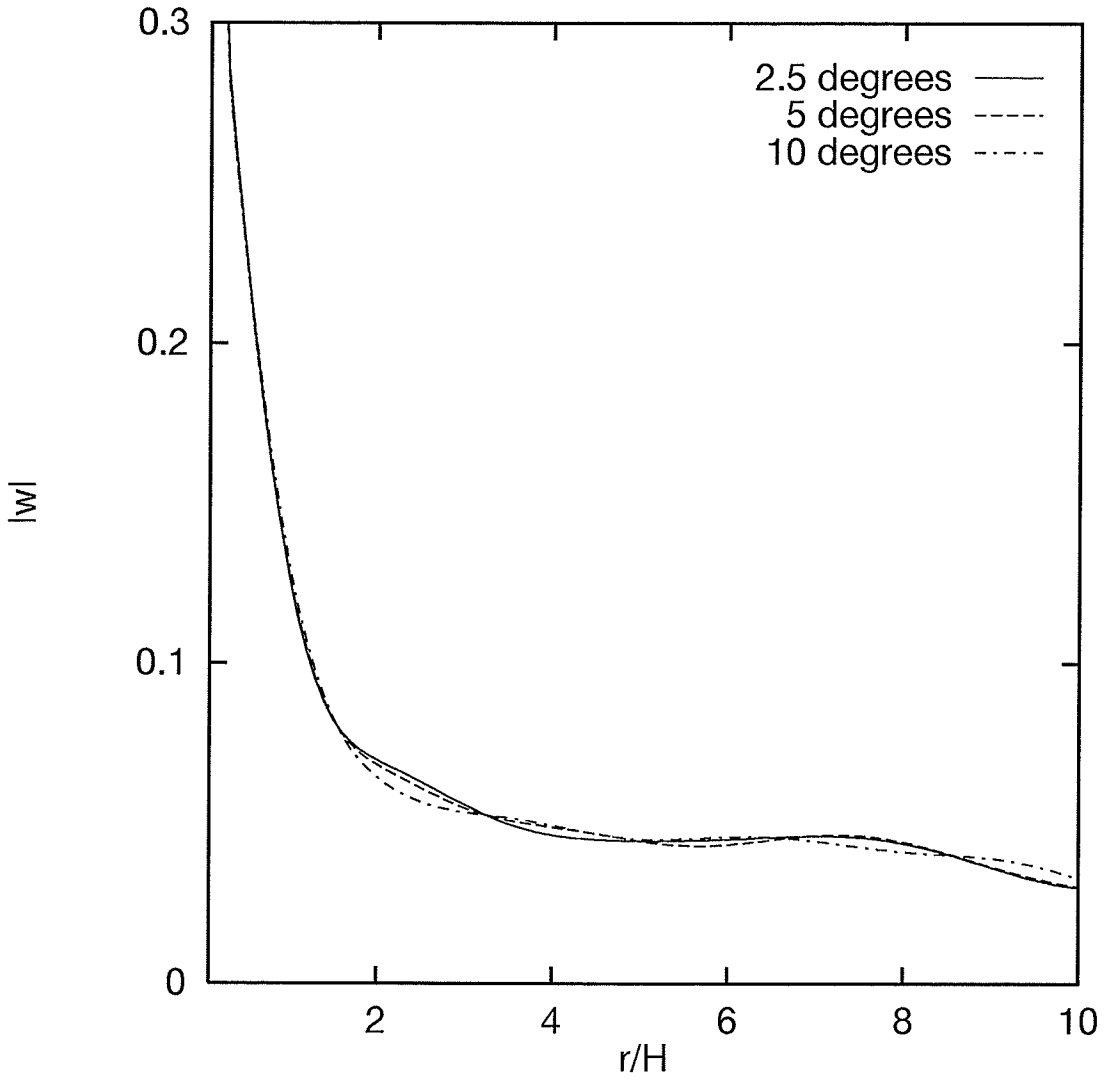

Figure 5.5: Variation of top surface displacement in the single layer plate at 90°

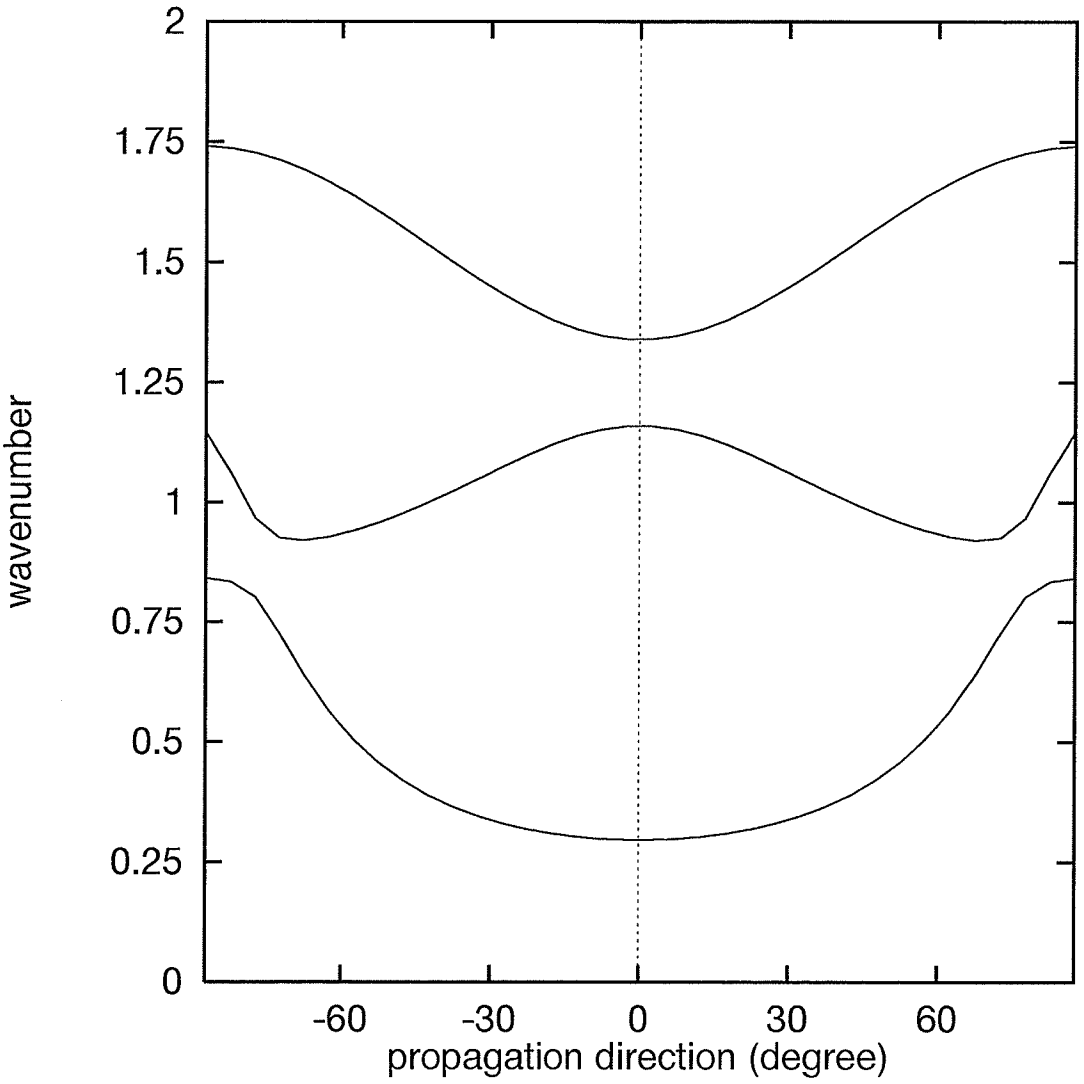

Figure 5.6: Variation of wave numbers versus propagation direction in the 8-layer plate

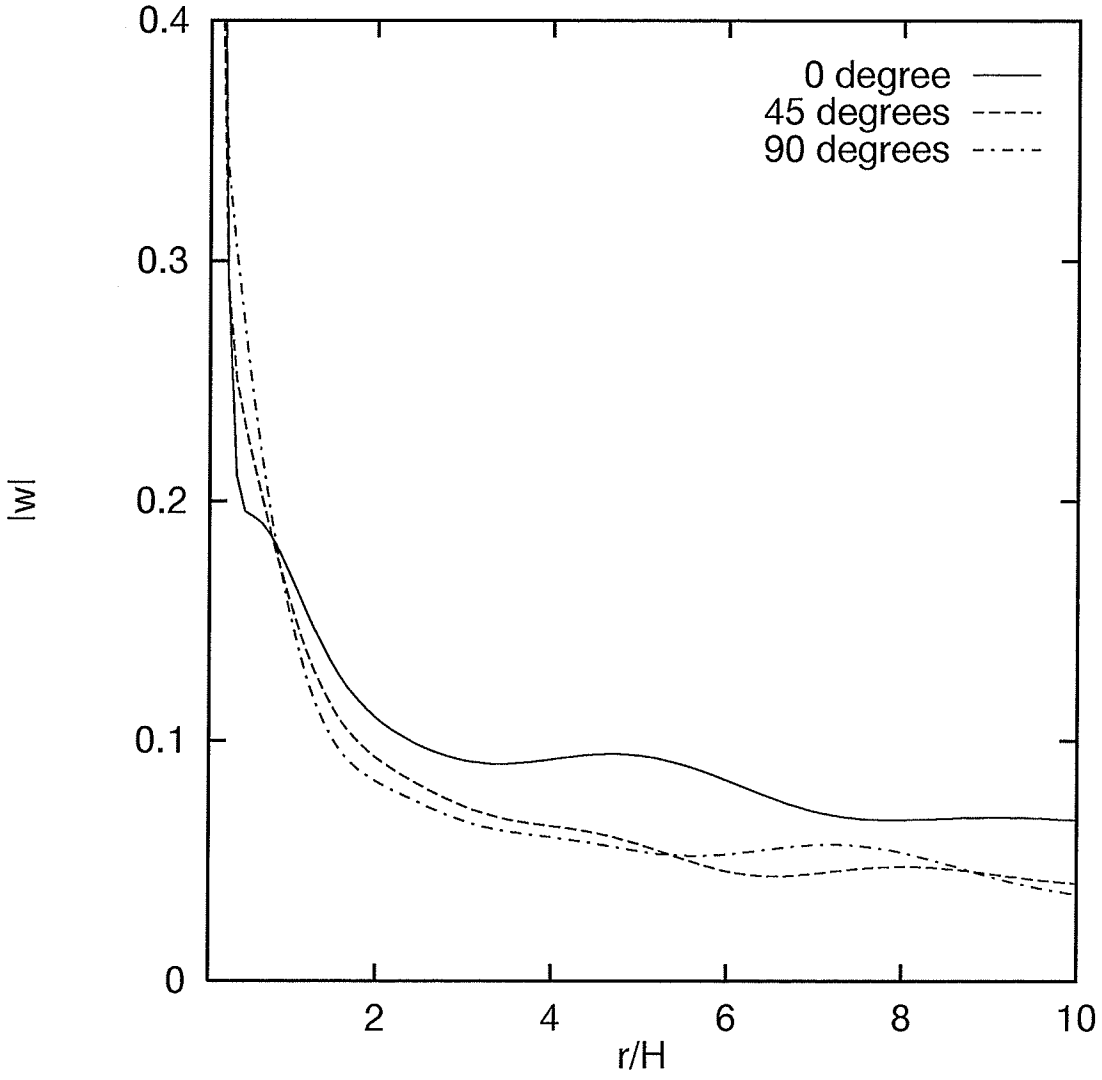

Figure 5.7: Variation of top surface displacement in the 8-layer plate

Chapter 6

Concluding Remarks

6.1 Conclusions

An analytical formulation of wave propagation is employed for plane-strain analysis of laminated composite plates and axisymmetric analysis of isotropic plates. Based on this formulation, a method is developed to compute the plane-strain elastodynamic Green's functions in terms of the guided wave modes due to line loads in laminated composite plates. It is shown that accurate computation of the Green's functions can be made both in the near and far fields by keeping not only the propagating modes, but also the non-propagating and evanescent modes, in the wave function expansion.

The Rayleigh-Ritz type approximation based stiffness method is used to investigate the two-dimensional wave phenomenon. The dispersion relation is obtained as a standard matrix eigenvalue problem. The orthogonality relations of the left and right eigenvectors are used together with the modal summation technique to construct the Green's functions.

In the analysis of wave propagation in isotropic plates, a three-dimensional problem is decomposed into a series of plane-strain and antiplane problems. An explicit

expression of three-dimensional elastodynamic Green's functions is obtained.

It is also illustrated that the three-dimensional wave propagation problem in a laminated composite plate can be decomposed into a sequence of two-dimensional problems. The three-dimensional Green's functions are expressed in a double summation form with respect to the travelling directions and wavenumbers.

A hybrid method which incorporates finite element formulation in a bounded interior region containing all the flaws with a modal representation in the exterior region is employed to investigate plane-strain wave scattering problem in laminated composite plates.

The boundary element method is applied to analyze scattering of plane-strain waves by cracks in laminated composite plates. A new technique is established to evaluate the Cauchy principal value integrals and weakly singular integrals involved in the boundary integral equations. This technique is also extended to three-dimensional wave scattering analysis. Numerical computations show that the boundary element method is much more efficient than the hybrid method especially when large cracks are involved in the analysis.

6.2 Recommendation for Future Work

The comprehensive set of Green's functions together with the boundary element analysis technique and software package presented in this thesis can be applied to analyze a variety of problems. The following recommendations are made for future work.

1 . The theoretical findings of the present study should be experimentally validated by carrying out ultrasonic testing of laminated composite plate specimens.

2 . The new technique to evaluate the CPV singular and weakly singular integrals involved in boundary element analysis should be systematically refined and incorporated into general application of boundary element analysis.

3 . More studies are needed on the numerical aspects of three dimensional Green's functions for laminated composite plates and their incorporation into three dimensional boundary element analysis.

Bibliography

[1] Jones, R.M., (1975). *Mechanics of Composite Materials.* McGraw-Hill Book Co. New York.

[2] Mindlin, R.D., (1960). "Waves and vibrations in isotropic, elastic solids." *Proc. 1st Symp. Naval Structural Mechanics* (Edited by J.N.Goodier and N.Noff), 199-232. Pergamon Press, Oxford, U.K.

[3] Nayfeh, A.H. and Chimenti, D.E., (1989). "Free wave propagation in plates of general anisotropic media." *ASME J. Appl. Mech.,* **56**, 881-886.

[4] Baylis, E.R. and Green, W.A., (1986a). "Flexural waves in fiber-reinforced laminated plates." *J. Sound and Vibration*, **110**(1), 1-26.

[5] Baylis, E.R. and Green, W.A., (1986b). "Flexural waves in fiber-reinforced laminated plates, Part II." *J. Sound and Vibration*, **111**(2), 181-190.

[6] Baylis, E.R., (1988). "Wave propagation in asymmetric fiber-reinforced laminated plate, Part II." *Acta Mechanica*, **71**, 167-183.

[7] Kapania, R.K. and Raciti, S., (1989). "Recent advances in analysis of laminated beams and plates, Part II: Vibrations and wave propagation." *AIAA Journal,* **27**(7), 935-946.

[8] Librescu, L. and Reddy, J.N., (1989). "A few remarks concerning several refined theories of anisotropic composite laminated plates." *Int. J. Eng. Sci.,* **27**(5), 515-527.

[9] Dong, S.B. and Huang, K.H., (1985). "Edge vibrations in laminated composite plates." *ASME J. Appl. Mech.,* **52**(2), 433-438.

[10] Dong, S.B. and Nelson, R.B., (1972). "On natural vibrations and waves in laminated orthotropic plates." *J. Appl. Mech.,* **39**, 739-745.

[11] Dong, S.B. and Pauley, K.E., (1978). "Plane waves in anisotropic plates." *J. Eng. Mech.,* **104**, 801-817.

[12] Datta, S.K., Shah, A.H., Bratton, R.L., and Chakraborty, T., (1988). "Wave propagation in laminated composite plates." *J. Acoust. Soc. Am.,* **83**, 2020-2026.

[13] Karunasena,W.M., Shah,A.H., and Datta,S.K., (1991). "Wave propagation in a multilayered laminated cross-ply composite plate." *ASME J. Appl. Mech.,* **58**, 1028-1032.

[14] Datta, S.K., Achenbach, J.D., and Rajapakse, Y.S., eds. (1990). *Elastic waves and ultrasonic nondestructive evaluation,* Elsevier Science Publishers, Amsterdam, North Holland.

[15] Miklowitz, J., (1960). "Recent developments in elastic wave propagation." *Appl. Mech. Rev.,* **13**(12), 865-878.

[16] Rokhlin, S.I., (1980). "Diffraction of Lamb waves by a finite crack in an elastic layer." *J. Acoust. Soc. Am.,* **67**(4), 1157-1165.

[17] Rokhlin, S.I., (1981). "Resonance phenomena of Lamb wave scattering by a finite crack in a solid layer." *J. Acoust. Soc. Am.,* **69**(4), 922-926.

[18] Tan, M. and Auld, B.A., (1980). "Normal mode variational method for the two- and three- dimensional accoustic scattering in an isotropic plate." *1980 Ultrason Symp. Proc.,* 857-861.

[19] Shah, A.H., Wong, K.C., and Datta, S.K., (1982). "Diffraction of plane SH waves in a half-space." *Earthquake Eng. Struct. Dyn.,* **10**, 519-528.

[20] Wong, K.C., (1985). "Elastic wave scattering by arbitrarily-shaped inhomogeneities." *Ph.D. dissertation.* The University of Manitoba, Winnipeg, Manitoba, Canada.

[21] Abduljabbar, Z., Datta, S.K., and Shah, A.H., (1983). "Diffraction of horizontally polarized shear waves by normal edge cracks in a plate." *J. Appl. Phys.,* **54**(2), 461-472.

[22] Koshiba, M., Karakida, S., and Suzuki, M., (1984). "Finite element analysis of Lamb wave scattering in an elastic plate wave guide." *IEEE Tran. on Sonics and Ultrasonics,* SU-31(1), 18-25.

[23] Paskaramoorthy, R., Shah, A.H., and Datta, S.K., (1989). "Scattering of flexural waves by a crack in a plate." *Eng Fract Mech.,* **33**(4), 589-698.

[24] Bratton, R.L., Datta, S.K., and Shah, A.H., (1990). "propagation and Scattering of Lamb waves in a fibre-reinforced composite plate." *Report 90-1, Center for space construction,* University of Colorado, Bouder, USA.

[25] Ju, T. H. and Datta, S. K., (1992). "Pulse propagation in a laminated composite plate and nondestructive evaluation." *Composites Eng.*, **2** (1), 55- 66.

[26] Datta, S.K., Ju, T.H., and Shah, A.H. (1992). "Scattering of an impact wave by a crack in a composite plate." *ASME J. Appl. Mech.,* **59**, 596-603.

[27] Bond, L.J., (1990). "Numerical techniques and their use to study wave propagation and scattering - a review." *Proceedings of the IUTAM Symposium on Elastic Wave Propagation and Ultrasonic Evaluation*, 17-27.

[28] Pina, H.L.G. and Fernandes, J.L.M., (1981). "some numerical integration formulae over triangles and squares with $1/r$ singularity." *Appl. Math. Modelling,* **5**, 209-211.

[29] Lachat, J.G. and Watson, J.O., (1976). "Effective numerical treatment of boundary integral equations: a formulation for three-dimensional elastostatics." *Int. J. Numer. Methods Eng.* **10**, 991-1005.

[30] Cruse, T.A., (1974). "An improved boundary integral equation method for three dimensional elastic stress analysis." *Compu. Struct.* **4**, 741-754.

[31] Guiggiani, M., (1991). "The evaluation of Cauchy principal value integrals in the boundary element method - a review." *Math. Comput. Modelling*, **15**, 175-184.

[32] Huang, Q. and Cruse, T.A., (1993). "Some notes on singular integral techniques in boundary element analysis." *Int. J. Numer. Methods Eng.*, **36**, 2643-2659.

[33] Cruse, T.A., (1988). *Boundary Element analysis in Computational Fracture Mechanics,* Kluwer Academic Publishers, Boston.

[34] Cruse, T.A., (1972). "Numerical evaluation of elastic stress intensity factors by the boundary-integral equation method." *The Surface Crack: Physical and Computational Solutions*, (Ed. J.L. Swedlow), ASME, N.Y., 153-170.

[35] Snyder, M.D. and Cruse, T.A., (1975). "Boundary-integral equation analysis of cracked anisotropic plate." *Int. J. Fract.,* **11**(2), 315-328.

[36] Cruse, T.A., (1978). "Two-dimensional BIE fracture mechanics." *Appl. Math. Modelling,* **2**, 287-293.

[37] Blanford, G.E., Ingraffea, A.R. and Liggett, J.A., (1981). "Two-dimensional stress intensity factor computations using the boundary element method." *Int. J. Numer. Methods Eng.*, **17**, 387-404.

[38] Gray, L.J., Martha Luiz F., and Ingraffea, A.R., (1990). "Hypersingular integrals in boundary element fracture analysis." *Int. J. Numer. Methods Eng.* **29**, 1135-1158.

[39] Krishnasamy, G. Schmerr, L.W., Rudolphi, T.J., and Rizzo, F.J., (1990). "Hypersingular boundary integral equations: some applications in acoustic and elastic wave scattering." *ASME J. Appl. Mech.*, **57**, 404-414.

[40] Sladek,V., Sladek J., and Tanaka, M., (1993). "Regularization of hypersingular and nearly singular integrals in the potential theory and elasticity." *Int. J. Numer. Methods Eng.,* **36**, 1609-1628.

[41] Beskos, D.E. (1987). "Boundary element methods in dynamic analysis." *Appl. Mech. Rev.,* **40**, 1-23.

[42] Miklowitz, J., (1978). *The Theory of Elastic Waves and Waveguides,* North-Holland, Amsterdam.

[43] Xu, P. C. and Mal, A. K., (1985). "An adaptive integration scheme for irregularly oscillatory functions." *Wave Motion*, **7**, 235-243.

[44] Xu, P.C., and Mal, A.K., (1987). "Calculation of the Green's functions for a layered viscoelastic solid." *Bull. Seism. Soc. Am.,* **77**, 1823-1837.

[45] Mal, A.K. and Lih, S.-S., (1992). "Elastodynamic response of a unidirectional composite laminate to concentrated surface loads: Part I." *ASME J. Appl. Mech.,* **59**, 878-886.

[46] Ceranoglu, A.N., and Pao, Y.H., (1981). "Propagation of elastic pulse and acoustic emission in a plate." *ASME J. Appl. Mech.,* **48**, 125-147.

[47] Weaver,R.L., and Pao,Y.H., (1982). "Axisymmetric elastic waves excited by a point source in a plate." *ASME J. Appl. Mech.,* **49**,821-836.

[48] Vasudevan, N., and Mal, A.K., (1985). "Response of an elastic plate to localized transient sources." *ASME J. Appl. Mech.,* **52**,356-362.

[49] Liu, G.R., Tani, J., Ohyoshi, T., and Watanabe, K., (1991). Transient waves in anisotropic laminated plate, Part I: theory; Part II: application. *ASME J. Vibration and Acoustics.* **113**, 230-239.

[50] Israil,A.S.M. and Banerjee, P.K., (1990). "Two-dimensional transient wave-propagation problems by time-domain BEM." *Int. J. Solids Structures,* **26**(8),851-864.

[51] Dunkin, J.W., (1965). "Computation of modal solution in layered, elastic media at high frequencies." *Bull. Seism. Soc. Am.,* **55**(2), 335-358.

[52] Karunasena, W.M., Shah, A.H., and Datta, S.K., (1991). "Reflection of plane strain waves at the free edge of a laminated composite plate." *Int. J. Solids Structures,* **27**(8), 949-964.

[53] Bathe, K.J., (1982). *Finite Element Procedures in Engineering Analysis*, Prentic-Hall, New Jersey.

[54] Gregory, R.D. and Gladwell, I., (1983). "The reflection of a symmetric Rayleigh-Lamb wave at the fixed or free edge of a plate." *J. Elast.,* **13**, 185-206.

[55] Conte, S.D. and Boor, C.D., (1972). *Elementary Numerical Analysis,* 2nd Edn. McGraw-Hill, New York.

[56] Sneddon, I.N., (1951). *Fourier Transforms*, McGraw-Hill, New York.

[57] Kausel, E and Peek, R., (1982). "Dynamic loads in the interior of a layered stratum: An explicit solution." *Bull. Seism. Soc. Am.,*, **72**, 1459-1481.

[58] Liu, G.R. and Achenbach, J.D., (1995). "Strip element method to analyze wave scattering by cracks in anisotropic laminated plates", *ASME J. Appl. Mech.,* **62**, 607-613.

[59] Mitrinovic, D.S. and Keckic, J.D., (1984). *The Cauchy Method of Residues* , D.Reidel Publishing Company, Boston.

[60] Dong, S.B., Goetchel, D.B. and Muki, R., (1982). "A global-local finite element analysis of axisymmetric scattering of elastic waves", *ASME J. Appl. Mech.,* **49**, 816-820.

[61] Dong, S.B., Avanessian, V. and Muki, R., (1986). "Axisymmetric soil-structure interaction by global-local finite elements", *Int. J. Earthquake Engr. Struct. Dyn.,* **14**, 355-367.

[62] Dong, S.B., Avanessian, V. and Muki, R., (1989). "Interaction of an axisymmetric body with obliquely incident seismic waves by global local finite elements", *Int. J. Earthquake Engr. Struct. Dyn.,* **18**, 185-197.

[63] Zienkiewicz, O.C., (1977). *The Finite Element Method,* McGraw-Hill, London.

[64] Brebbia, C.A., Telles, J.C.F., and Wrobel,L.C., (1984). *Boundary Element Techniques - Theory and Applications in Engineering,* Springer Verlag, Berlin, Heideberg, New York, Tokyo.

[65] Henshell, R.D. and Shaw, K.G., (1975). "Crack-tip finite elements are unnecessary." *Int. J. Num. Meth. Engng.*, **9**, 495-507.

[66] Barsoum, R.S., (1976). "On the use of isoparametric finite elements in linear fracture mechanics." *Int. J. Num. Meth. Engng.*, **10**, 25-37.

[67] Barsoum, R.S., (1977). "Triangular quater-point elements as elastic and perfectly-plastic crack-tip elements." *Int. J. Num. Meth. Engng.*, **11**, 85-98.

[68] Keer, L.M., Lin, W., and Achenbach, J.D., (1984). "Resonance effects for a crack near a free surface," *J. Appl. Mech.,* **51**, 65-70.

[69] Cawley, P., and Theodorakopoulos, C., (1989). "The membrane resonance method of nondestructive testing." *J. Sound and Vibration,* **130**, 299-311.

[70] Pao, Y.H. and Mow, C.C., (1972). *Diffraction of Elastic Waves and Dynamic Stress Concentrations*, Crane, Russak and Company Inc., New York.

[71] Stratton, J.A., (1941). *Electromagnetic Theory*, McGraw-Hill, New York.

[72] Hsu, H.P., (1972). *Fourier Analysis*, Simon and Schuster, New York.

[73] Beissner, R.E., (1986). "Boundary element model of eddy current flaw detection in three dimensions." *J. Appl. Phys.*, **60**(1), 352-356.

[74] Kahn, A.H., (1988). "Boundary integral equation methods for two dimensional models of crack-field interactions." *J. Nondetr. Eval.,* **7**(1/2), 3-14.

[75] Lekhnitskii, S.G., (1963). *Theory of Elasticity in an Anisotropic Body*, Holden-Day, San Francisco.

[76] Karunasena, W.M., (1992). "Elastic waves in laminated composite plates for application in ultrasonic nondestructive evaluation." *Ph.D. dissertation,* The University of Manitoba, Winnipeg, Manitoba, Canada.

Appendix A

Coefficients of matrix $[P^{\Delta}]$

The elements of the matrix $[P_i^{\Delta}]$ appearing in equation (2.24) are given below:

$$
\begin{aligned}
p_{11}^{\Delta} &= p_{66}^{\Delta} = \frac{D_{66}^2}{\Delta_1\Delta_2}k^2\{r_1r_2[(d(1+a)+abc(1+b))cosr_1hcosr_2h - ad(1+b) - bc(1+a)] \\
&\quad +[r_1^2abd(1+a)+r_2^2c(1+b)]sinr_1hsinr_2h\}, \\
p_{12}^{\Delta} &= p_{56}^{\Delta} = \frac{jk}{\Delta_1}(abr_1sinr_1hcosr_2h - r_2cosr_1hsinr_2h), \\
p_{13}^{\Delta} &= p_{46}^{\Delta} = \frac{D_{66}}{\Delta_1\Delta_2}jk[ar_1r_2(d+bc)(cosr_1hcosr_2h-1) \\
&\quad +(a^2r_1^2bd+r_2^2c)sinr_1hsinr_2h], \\
p_{14}^{\Delta} &= p_{36}^{\Delta} = \frac{D_{66}}{\Delta_1\Delta_2}jk^3\{(br_1r_2(ab+2a+1)(cosr_1hcosr_2h-1) \\
&\quad +[r_2^2(1+b)+r_1^2ab^2(1+a)]sinr_1hsinr_2h\}, \\
p_{15}^{\Delta} &= p_{26}^{\Delta} = \frac{jk}{\Delta_2}(r_2sinr_1hcosr_2h - abr_1cosr_1hsinr_2h), \\
p_{16}^{\Delta} &= \frac{k^2}{\Delta_1\Delta_2}[2abr_1r_2(cosr_1hcosr_2h-1)+(a^2b^2r_1^2+r_2^2)sinr_1hsinr_2h], \\
p_{21}^{\Delta} &= p_{65}^{\Delta} = \frac{D_{66}^2}{\Delta_2}jk[r_2c(1+b)sinr_1hcosr_2h - r_1d(1+a)cosr_1hsinr_2h], \\
p_{22}^{\Delta} &= p_{55}^{\Delta} = cosr_1hcosr_2h, \\
p_{23}^{\Delta} &= p_{45}^{\Delta} = \frac{D_{66}}{\Delta_2}(adr_1cosr_1hsinr_2h - cr_2sinr_1hcosr_2h),
\end{aligned}
$$

$$
\begin{aligned}
p^{\Delta}_{24} &= p^{\Delta}_{35} = \frac{D_{66}}{\Delta_2}k^2[r_1(1+b)sinr_1hcosr_2h - r_2b(1+a)cosr_1hsinr_2h],\\
p^{\Delta}_{25} &= \frac{\Delta_1}{\Delta_2}sinr_1hsinr_2h,\\
p^{\Delta}_{31} &= p^{\Delta}_{64} = \frac{D^3_{66}}{\Delta_1\Delta_2}jk^3\{r_1r_2(1+a)(1+b)(d+bc)(cosr_1hcosr_2h-1)\\
&\quad +[r_2^2c(1+b)^2 + r_1^2bd(1+a)^2]sinr_1hsinr_2h\},\\
p^{\Delta}_{32} &= p^{\Delta}_{54} = -\frac{D_{66}}{\Delta_1}k^2[r_1(1+a)bsinr_1hcosr_2h - r_2(1+b)cosr_1hsinr_2h],\\
p^{\Delta}_{33} &= p^{\Delta}_{44} = \frac{D^2_{66}}{\Delta_1\Delta_2}k^2\{r_1r_2[d(1+a)+abc(1+b)+(ad(1+b)-bc(1+a))cosr_1hcosr_2h]\\
&\quad -[r_1^2abd(1+a)+r_2^2c(1+b)]sinr_1hsinr_2h\},\\
p^{\Delta}_{34} &= \frac{D^2_{66}}{\Delta_1\Delta_2}k^4\{2r_1r_2(1+a)(1+b)b(1-cosr_1hcosr_2h)\\
&\quad -[r_2^2(1+b)^2 + r_1^2b^2(1+a)^2]sinr_1hsinr_2h\},\\
p^{\Delta}_{41} &= p^{\Delta}_{63} = \frac{D^3_{66}}{\Delta_1\Delta_2}jk\{(r_1r_2cd(ab+2a+1)(cosr_1hcosr_2h-1)\\
&\quad +[r_1^2ad^2(1+a)+r_2^2c^2(1+b)]sinr_1hsinr_2h\},\\
p^{\Delta}_{42} &= p^{\Delta}_{53} = -\frac{D_{66}}{\Delta_1}(adr_1sinr_1hcosr_2h - cr_2cosr_1hsinr_2h),\\
p^{\Delta}_{43} &= \frac{D^2_{66}}{\Delta_1\Delta_2}[2acdr_1r_2(1-cosr_1hcosr_2h) - (a^2d^2r_1^2+c^2r_2^2)sinr_1hsinr_2h],\\
p^{\Delta}_{51} &= p^{\Delta}_{62} = \frac{D^2_{66}}{\Delta_1}jk[r_1d(1+a)sinr_1hcosr_2h - r_2c(1+b)cosr_1hsinr_2h],\\
p^{\Delta}_{52} &= \frac{\Delta_2}{\Delta_1}sinr_1hsinr_2h,\\
p^{\Delta}_{61} &= \frac{D^4_{66}}{\Delta_1\Delta_2}k^2\{2cdr_1r_2(1+a)(1+b)(cosr_1hcosr_2h-1)\\
&\quad +[r_2^2c^2(1+b)^2 + r_1^2d^2(1+a)^2]sinr_1hsinr_2h\}.
\end{aligned}
\tag{A.1}
$$

$$
\begin{aligned}
c &= (1-\bar{\delta})k^2 - \bar{\beta}r_1^2a; \quad d = (1-\bar{\delta})k^2b - \bar{\beta}r_2^2,\\
\Delta_1 &= D_{66}jk\bar{\beta}r_2^2(\frac{r_1^2}{r_2^2}ab-1); \quad \Delta_2 = D_{66}jkr_1r_2(ab-1),\\
h &= y_{i+1} - y_i = h_i.
\end{aligned}
\tag{A.2}
$$